FOR REFERENCE ONLY

Feasibility of a Laterally Emitting Thin Film Electroluminescence Device as an Application Specific Integrated Display

Dipl.-Ing. Jörg Rüdiger

17 JUL 2001

A thesis submitted in partially fulfilment of the requirements of The Nottingham Trent University for the degree of doctor of philosohpy

June 2001

40 0715254 4

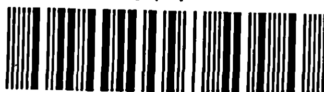

ProQuest Number: 10183396

All rights reserved

INFORMATION TO ALL USERS
The quality of this reproduction is dependent upon the quality of the copy submitted.

In the unlikely event that the author did not send a complete manuscript
and there are missing pages, these will be noted. Also, if material had to be removed,
a note will indicate the deletion.

ProQuest 10183396

Published by ProQuest LLC (2017). Copyright of the Dissertation is held by the Author.

All rights reserved.
This work is protected against unauthorized copying under Title 17, United States Code
Microform Edition © ProQuest LLC.

ProQuest LLC.
789 East Eisenhower Parkway
P.O. Box 1346
Ann Arbor, MI 48106 – 1346

Statement of Original Work

The work presented in this thesis represents the author's contribution to the ongoing research programme at the Nottingham Trent University. The research programme is to understand the physics of laterally emitting thin film electroluminescent (LETFEL) devices and to design an application specific display (ASID) utilizing a standard LETFEL production process. The RC-models, the optical model and the electrical TFEL model with distributed interface charge as presented in this work are developments by the author. The author is responsible for the characterisation of the TFEL devices and the simulation, including writing the simulation programs and designing the measurement systems as presented in this work. The author also designed the set of photo masks used for optical characterisation of the displays and for demonstrating the ASID principal. All of the etching experiments including the photolithographic patterning was carried out by the author.

Abstract

The design of an application specific integrated display (ASID) is demonstrated. The presented ASID is based on the lateral emitting thin film electroluminescence (LETFEL) technology whereby the shape of the display elements is defined by a metal layer. The design is support by theoretical models.

Different Electrical models have been developed for the transient characteristics of TFEL devices and are compared with measured characteristics. The single interface state model, which is based on the assumption that all interface electrons are located on a defined energy level, leads to two equivalent differential equations. The simulated characteristics are in good agreement with measured characteristics, especially for non annealed TFEL devices. The model with distributed interface electrons over the the bandgap leads to a system of differential equations. With this model, the agreement between measured and simulated characteristic could be improved for annealed devices. Furthermore, the case that the interface distribution conserves the equilibrium distribution during the emission process is discussed. Problems in measuring the interface electron distribution are pointed out.

Based on the physical electrical models of TFEL devices, equivalent RC-models with single interface states and distributed interface states are deduced in a theoretical way. The models consists of nonlinear resistors, modeling the tunneling behaviour, and nonlinear capacities, modeling behaviour of the interface electrons. Simulation results are in good agreement with measured results and thus, the RC-models are suitable for embedded simulation of driver electronics and TFEL device.

A novel analytic model of the optical behaviour of LETFEL structures is devel-

oped and employed for calculating the outcoupled light of a pixel used in light emitting dot matrix displays. The presented solutions are based on a ray optics approximation whereby the absorption of the light within the light generating medium (phosphor material) and the transmission behaviour of the phosphor-air interface is taken into account, as well as the micro-mirror width. The model is applied to the circular, square and hexagonal pixels. Furthermore, the influence of MIS-effects on the TFEL characteristic and the electrostatic field distribution in TFELs are studied. Additionally, the feasibility of fabrication of LETFEL devices using magnet enhanced ion etch has been investigated.

Preface

When, more than 60 years ago, the electroluminescence effect was discovered by Destriau, it promised at first glance to be the ideal way of generating light needed for information displays. Electroluminescence - the cold generation of light - occurs when an electrical field is applied across an electroluminescent material. Common electroluminescent materials are mainly wide-bandgap semiconductors, in general *polycrystalline*, doped with rare earth metal, like Zinc-sulfide doped with Manganese. The dopant has the function of light emitting centers and determine the colour of the emitted light. Electroluminescence can be utilized to build readily dot matrix displays by deposition of an electroluminescent thin film - stacked between transparent electrodes - on top of a cheap glass substrate to provide a TFEL-display (thin film electroluminescent display). The colour of the display is chosen by the right kind of dopant. All these aspects deem the electroluminescent display to be the ideal solution for information displays.

Despite the advantages of TFEL-displays and also fifty years of research into them, the cathode ray tube is still the dominant display in use, rendering the TFEL display almost insignificant. The question of what the disadvantages of TFEL-displays are then arises. It emerged that the short life time is the essential problem, which prevents the commercial success. As well as this, the brightness of the displays is low and the driving voltages are, for most display types, high. Yet the underlying disadvantage is that the TFEL principal does not allow an engineering approach. Unlike III-V semiconductor LEDs, where the energy band gap, the crystal lattice constant and carrier concentration of the crystal can be changed continuously and independently, the TFEL display has only a few free parameters which can be tuned. These are for example the light center concentration, the thickness of phosphor and insulator layer. All other parameters, such as carrier

concentration or characteristics of the light center, are principally fixed by the chosen materials.

To minimize these disadvantages, an exact picture of the physical processes involved in the TFEL working principle is essential. This understanding is indispensable for an optimization and for finding out physical limitations of the TFEL display. It gives a better understanding of the failure mechanism and is necessary for a correct measurement of parameter. The causes of problems can be pointed out by an appropriate theory of TFEL, which is a first step towards an improvement of the design.

Acknowledgements

During the course of the work performed for this thesis, many persons have made helpful contributions, and I would like to thank them all.

I am especially grateful to Professor C. B. Thomas for giving me the opportunity to study in England and undertake this research.

I wish to thank Dr. Christos Mias for his spiritual support, helpful discussions and assistance in preparation of writing the papers.

Thanks are equally given to Dr. R. Stevens and Dr. W. M. Cranton, who supervised this thesis, for the effort and patience they spent.

I wish to especially thank my friend and colleague Muru for his help.

I would also like to thank all my colleagues and friends of the research team for the time we spent and worked together. These are Alan, Dr. S. Barros, Dr. M. Craven, Demos, Dr. E. Mastio, Dr. Theng, Dr. R. Ranson, and Dr. C. Tsakonas.

Thanks also go to Rutherford Appleton Laboratory and Qudos Technology Ltd for their technical support.

Finally I will be eternally grateful to my girlfriend Claudia for her continued love, support and encouragement.

Contents

1 Introduction **18**

1.1 Thin Film Electroluminescence 18

1.2 Lateral Emitting Thin Film Electroluminescent Displays 23

1.3 Objective 24

1.4 Structure of the Thesis 26

2 Measurement Methods and Sample Fabrication **27**

2.1 TFEL Fabrication Process for Electrical Characterisation 27

2.2 LETFEL Fabrication Process for Optical Characterisation 29

2.3 Electrical Measurement Method 31

2.4 Optical Measurement Method 32

3 Electrical Characteristics of TFEL Devices **34**

3.1 Fundamental TFEL-Characteristic 35

3.1.1 Relaxed State 35

3.1.2 Compensated State 36

3.1.3 Charge-Voltage and Current-Voltage Characteristic 37
3.1.4 Space Charge Limited Current 39
3.1.5 Tunneling from Interface States 41
3.2 Dynamic TFEL Characteristics for Single Interface State 42
3.2.1 Charge at the Interface 43
3.2.2 Electron Emission from Single Interface State 44
3.2.3 Differential Equation Electrical Field 45
3.2.4 Differential Equation for the Interface Charge 46
3.2.5 Transfer Current 46
3.2.6 Comparison with Measurement 47
3.3 Electrical Characterisation by Simulation 51
3.3.1 Transient Characteristics 51
3.3.2 Current-Frequency-Characteristic 53
3.3.3 Transfered Charge versus Initial Charge 54
3.4 Dynamic TFEL Characteristics for Distributed Interface States . 55
3.4.1 Assessment of Interface State Properties 56
3.4.2 Electron Emission from Distributed Interface States 57
3.4.3 TFEL with Distributed Interface Charge 59
3.4.4 Comparison with Measurement 60
3.5 Measurement of the Interface Electron Distribution 62

4 Electrical Characteristics of LETFEL Devices on Silicon **65**

4.1 Influence of the MIS-Capacity 65

4.2 Electrostatic Field Distribution in LETFELs 72

4.2.1 Simulation Method 72

4.2.2 Simulation Results 74

5 RC-Models for TFEL Devices **76**

5.1 RC-Model for Layered Structure 77

5.2 RC-Model for TFELs with Single Interface State 78

5.2.1 Physical Model of the TFEL 78

5.2.2 Equivalent RC-Network 80

5.2.3 Comparison RC-Model with Measurement 84

5.3 RC-Model for TFELs with Distributed Interface States 85

5.3.1 TFEL with Distributed Interface States 85

5.3.2 RC-Model for TFEL with Distributed Interface States . . 87

5.3.3 Comparison with Measurement 88

5.4 Conclusion 91

6 Optical Characteristics of LETFELs **92**

6.1 Introduction 92

6.2 Attenuation in a Luminescent Waveguide 94

6.3 Optical Characterisation 96

6.3.1 Attenuation in a Passive Waveguide 96

6.3.2 Attenuation in a Active Waveguide 97

6.4 Simple optical model of electroluminescent pixel structures 99

6.4.1 Introduction 99

6.4.2 Model for Three-Dimensional Structures 100

6.4.3 Model for Two-Dimensional Structures 102

6.4.4 Model for Circle, Square and Hexagon Structures 105

6.4.5 Results and Discussion 107

6.5 Conclusion 111

7 Design and Fabrication of an ASID 112

7.1 Design of an ASID 112

7.2 Mask Set Design 115

7.3 Characteristics of Different Pixel Structures 117

7.4 Demonstration of an ASID 118

8 Conclusion and Future Work 120

A Exact Q-V Characteristic 129

B Process and Device Parameter 132

C Compensator Circuit 135

D Photolithographic Masks 137

E Magnet Enhanced Ion Etch **145**

F Listing RC-model **150**

G Publication **152**

List of Symbols

SYMBOL	UNIT	EXPLANATION
A	m^2	TFEL device area, active area
C_d	F	TFEL device capacity
$C_i = A \cdot \epsilon_i/(2d_i)$	F	insulator capacity (both layers)
$C_{ip} = C_iC_p/(C_i + C_p)$	F	capacity of phosphor and insulators layers
$C_p = A \cdot \epsilon_p/d_p$	F	phosphor layer capacity
$C_S(V_S)$	F	nonlinear capacity modeling interface charges
$c_1(E_I) = q_0/(4\sqrt{2m^*E_I})$	$s^{-1} \cdot m/V$	
$c_2(E_I) = 4\sqrt{2m_I^*}E_I^{1.5}/(3q_0\hbar)$	V/m	
E_F	Ws	Fermi energy
E_g	Ws	bandgap energy
E_I	Ws	energy level of the interface state
E_n	Ws	energy level of interface state, $n = 1 \dots m$
d_i	m	insulator layer thickness (one side)
d_p	m	phosphor layer thickness
d_p^*	m	phosphor layer thickness without interface charge region
F_{ip}	V/m	external field at the insulator phosphor interface
f_d	Hz	driving frequency
$f_0(E, E_F) = \frac{1}{1+g\exp(\frac{E-E_F}{kT})}$	1	occupancy function (Fermi-Dirac distribution)
F_S	V/m	electrical field strength at the silicon surface
F_p	V/m	electrical field in the phosphor layer
$F_p(x)$	V/m	electrical field distribution across the phosphor layer
F_0	V/m	electrical field at the cathodic interface
g	1	degeneracy factor
g	$m^{-3} \cdot s^{-1}$	generation rate of carriers
G_S	$m^{-2} \cdot s^{-1}$	surface generation rate
$G(V) = Q_{I0}\mathbf{T}\,[V/d_p]$	A	nonlinear resistor modeling the tunnel behavior
$G_n(V) = Q_{I0.n}\mathbf{T}_n\,[V/d_p]$	A	nonlinear resistor for n.th interface state
$\hbar = h/(2\pi)$	J·s	reduced Planck's constant, h Planck's constant

SYMBOL	UNIT	EXPLANATION
I_D	A	generation and diffusion current from the bulk
I_{SC}	A	generation current in the space charge region
$I_t = dQ_I/dt$	A	transfer current, conduction current in the phosphor layer
$I_d = dQ_d/dt$	A	device current of the TFEL device
$I_{t.n}(t)$	A	transfer or injection current from the n.th energy level
J_h	$\mathrm{A/m^2}$	hole current density
$K = N_d \epsilon_{Si} q_0$	$\mathrm{F \cdot As/m^4}$	
k	J/K	Boltzmann's constant
m^*	kg	effective electron mass of the conduction band
$N_s(E)$	$\mathrm{m^{-2} \cdot (Ws)^{-1}}$	interface state distribution
N_0	$\mathrm{m^{-2} \cdot (Ws)^{-1}}$	average interface state density
$n_I(t)$	$\mathrm{m^{-2}}$	momentary interface electron density at the cathodic interface
n_{I0}	$\mathrm{m^{-2}}$	initial density of mobile electrons at the cathodic interface
$n_I(t, E)$	$\mathrm{m^{-2} \cdot (Ws)^{-1}}$	electron density for the energy interval $[E, E + dE]$.
$n_{I.n}(t)$	$\mathrm{m^{-2}}$	electron density for n.th level, energy range $[E_{n-1}, E_n]$
$n_{I0.n}$	$\mathrm{m^{-2}}$	initial interface electron density for the n.th energy level
N_D	$\mathrm{m^{-3}}$	donor concentration
$n(x)$	$\mathrm{m^{-3}}$	electron concentration across the phosphor layer
n_i	$\mathrm{m^{-3}}$	intrinsic carrier concentration
Q_C	C	charge of nonlinear capacitor C_S
Q_d	C	device charge; charge on the electrodes (anode)
Q_I	C	interface charge at the cathode, polarization charge
q_0	C	elementary charge
$Q_{I0.n} = Aq_0 n_{I0.n}$	C	initial interface charge for the n.th energy level
$Q_{I.n}(0)$	C	interface charge at the beginning for n.th energy level
$Q_{I0} = Aq_0 n_{I0}$	C	initial interface charge
Q_I^*	C	interface charge at the anode, polarization charge
$Q_{I\,\max} = C_i \cdot V_d$	C	maximal transferable interface charge for given device voltage
$Q_t = Q_I(T_d/2) - Q_I(0)$	C	total transfered charge in one halfcycle

SYMBOL	UNIT	EXPLANATION
r	1/s	recombination rate
$sign(x)$		sing function, $sign(x) = 1$ for $x > 0$,
		$sign(x) = -1$ for $x < 0$, $sign(0) = 0$
T	K	temperature
$T_0[F_p(x)]$	1/s	0.th order Taylor Expansion of the electrical field
$\mathbf{T}[F_p, E] = c_1(E)F_p$	1/s	tunneling probability as a function of energy
$\cdot \exp(-\frac{c_2(E)}{F_p})$		
$\mathbf{T}[F_p] = c_1 F_p \exp(-\frac{c_2}{F_p})$	1/s	tunneling probability from energy level E_I
$\mathbf{T}_n[F_p] = \mathbf{T}[F_p, E_n]$	1/s	tunneling probability for the n.th energy level
$T_d = 1/f_d$	s	
t	s	time
V_S	V	voltage drop over the interface charge layer
V_{ip}	V	voltage across the phosphor layer(incl. charge layer)
V_{SC}	V	voltage across the space charge layer
$V_0 = N_d \epsilon_{Si} q_0 / C_{ip}^2$	V/m^4	
$V_T = kT/q_0$	V	thermal voltage
$V_F = -V_T \ln \frac{N_d}{n_i}$	V	flatband voltage
V_d	V	device voltage; voltage across the TFEL device
$\alpha = C_i/(C_i + C_p)$	1	divider factor
α_m	1/m	carrier multiplication rate
ϵ_i	F/m	permittivity of insulator material
ϵ_p	F/m	permittivity of phosphor material
ϵ_{Si}	F/m	permittivity of the silicon
μ	Ws	mean value of the interface state distribution
μ_e	m^2/(V·s)	electron mobility in the phosphor layer
μ_p	m^2/(V·s)	hole mobility μ_p
σ	Ws	standard deviation of the interface state distribution
τ_g	s	generation lifetime
τ_p	s	hole life time

Optical Symbols

SYMBOL	UNIT	EXPLANATION
A	m^2	cross section area of the active waveguide
A_t	m^2	total area of a pixel (active and passive area)
A_{th}	m^2	total area of a hexagonal pixel cell
A_{ts}	m^2	total area of a square pixel cell
$\mathbf{B}(t)$	m	boundary line of the pixel
D	m	pixel diameter of the active area
dS	m^2	illuminated infinitesimal area element on the surface
E	lx	illuminance
$E' = d\Phi/db$	lm/m	two-dimensional illuminance
$g = d\Phi/dV$	$\text{lm}\cdot\text{m}^{-3}$	light generation density of an infinitesimal volume dV
$g' = d\Phi/dA$	$\text{lm}\cdot\text{m}^{-2}$	two-dimensional light generation density
I	cd	luminous intensity
$I' = d\Phi/d\omega$	lm/rad	two-dimensional luminous intensity
$i' = dI'/dA$	$\text{lm}\cdot\text{rad}^{-1}\cdot\text{m}^{-2}$	two-dimensional luminous intensity density
I_a	cd	intensity of an active wave guide
$i_g = dI/dV$	$\text{cd}\cdot\text{m}^{-3}$	intensity density i_g for an infinitesimal volume dV
I_{max}	cd	intensity for an infinite long active waveguide
I_p	cd	intensity of a passive waveguide
I_0	cd	initial intensity
l	m	length of the waveguide
$r = \|\mathbf{r}_1 - \mathbf{r}_2\|$	m	distance between light source and area element
$R_B(\vartheta)$	m	distance from the origin to the boundary line B
S	m^2	illuminated surface area
$T(\vartheta)$	1	transmission function
w	m	micro mirror width
y	m	ordinate
y_g	m	integration index

SYMBOL	UNIT	EXPLANATION
α	m^{-1}	attenuation coefficient
α_1 α_2	rad	integration index
Φ	lm	total light flux (luminous power) of a light source
Φ_c	lm	light flux of a circular pix el
Φ_h	lm	light flux of a hexagonal pixel
Φ_s	lm	light flux of the square pixel
Φ_{s1}	lm	light flux of a square pixel under consideration of the 1st reflection
$\rho = D/\sqrt{3}$	m	distance between center point and corner point of the hexagon
$\vartheta = \angle(\mathbf{r}_1 - \mathbf{r}_2, \mathbf{n}_A)$	rad	angle between the light ray and the surface normal vector $\mathbf{n}_S$
ϑ_t	rad	angle of total internal reflection

Chapter 1

Introduction

1.1 Thin Film Electroluminescence

Electroluminescence is a non-thermal generation of light, which occurs when an electrical field is applied to an electroluminescent material. This electroluminescence effect is utilized in thin film electroluminescent (TFEL) devices. Among other things, TFEL devices can be divided in two types: DC driven TFEL and AC driven TFEL (AC-TFEL) devices. This work will focus on AC-TFEL devices. An AC-TFEL device consists basically of a stack of thin film layers - an electroluminescent thin film (phosphor layer) which is sandwiched between thin film

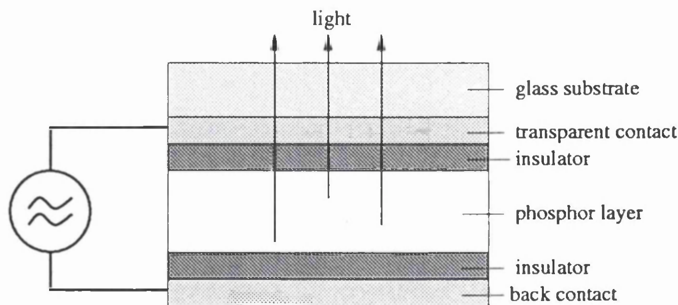

Figure 1.1: Cross section of a TFEL on glass substrate

insulating layers and electrodes, see Figure 1.1. Common phosphor materials are mainly wide-bandgap semiconductors, which are mostly used in a polycrystalline state and doped with a transition metal. Depending on the deposition method, these wide band gap semiconductors are low or non conductive. The dopant has the function of light emitting centers and determine the colour of the emitted light. The contacts are used to apply an AC driving voltage. The insulator layers prevent an injection of electrons from the electrodes into the phosphor layer when a voltage is applied on the electrodes.

The application of an alternating voltage on the electrodes causes an alternating electrical field in the insulator and phosphor layer, which results in emission of light from the phosphor film. The transformation of electrical energy into light occurs in the following way (Figure 1.2):

1. Electrons are injected from interface states between the insulator and phosphor layer into the conduction band of the phosphor layer.

2. These injected electrons are accelerated towards the anode due to the applied field and gain kinetic energy.

3. Electrons, which have gained sufficient high energy (hot electrons), directly excite luminescent centers through impact excitation. Excitation means a transition of inner electrons of the luminescent atom from a low energy state to a higher state. The excited electron subsequently undergoes a spontaneous transition back to the lower energy state under emission of light.

4. Electrons travel through the phosphor layer to the anode and are trapped at the phosphor insulator interface causing a polarization charge.

The same process takes place in the opposite direction when the polarity of the driving voltage is reversed. Each subprocess plays a significant role in the light

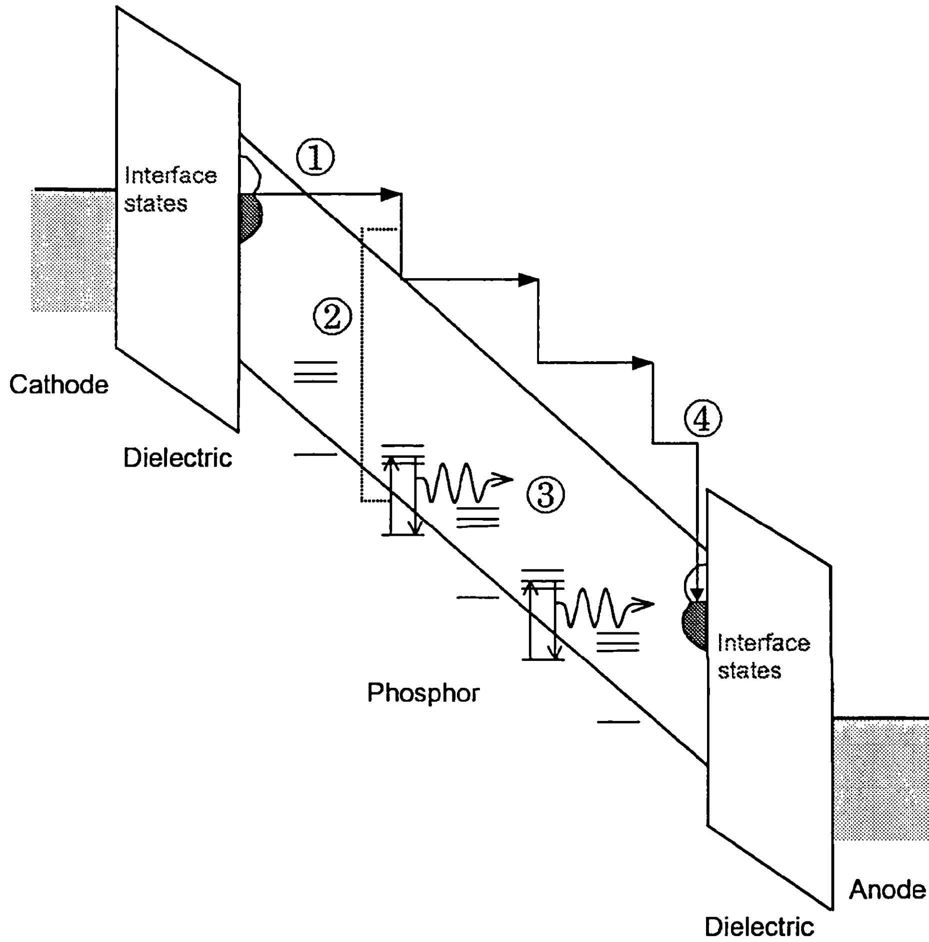

Figure 1.2: 1 Tunnel emission of electrons and acceleration due to applied field, 2 Impact excitation of luminescent centers, 3 Radiative emission, 4 Re-trapping of electrons at anodic interface, after [1]

generation process and needs to be considered for the design of TFELs.

The most important subprocess is the generation of free carriers. Various electron sources are possible as a cause for conduction in the phosphor material. Apart from electron injection from the interface states, other electron generation processes may occur, for instance thermal generation of bulk electrons, emission of electrons from bulk traps and high field carrier multiplication. The thermal generation of electrons plays a minor role, as the used phosphor materials possesses a relative wide bandgap, for example 3.68 eV for ZnS , so that significant carrier concentrations are only reached at high temperatures. Yet for polycrystalline materials, thermal generation could be more relevant, since the distortion of the crystal structure at the grain boundaries creates additional energy states (bulk states) within the forbidden bandgap. Indeed, emission of carriers from bulk states takes place in some phosphor materials, as in CdS, but not in the used ZnS phosphor. High field carrier multiplication may also play a role. Experimental estimation of the impact ionization rate gave values between $1 \ldots 3 \cdot 10^4/cm$ [2]. It is believed that carrier multiplication is involved especially in TFEL devices with hysteretic characteristic.

However, it has been shown by various works that emission of electrons from interface states plays a major role in the light generation process in ZnS–phosphor TFEL devices [3]. Interface states within the forbidden bandgap are created at the interface between the insulator and phosphor layer because the crystal structure of the insulator and phosphor material is distorted, which results in unsaturated (dangling) bonds of the atoms. Those unsaturated bondings can easily capture and release electrons. They therefore represent allowed energy states in addition to the states of the conduction and valence band. The unsaturated bondings or free energy states are designated as interface states and the captured electrons are

interface electrons. The interface states are continously distributed throughout the bandgap. Little is known about the the interface state distribution so far. However, attempts has been made to measure the interface electron distribution with different methods [4], [5].

When an electrical field is applied, interface electrons are emitted from the interface states into the conduction band of the phosphor layer. This emission results from pure field stimulated tunneling of electrons through the forbidden bandgap into the conduction band of the phosphor layer. Due to the field in the phosphor layer, these emitted electrons are accelerated towards the positive electrode thus gaining energy. During this acceleration process the electrons undergo different scattering processes, for example scattering with phonons or collisions with light emitting centers. If the energy of the electrons is higher than the energy of the bandgap, a collision with a lattice atom can also result in a carrier multiplication process (generation of an electron hole pair). If hot electrons collide with light emitting centers and have sufficient kinetic energy ($E > 2.2V$ for Mn, [1]), they can cause an impact excitation of the light emitting center, which eventually results in the emission of light. The excitation results in a transition of an inner shell electron from a low energy state to a higher energy state. Different shell transitions are possible [1],[6]. The cross section for a transition by electron impact is estimated as $\sigma_{Mn^{2+}} = 3.7 \cdot 10^{-16}\text{cm}^2$ in [7] and in [8].

When an excited electron returns to the ground state, the energy difference is emitted as visible light (about $\lambda = 600$ nm for Mn centers). This process is a spontaneous emission of light. The average time until the electron returns is called the decay time. The decay time of the luminescent Mn-centers depend on the center concentration [3], the luminescence level [9], the field strength [10] and on the deposition and annealing process [3]. Electrons, which are involved in

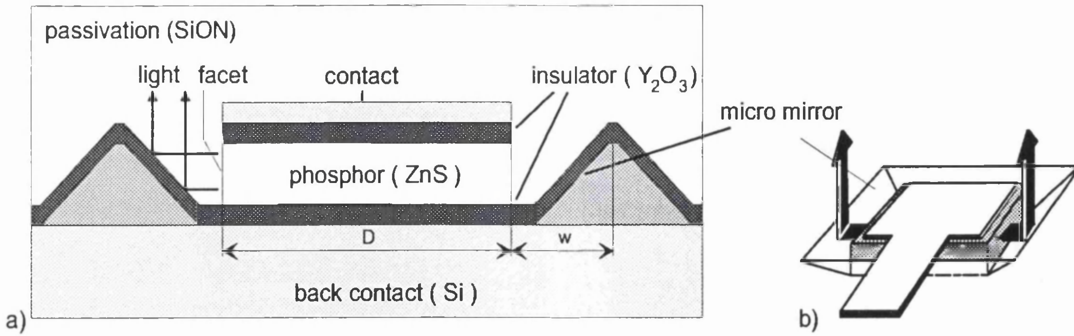

Figure 1.3: a) Cross section of a LETFEL device, b) Schematic of a LETFEL pixel

any collision, lose kinetic energy and again take part in the acceleration process. When the electrons eventually reach the positive electrode, they are trapped by a free interface state.

1.2 Lateral Emitting Thin Film Electroluminescent Displays

The Lateral Emitting Thin Film Electroluminescence (LETFEL) device, as used in this research program, is an improvement of the conventional thin film electroluminescence (TFEL) device [11], [12], [13], [14]. In conventional TFEL devices, generated light is coupled out in a direction perpendicular to the film plane by passing through the insulator layer and the transparent electrode. As a result, the light is attenuated because the transparent electrode possesses a low transparency in comparison to glass-like materials (SiO_2). Moreover, light that is emitted sidewards in the film-plane is not coupled out and is therefore lost. The LETFEL device, as illustrated in Figure 1.3a, attempts to overcome these disadvantages by utilizing lateral emission of light (sidewards to the film plane).

The LETFEL basically consists of a conventional TFEL stack (Y_2O_3-insulator,

ZnS-phosphor, Y_2O_3-insulator) for generating light. In addition, this TFEL stack forms a planar waveguide [15][16], so that light, generated within the phosphor layer (ZnS), is guided along the planar waveguide to the phosphor-passivation interface (facet). There, it is coupled out laterally and deflected by micro-mirrors in a direction perpendicular to the film plane. By avoiding light emission through the top electrode, the brightness of the LETFEL device is approximately four times higher than an equivalent TFEL device [17]. The mirrors are arranged to provide surface emitting apertures forming display elements, i.e. digits, letters or simple pixels. Figure 1.3b shows such a pixel formed with mirrors surrounding the active TFEL stack.

A further specific detail of the LETFEL display is the use of a commercial, mono crystalline silicon wafer as substrate and back contact. The advantage of using a Si-substrate is that it potentially enables the integration of driver electronics for the display [18]. This is especially interesting for miniaturized displays, for example head mounted displays. By integrating the driver electronics in the display substrate, the number of expensive connection pins can be reduced.

1.3 Objective

The use of LETFEL devices for many display applications has been presented in different works [17]. The most important display application is, of course, the full accessible dot matrix display. However, displays with a fixed legend are a common and adequate solution for many information display applications. The shape of the display elements are, in this case, defined by the customer's application.

At the present time, a complete new set of approximately five photo-lithographic masks are necessary for the fabrication of the most basic custom defined display.

For reducing production costs and indeed making a fixed legend device commercially attractive, it is desirable to adapt a standard display device to different custom defined displays by changing one photo mask only. This goal can be achieved by a standard device with an array of small pixel cells, which can be connected to more complex display elements solely by changing the metal layer.

The overall aim of the research presented in this thesis is to design a LETFEL device usable as a fixed legend Application Specific Integrated Display (ASID). The design has been supported by theoretical investigations and experimental device characterizations. Individual objectives presented are as follows:

- Study of the electrical characteristics involving the design decision, i.e. electrostatic field distribution and MIS-influence
- Development of electrical equivalent RC-models of a TFEL usable for embedded simulation of driver electronics and TFEL
- Theoretical investigation of the optical efficency of different cell structures by using a new developed calculation method
- Design of an ASID
- Fabrication and testing of an ASID device to demonstrate the principle
- Characterisation of the resultant displays
- Feasibility study using magnet enhanced ion etcher for producing LETFEL Devices

1.4 Structure of the Thesis

Chapter 2 details the sample preparation and the measurement procedure for electrical and optical characterisation of TFEL and LETFEL devices. A theoretical investigation of the electrical characteristics of AC TFEL devices is presented in Chapter 3. Problems in measuring the interface electron distribution are also discussed in this chapter. Electrical characteristics of LETFEL devices as used in this work are examined in chapter 4. Chapter 5 shows equivalent RC-models for TFEL devices derived from the physical equation. Chapter 6 presents a new, simple optical model for optimizing a pixel structure. Chapter 7 details the design and fabrication of a LETFEL ASID. Chapter 8 gives a conclusion and an outlook for future work.

Chapter 2

Measurement Methods and Sample Fabrication

2.1 TFEL Fabrication Process for Electrical Characterisation

This section details the process steps for producing TFEL devices as used for the electrical characterisation. The major process steps are illustrated in Figure 2.1. All process steps and process parameter for the TFEL sample wafer jr2 are shown in Table B.1 of the appendix. The detailed processing sequence for TFEL devices and investigation are reported in [3], [16] and [17].

The substrate used for the devices is a standard 4 inch Silicon wafer, which is n-doped and has a resistivity of $4 \ldots 10\,\Omega\cdot$cm. The first step is the deposition of a TiW metal base layer on top of the Si-substrate by DC sputtering. Subsequently, the TFEL stack, consisting of insulator (Y_2O_3) and phosphor (ZnS:Mn) layers, is deposited by RF sputtering in Argon atmosphere. The deposition of the TFEL

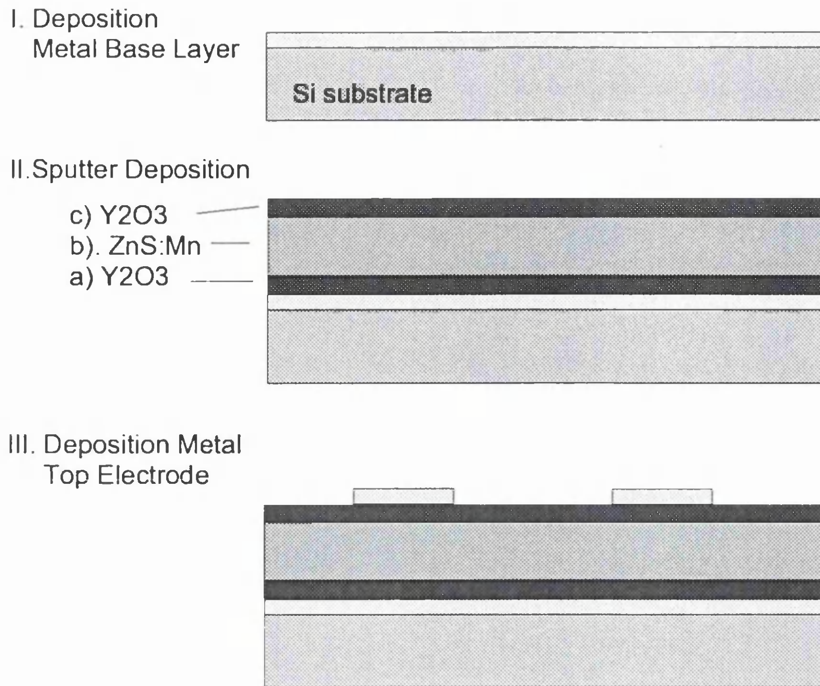

Figure 2.1: Main process steps for production of TFEL devices

stack is done in a separate sputter system in order to avoid contamination with metal. After deposition of the TFEL stack, the device is optional thermally annealed to activate the luminescent centres. A quarter of wafer jr2 has not been annealed (sample jr2b), another quarter of sample wafer jr2 has been thermally annealed (sample jr2a). For details of the deposition and annealing process see [3] and [16].

The deposition of the top electrode is subsequently done by thermal evaporation through a contact mask with circular openings. The material used for the top electrode is Aluminium. Finally, Aluminium is deposited in the same way on the back of the Silicon wafer to improve the back contact conductivity.

2.2 LETFEL Fabrication Process for Optical Characterisation

The process steps for producing a most basic LETFEL device, as used for the optical characterisation and demonstration of an ASID with sample wafer jr1, are illustrated Figure 2.2 of the appendix. All process steps and process parameter are shown in Table B.3. A detailed investigation and the complete process sequence for LETFEL devices are reported in [3], [16] and [17]. The etching of device facets with Ion Milling has been investigated and detailed in [15].

The substrate used for the devices is a standard 4 inch Silicon wafer, which is n-doped and has a resistivity of $4 \ldots 10\,\Omega\cdot$cm. The micro mirrors are made of SiO_2 and are produced outside the university by QUDOS Ltd. (Figure 2.2.I). The production of the micro mirrors is basically done by deposition of SiO_2 (2.2.Ia), photolithography (2.2.Ib), reactive etch of the SiO_2 (2.2.Ic) and strip resist. The TFEL stack, consisting of insulator (Y_2O_3) and phosphor (ZnS:Mn) layers, is subsequently deposited by RF sputtering (2.2.Ia-c) in Argon atmosphere. Subsequently, the TFEL stack is thermally annealed to activate the luminescent centres. For details of the deposition and annealing process see [3] and [16].

The Aluminum top electrode is deposited on top of the TFEL stack by thermal evaporation (2.2.IIIa). A photolithographic process is used to define a photo resist mask in the shape of the electrodes (2.2.IIIb). After that, the Al metal layer is then etched with Argon ion etch (2.2.IIIc). The remaining photo resist is removed with a plasma asher. For improving the back contact conductivity, Aluminium is finally deposited on the back of the Silicon wafer.

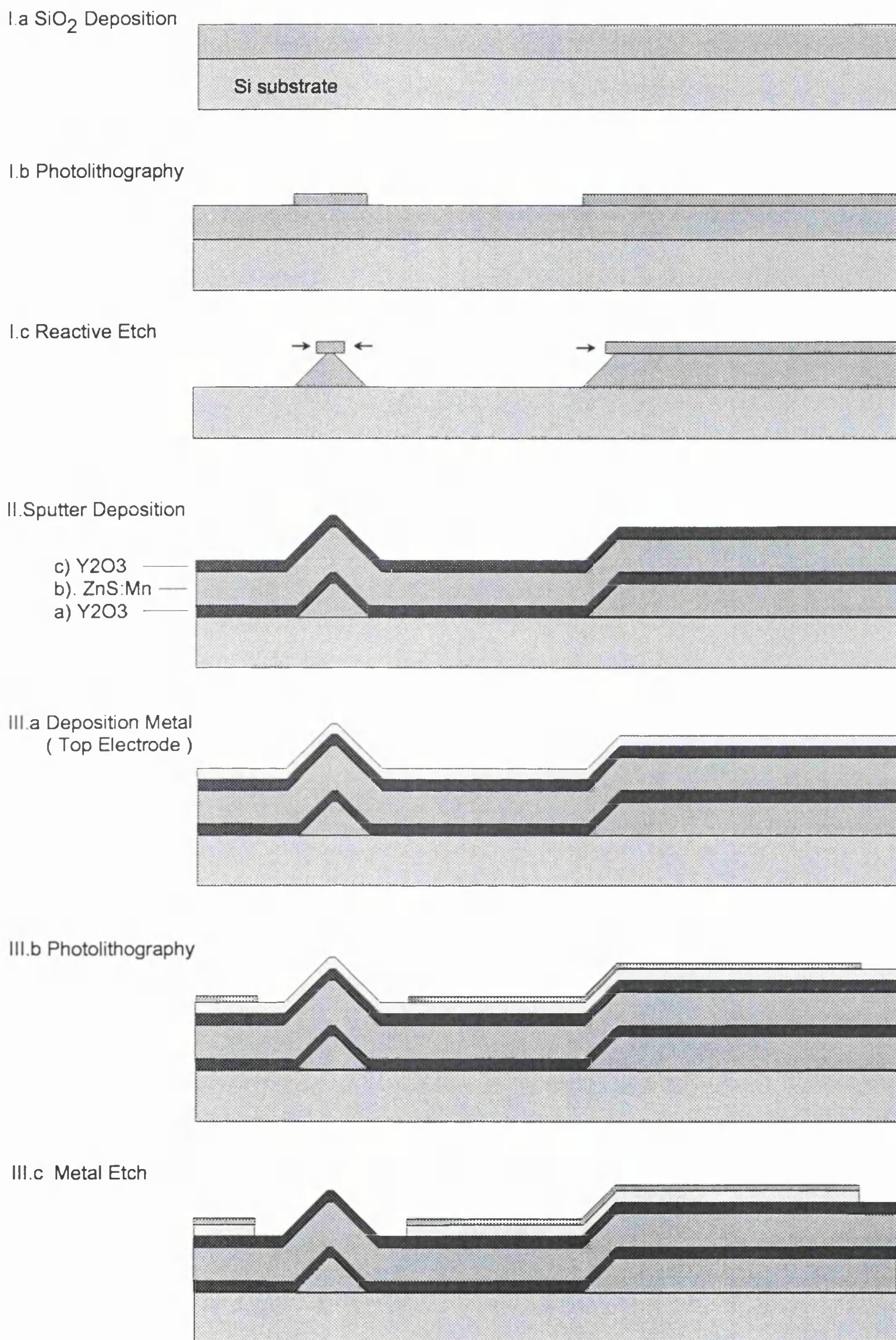

Figure 2.2: Main process steps for production of LETFEL devices

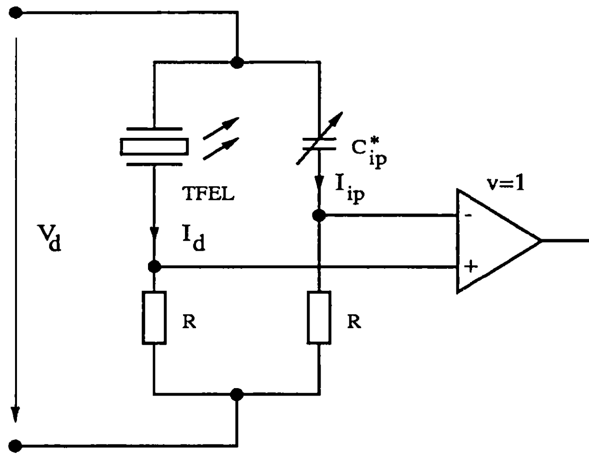

Figure 2.3: Compensator Circuit

2.3 Electrical Measurement Method

The electrical characterisation is carried out by direct measurement of the transfer current (conduction current) in the phosphor layer. The transfered charge is subsequently obtained from this data by numerical integration of the transfer current over the time. All electrical measurement shown in this work are done with the TFEL sample wafer jr2 (see section 2.1 for details of the production process). Since the TFEL stack is grown on a metal base layer, the influence of the underlaying silicon is eliminated.

The measurement of the transfer current has been done with a compensator circuit for compensating the displacement current of the TFEL capacity C_{ip}, as reported in many publications, for instance see [10], [48]. The principal schematic of the compensator is shown in Figure 2.3. The complete electrical circuit is shown in the appendix in Figure C.1. The measurement of the transfer current is done by subtracting a current I_{ip}, which is equal to the displacement current of the TFEL capacity, from the total device current I_d. The device current is given by equation

(A.16)

$$I_d = C_{ip}\frac{dV_d}{dt} + \frac{C_{ip}}{C_p}I_t \quad . \tag{2.1}$$

The current I_{ip} is equal to the displacement current if the adjustable capacitor C_{ip}^* is made equal to the TFEL capacity C_{ip}. The capacities are matched by tuning the adjustable capacitor C_{ip}^* while the device voltage is below threshold ($I_t \approx 0$) so that the measured current becomes zero. In that case, $I_{ip} = C_{ip}\frac{dV_d}{dt}$ because of $C_{ip} = C_{ip}^*$. If this current is subtracted from the device current, one gets:

$$I_d - I_{ip} = \frac{C_{ip}}{C_p}I_t \tag{2.2}$$

$$I_t = \frac{1}{\alpha}(I_d - I_{ip}) \tag{2.3}$$

where α is defined by (3.5). The subtraction is done with an difference amplifier and the measured voltage must be subsequently divided by α in order to obtain the actual transfer current.

The measurement of the transfer current has been carried out in a steady state regime and with a digital oscilloscope, which takes an average over about 50 cycles. In addition, the number of measured points has been reduced by averaging of 10 consecutive measured points.

2.4 Optical Measurement Method

The initial measurement of the optical characteristics of LETFEL displays was done by measuring the luminance with a Minolta luminance meter in a perpendicular direction to the substrate. This method leads to problems because the intensity of the emitted light is measured only from one direction and therefore,

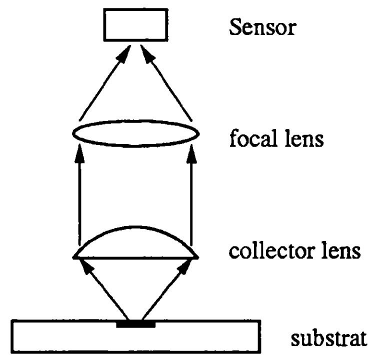

Figure 2.4: Schematic of the optical system used for integral measurement of the emitted light flux

in order to compare different displays, the angular distribution of the intensity must be identical between the displays. This condition is difficult to realise since the low production precision of the micro mirrors cause differences in the angular distribution. In order to reduce the influence on the measurement due to the variation of the angular distribution, the optical characterisation of the display should ideally be made by measuring the total light flux. However, it is more practicable to make an integrating measurement of the light flux for a certain solid angle. This way of measuring has been done with an optical system as shown in Figure 2.4. The collector lense collects all emitted light within an angle of about 45° around the perpendicular line of the display. An integral measurement of the emitted light has been done in this way for all optical measurements reported in this work. The reported measurements are an average of four equal displays on the same wafer. They all have been done with the LETFEL same sample wafer jr1 (see section 2.2 for details of the production process).

Chapter 3

Electrical Characteristics of TFEL Devices

Several electrical models for TFEL devices have been developed up to now, for instance see [19], [20], [21]. These models describe either non-hysteretic behavior or hysteretic behavior of TFELs, for instance [22], [23],[24]. Also analytical models have been presented in [25]. These models are developed for the case of a single interface state distribution.

The aim of this chapter is to develop an electrical model in a straightforward way for single and distributed interface states. In comparison to other models, the analysis leads to two equivalent nonlinear differential equation for the single interface state TFEL model and to a system of nonlinear first order differential equations for distributed interface states. These differential equations are solved with a standard numerical solver. The simulation results are compared with measured data in order to validate the models. The question is examined of whether a model with single interface states is adequate to describe TFEL devices.

3.1 Fundamental TFEL-Characteristic

The TFEL structure represents a layered capacitor where the two insulator layers can be considered as one dielectric layer if they are symmetrical. When a voltage V_d is applied to the electrodes the electrical field in the phosphor layer causes a charge (electrons) transfer through the phosphor layer from the Y_2O_3–ZnS–interface on the one side to the interface on the opposite side. As a consequence, the external charge Q_d on the electrodes is a function of the external voltage V_d and the transferred interface charge Q_I:

$$Q_d = f(V_d, Q_I) \tag{3.1}$$

3.1.1 Relaxed State

The relaxed state is the state where no transferred charge is present ($Q_I = 0$). The relaxed state can be achieved when no voltage is applied on the electrodes for a sufficiently long time (up to days), so that all transferred charge flows back until a field free equilibrium is reached (also called flat band case). If no charge is transferred, the total TFEL device capacity C_d below threshold voltage is equal to the capacity of a layered capacitor C_{ip}:

$$Q_I = 0: \qquad C_{ip} = \frac{C_i C_p}{C_i + C_p} \tag{3.2}$$

The insulator capacitance C_i (total capacity of both insulator layers) and the phosphor layer capacitance C_p are given by

$$C_i = A \cdot \epsilon_i / (2d_i) \quad and \quad C_p = A \cdot \epsilon_p / d_p \tag{3.3}$$

where d_p is the phosphor layer thickness, the insulator layer thickness (one side) d_i, the active area A, the permittivity ϵ_p and ϵ_i for the phosphor and insulator material. The field F_p in the phosphor layer is given for an applied device voltage V_d by

$$F_p = \frac{C_i}{C_i + C_p} \cdot \frac{V_d}{d_p} = \frac{\alpha}{d_p} V_d \tag{3.4}$$

where α is

$$\alpha = \frac{C_i}{C_i + C_p} \quad . \tag{3.5}$$

This factor describes the ratio of the voltage drop across the phosphor layer to the applied device voltage.

3.1.2 Compensated State

A transfer of charge occurs when a voltage above threshold voltage is applied to the TFEL device. The charge transfer continues as long as the field in the phosphor layer is not equal to zero. The transferred charge causes an electrical field in the opposite direction to the external field. This transferred charge therefore compensates the external applied field in the phosphor layer and cause the transfer process to decay. If enough interface electrons are available the field in the phosphor layer goes to zero after a sufficiently long time. In reality, the transfer process virtually comes to an standstill when the field in the phosphor layer goes below threshold field strength.

The following equation characterize the compensated state:

$$F_p \approx 0 \tag{3.6}$$

$$Q_I = C_i \cdot V_d = Q_{I\,\max} \tag{3.7}$$

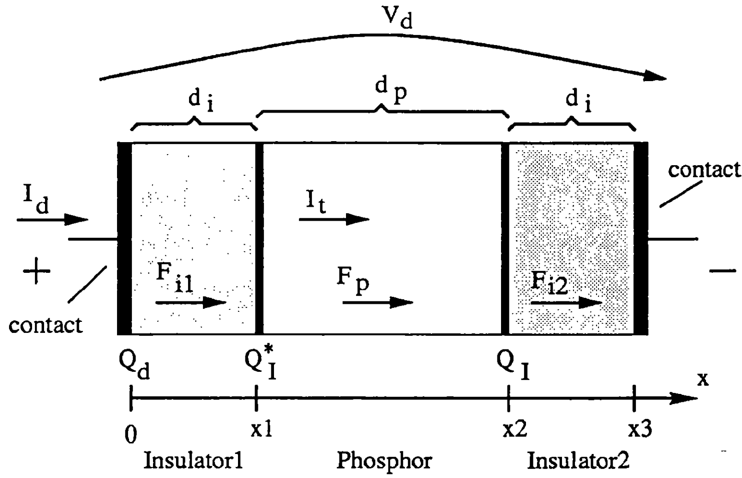

Figure 3.1: 1-Dimensional Structure of a TFEL Device

where $Q_{I\,\max}$ is the maximal amount of charge which can be transferred in the TFEL for a given device voltage V_d. The maximal transferable charge $Q_{I\,\max}$ thus depends on the insulator capacity C_i for a given device voltage V_d. In this case, the total TFEL device capacity C_d is equal to the insulator capacity.

3.1.3 Charge-Voltage and Current-Voltage Characteristic

In order to find the charge voltage characteristics of the TFEL, the charge distribution of the TFEL must be known. The field distribution is then found by integrating the Poisson's equation for the given charge distribution of the TFEL. By integrating the result a second time, the charge voltage characteristic is obtained. Let Q_d be the charge on the anodic electrode, Q_I and Q_I^* be the transferred charge concentrated in a thin layer at the cathodic and anodic insulator-phosphor interface (denoted as interface charge), as illustrated in Figure 3.1. Furthermore, we assume that the distributed charge in the phosphor is negligible (see 3.1.4). Because of that and the charge conservation, it is $Q_I = -Q_I^*$. By solving Poisson's equation for this charge distribution as shown in appendix A, it follows the device

voltage V_d as a function of the device charge

$$V_d = \frac{Q_d}{C_{ip}} - \frac{Q_I}{C_p} \tag{3.8}$$

The external device voltage is thus the difference of the voltage across the TFEL-Capacitor C_{ip} caused by the charges on the electrodes and the voltage across the phosphor layer caused by the transferred interface charge. The field in the phosphor layer and the transferred charge as function of the device voltage are then

$$F_p = \frac{1}{d_p}\left(V_d - \frac{Q_d}{C_i}\right) \tag{3.9}$$

$$F_p = \frac{1}{d_p}\left(\alpha V_d - \frac{Q_I}{C_p + C_i}\right) \tag{3.10}$$

$$Q_I = Q_d/\alpha - C_p V_d \tag{3.11}$$

Above equation are valid at every time t. If the device voltage and the device charge are measured, the field in the phosphor layer and the interface charge can be calculated using equations (3.9) and (3.11). The transfer current in the phosphor layer is $I_t = dQ_I/dt$ and the total device current is $I_d = dQ_d/dt$. When equation (3.8) is differentiated with respect to t, it follows

$$I_d/C_{ip} - I_t/C_p = \frac{dV_d}{dt} \tag{3.12}$$

The first term on the left hand side is the voltage drop due to the displacement current and the second term represents voltage drop caused by transfer current.

3.1.4 Space Charge Limited Current

The electrons, which are injected into the phosphor layer and traveling through it, create a space charge in the phosphor layer. This distributed charge influences the electrical field in the phosphor layer and therefore alter the electron injection process [26]. The injected current is so called space charge limited. Therefore, it is of importance to estimate the influence of the space charge.

The field distribution $F_p(x)$ and the electron concentration $n(x)$ across the phosphor layer can be calculated for a given current density by solving the Poisson's equation under the assumption that no carrier multiplication, generation g or recombination r occurs:

$$r = g = 0; \; \alpha_m = 0; \; J_h = 0 \tag{3.13}$$

As a result of the assumption, the hole current density J_h equals zero. Starting with the Possion's equation (3.14) and the equation for the current density

$$\frac{dF_p(x)}{dx} = -q_0 n(x)/\epsilon_p \tag{3.14}$$

$$J_e = q_0 \mu_e n(x) F_p(x) \tag{3.15}$$

one can eliminate $n(x)$ between (3.14) and (3.15), and one gets the differential equation

$$J_e = -\mu_e \epsilon_p F_p(x) \frac{dF_p(x)}{dx} \quad . \tag{3.16}$$

The electrical field at the cathodic interface $F_0 = F_p(x = 0)$ must be given as a boundary condition. Integration of this equation with the boundary condition leads to

$$F_p(x) = \sqrt{F_0^2 - \frac{2}{\mu_e \epsilon_p} J_e x} \quad for\ 0 \leq x \leq d_p \quad . \tag{3.17}$$

This function describes the field distribution across the phosphor layer for a given injection current and field F_0 . In fact, J_e is also a function of the field F_0 and is given by the tunneling of interface electrons, see equation (3.26). The following analysis of function (3.17) for a real TFEL device under normal driving condition shows that the electrical field across the phosphor layer can be considered as constant. That means in other words that the space charge is negligible. The function of the electrical field $F_p(x)$ can thus expanded in the 0.th order Taylor Series at $x = 0$:

$$F_c(x) = T_0[F_p(x)] = F_p(0) = F_0 \tag{3.18}$$

The maximum deviation from the actual value $\Delta F = |F_p(x) - F_c(x)|$ is estimated with the truncation error

$$\Delta F(x) \leq \max\{F_p'(\xi) \cdot x \mid 0 \leq \xi \leq x\} \tag{3.19}$$

$$\leq \frac{d_p J_e}{\mu_e \epsilon_p \sqrt{F_0^2 - \frac{2}{\mu_e \epsilon_p} J_e d_p}} \tag{3.20}$$

For example consider a ZnS phosphor layer with $d_p = 1\mu$m, $\epsilon_p = 7.5 \cdot \epsilon_0$, $\mu_e =$ 165 cm^2/Vs, applied Voltage $V_d = 10 \ldots 270$ V $\equiv F_p = 3.6 \cdot 10^4 \ldots 10^6$ V/cm, high injected current density of $J_e = 1$ A/cm^2. The error caused by the Taylor Expansion is with $\Delta F(x) \leq 3 \cdot 10^{-8}$ negligible . Therefore, the assumption of a constant field across the phosphor layer is valid.

3.1.5 Tunneling from Interface States

The application of an electrical field across the phosphor layer causes an injection of electrons from electron occupied interface states into the conduction band of the phosphor layer. It has been found that the injection process in ZnS TFELs is dominated by pure tunneling through the bandgap barrier [3]. For the case of a TFEL, the electron emission rate is calculated for a triangular potential barrier. That can be done by solving the tunneling probability with the Wentzel-Kramers-Brillouin approximation (WKB-approximation [27]). The electron emission rate is for a field F_p in the phosphor layer [28]:

$$\mathrm{T}\,[F_p] = c_1 F_p \exp(-\frac{c_2}{F_p}) \tag{3.21}$$

with the constants

$$c_1(E_I) = \frac{q_0}{4\sqrt{2m^* E_I}} \quad and \quad c_2(E_I) = \frac{4\sqrt{2m^*} E_I^{3/2}}{3 q_0 \hbar} \tag{3.22}$$

where m^* is the effective electron mass of ZnS in the conduction band ($m^* \approx 0.25 m_0$), q_0 is the elementary charge, $\hbar = h/(2\pi)$ and h is Planck's constant. The energy E_I denotes the energy level of the interface state counted from the lowest band edge of the conduction band. The field F_p is the electrical field strength at cathodic insulator-phosphor-interface. Figure 3.2 shows the electron emission rate (tunneling probability) over the electrical field for different energy levels of the interface state. The sudden increase of electron emission above a threshold field strength is the reason for the threshold voltage in the brightness–voltage–characteristic of the TFEL device [29].

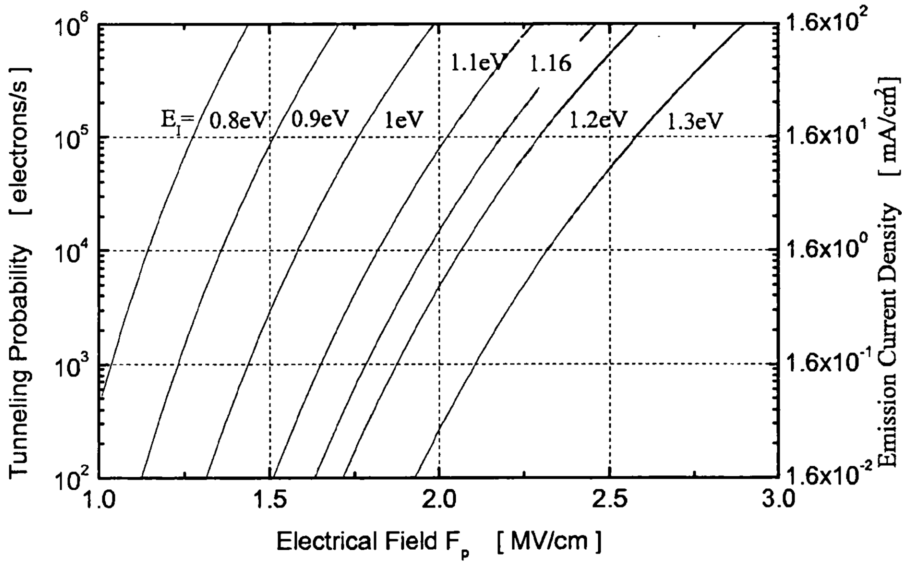

Figure 3.2: Calculated tunneling probability (electron emission rate) versus field for different energy levels below the conduction band (equation 3.21); right scale: emission current density for a interface electron density $n_0 = 10^{12}$ electrons per cm^2 (see equation 3.26)

3.2 Dynamic TFEL Characteristics for Single Interface State

The dynamic characteristics developed in this section are for TFELs with a single interface state distribution. Single interface distribution means that all interface electrons are located at the same definite energy level E_I below the conduction band (Dirac distribution). This is a rather idealistic model as the interface electrons are distributed over the whole bandgap. In addition, it is assumed that no carrier multiplication occurs. Despite the assumption, a simulation of this simple case can give important insight into the working principal of the TFEL, as well as being a good approximation of the physical processes.

3.2.1 Charge at the Interface

If electrons are transferred from the cathode to the anode, unsaturated bonds remain on the cathode, causing a positive interface charge Q_I. Respectively, trapped electrons on the anode cause a negative charge Q_I^*. Let n_{I0} be the initial density of available interface electrons at the cathodic interface in the relaxed state, that is, when no electrons are transferred from one to the other side. Under this condition, no internal electric field exists since all interface electrons are bonded and thus they are electrically compensated. The number of interface electrons $n_I \cdot A$ does not necessarily need to correspondent to the number of transferred electrons. In general, the number of transfered electrons is less then number of the available interface electrons.

If the interface electron density differs from the initial density n_{I0}, the interface charge at the cathodic interface is then

$$Q_I(t) = -q_0 A(n_I(t) - n_{I0}) \tag{3.23}$$

where $n_I(t)$ is momentary interface electron density at the cathodic interface at the time t. A surplus of electrons at the cathode results in a negative interface charge Q_I. For convenience, an initial interface charge Q_{I0}, characterizing the amount of mobile electrons for one side in the relaxed state, can be defined as

$$Q_{I0} = Aq_0 n_{I0} \quad . \tag{3.24}$$

Note, that Q_{I0} does not represent a charge in the conventional sense, since the charge Q_{I0} is an equivalent expression for the initial interface electron density n_{I0} and does not cause any electrical field. Rewriting equation (3.23) with (3.24), one

gets an expression for the interface electron density at the time t :

$$n_I(t) = \frac{1}{Aq_0}\{Q_{I0} - Q_I(t)\} \tag{3.25}$$

3.2.2 Electron Emission from Single Interface State

The number of injected electrons per second is the product of the amount of available interface electrons and the tunneling probability. If $n_I(t)$ denotes the amount of available interface electrons per area, the transfer current (or injection current) is then

$$I_t(t) = q_0 A n_I(t) \mathbf{T}\left[F_p(t)\right] \tag{3.26}$$

where $F_p(t)$ is the electrical field in the phosphor layer at time t, $n_I(t)$ is the interface electron density, A is the device area, $\mathbf{T}$ is the tunneling function (3.21) for the given energy level E_I of the interface state [20]. Since electrons are emitted from the interface state under the applied electrical field, the amount of available interface electrons decreases with time. The transfer current is obtained by differentiating equation (3.23) with respect to t :

$$I_t(t) = \frac{dQ_I}{dt} = -q_0 A \frac{d}{dt} n_I(t) \tag{3.27}$$

A decrease of the interface electron density $n_I(t)$ at the cathode means that electrons are emitted and consequently cause a positive transfer current, see Figure 3.1.

3.2.3 Differential Equation Electrical Field

The electrical field in the phosphor layer F_p as function of time can be expressed as a differential equation where the applied device voltage $V_d(t)$ is the stimulus function and either the interface charge or the initial electrical field in the phosphor layer need to be known as the initial value. By equating (3.26) and (3.27), I_t is eliminated, and subsequently substitution of n_I with equation (3.25) gives

$$\frac{d}{dt}Q_I(t) = (Q_{I0} - Q_I(t))\,\mathbf{T}\left[F_p(t)\right] \quad . \tag{3.28}$$

Rewriting equation (3.10), the interface charge as a function of the applied device voltage V_d and the internal field F_p in the phosphor layer is

$$Q_I(t) = (C_p + C_i)\left(\alpha V_d(t) - d_p F_p(t)\right) \quad . \tag{3.29}$$

Substitution of Q_I in equation (3.28) with the above equation gives finally the differential equation for the field:

$$\frac{d}{dt}F_p(t) + \left(F_p(t) - \frac{\alpha}{d_p}V_d(t) + \frac{1}{d_p}\frac{Q_{I0}}{C_p + C_i}\right)\mathbf{T}\left[F_p(t)\right] = \frac{\alpha}{d_p}\frac{d}{dt}V_d(t) \quad , \tag{3.30}$$

which is similar to the equation obtained in [20]. This equation is a first order nonlinear differential equation. For a better understanding, this equation can be rewritten with equation (3.29) as

$$\frac{d}{dt}F_p(t) + \left(\frac{1}{d_p}\frac{Q_{I0} - Q_I(t)}{C_p + C_i}\right)\mathbf{T}\left[F_p(t)\right] = \frac{\alpha}{d_p}\frac{d}{dt}V_d(t) \tag{3.31}$$

Two extreme cases are of interest: first case, under the condition $Q_{I0} = Q_I(t)$, that is when all available interface charges are transferred to the opposite side (

exhaustion of interface electrons), this equation leads to

$$\frac{d}{dt}F_p(t) = \frac{\alpha}{d_p}\frac{d}{dt}V_d(t) \tag{3.32}$$

In other words, F_p follows V_d as in an ordinary layered capacitor. Moreover, the transfer current becomes zero, as equation (3.28) shows. Second case: the electrical field is below the threshold field, so that $\mathbf{T}[F_p] \approx 0$ follows. This is the case in the relaxed state and the compensated state. The current then becomes zero (equation 3.28) and again equation (3.32) is obtained for the field in the phosphor layer. The TFEL device shows the behavior of an ordinary layered capacitor.

3.2.4 Differential Equation for the Interface Charge

Similarly, if F_p in equation (3.28) is substituted with (3.10), one gets the differential equation for the interface charge :

$$\frac{d}{dt}Q_I(t) = (Q_{I0} - Q_I(t))\,\mathbf{T}\left[\frac{1}{d_p}(\alpha V_d(t) - \frac{Q_I(t)}{C_p + C_i}\right] \tag{3.33}$$

This differential equation is equivalent to the differential equation (3.30) for the field.

3.2.5 Transfer Current

To obtain the transfer current $I_t(t)$, either the interface charge $Q_I(t)$ or electrical field $F_p(t)$ in the phosphor layer as a function of time need to be known. If the interface charge $Q_I(t)$ is known, the transfer current $I_t(t)$ is obtained by differentiation of $Q_I(t)$ with respect to t. If the field $F_p(t)$ is known, the transfer current is

obtained by differentiating equation (3.29) with respect to t. The transfer current is then

$$I_t(t) = (C_p + C_i)\left(\alpha \frac{d}{dt} V_d(t) - d_p \frac{d}{dt} F_p(t)\right) \quad . \tag{3.34}$$

The transfer current can also be calculated directly without differentiation when Q_I on the right side of equation (3.28) is substituted with equation (3.29):

$$I_t(t) = (Q_{I0} - (C_p + C_i)\{\alpha V_d(t) - d_p F_p(t)\})\,\mathbf{T}\,[F_p(t)] \tag{3.35}$$

3.2.6 Comparison with Measurement

The transfer current as a function of time ($I_t - t$-characteristic), the transferred charge-voltage characteristic and the transferred charge versus driving frequency are simulated for the steady state regime and compared with measured data. Since the $F_p - t$ - characteristic of the TFEL is is given by a single first order differential equation, a standard numerical solver can be used. For all following simulations, the field equation (3.30) has been solved with a solver of the MATLAB software package. Subsequently, the transferred charge and the transfer current is calculated with equation (3.29) and (3.28). It is essential to choose an suitable numerical solver because otherwise inaccurate solutions are obtained, for example oscillating solutions. It became apparent that a stable solution is found with the solver ode23tb (low order method for stiff differential equation, for details see MATLAB package [30]).

The initial value is the interface charge $Q_I(0)$. This charge is to zero for the first half period. For obtaining the steady state regime, the initial charge is set zero for the calculation of the first half period, subsequently the transferred charge of the previous calculation is taken as the initial charge for all following calculations. This process is repeated until a stable value for Q_I is found (typical after 10

iterations). The parameters used for the simulations are listed in Table B.2 of the appendix.

A comparison of the the I_t-t characteristic is made between simulation and measurement in Figure 3.3. As can be seen, the simulation of the non annealed device is in good agreement with the measured characteristic. The interface electron density $n_0 = 5 \cdot 10^{12}$ cm^{-2} and the interface level $E_I = 1.16$ eV has been obtained by trial.

Furthermore, the transferred charge as function of driving voltage (Q_t-V-characteristic) and the transferred charge as a function of the driving frequency (Q_t-f_d-characteristic) are simulated and compared with measured characteristics, see Figure 3.4(ii) and 3.5. The transfered charge Q_t is the difference of the final interface charge after one half period and the interface charge at $t = 0$, $Q_t = Q_I(T_d) - Q_I(0)$. A good fit is obtained for an interface electron density $n_0 = 10^{14}$ cm^{-2} and the interface level $E_I \approx 1.3$ eV, which is in discrepancy with the results obtained from the simulation of the $I_t - t$-characteristic.

An explanation for the discrepancy might be that many different solutions (pairs of parameter E_I and n_0) could be possible for a fit of the $I_t - t$—curve. If this is the case, many different measurements are then necessary in order to exclude wrong solutions and to find a unique solution. As a conclusion, a single measurement of the transient characteristic for one driving waveform does not suffice to calculate back the interface electron density and the interface level.

The $I_t - t$ characteristic of a thermally annealed device is presented in Figure 3.3. Compared to the non annealed device, it is clear to see that the rise of the current occurs about 10 μs earlier and the decay time is longer compared to the non-annealed device. This is in agreement with the softening of the brightness-voltage-characteristic and a shift of the threshold voltage towards lower voltage

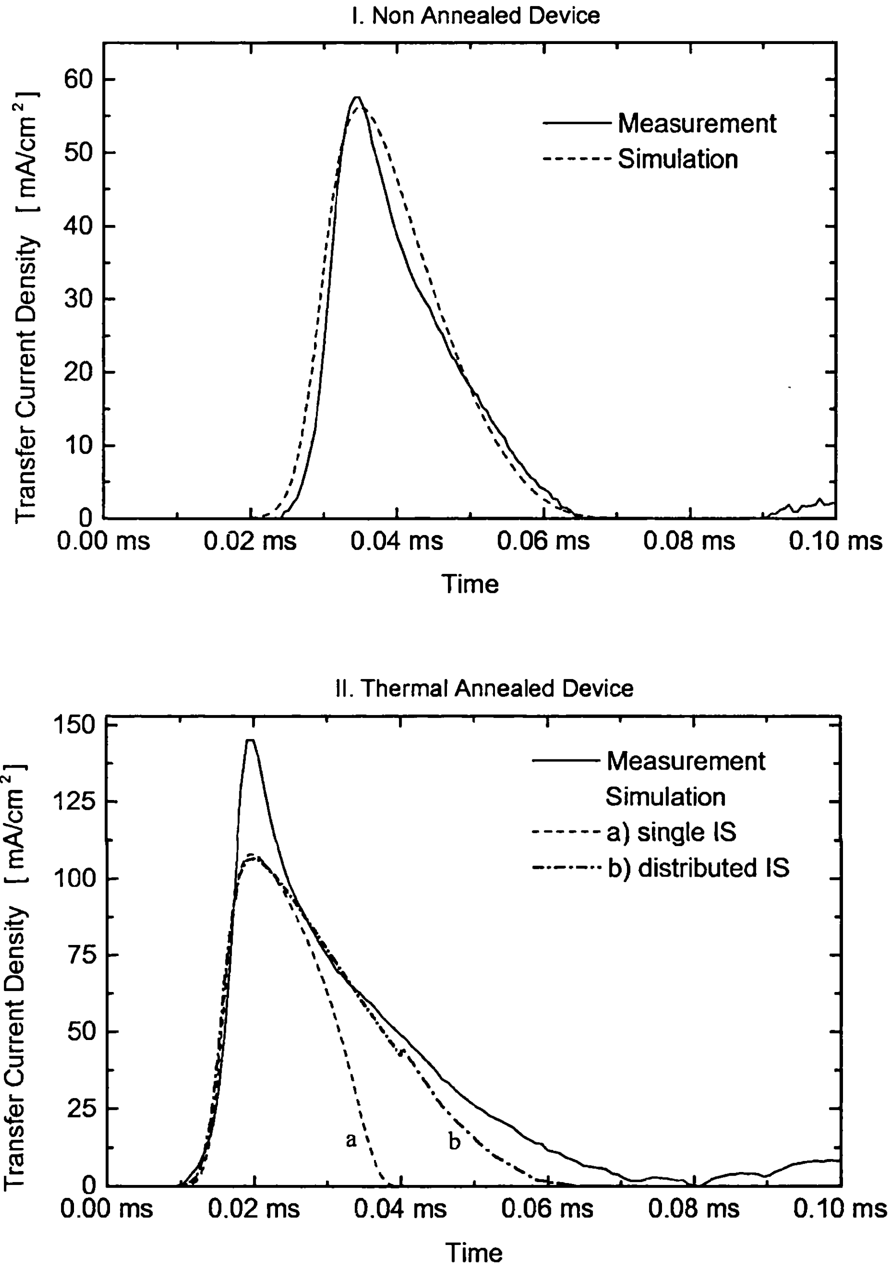

Figure 3.3: Transfer current density as function of time for sine wave stimulus with $V_d = 270$ V and $f_d = 5$ kHz in steady state regime:
I. non annealed device (jr2b): simulation $E_I = 1.16$ eV, $n_0 = 5 \cdot 10^{12}$ cm^{-2}
II. thermal annealed device (jr2a): simulation
a) with single interface state at $E_I = 0.9$ eV, $n_0 = 5 \cdot 10^{12}$ cm^{-2}
b) with distributed interface states as shown in Figure 3.10

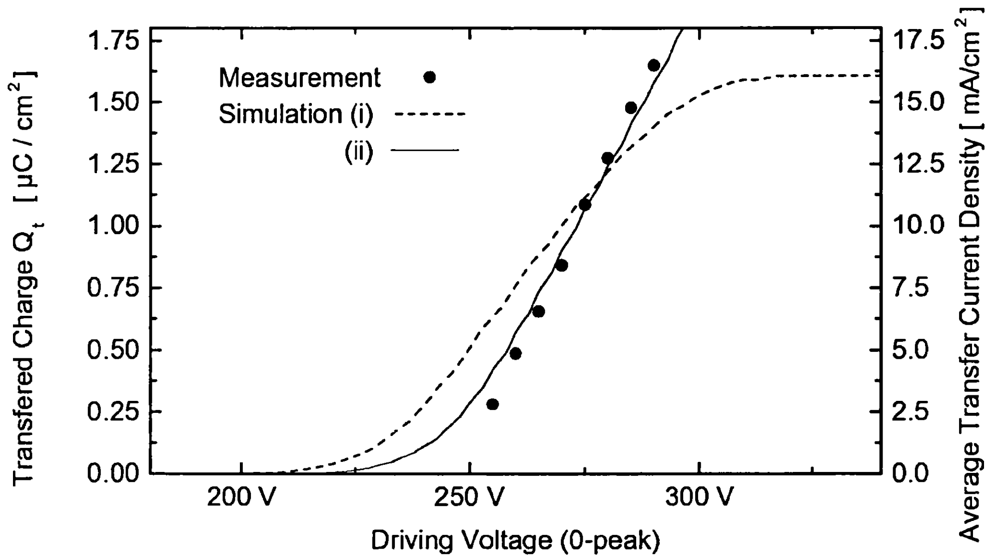

Figure 3.4: Q_t-V_d characteristic in steady state regime; transferred charge after one half-wave, stimulus: sine waveform $f_d = 5$ kHz, measurement: device jr3b (non annealed), simulation: (i) $E_I = 1.16$ eV, $n_0 = 5 \cdot 10^{12}$ cm^{-2} (as in Fig. 3.3), (ii) $E_I = 1.3$ eV, $n_0 = 10^{14}$ cm^{-2} (estimated)

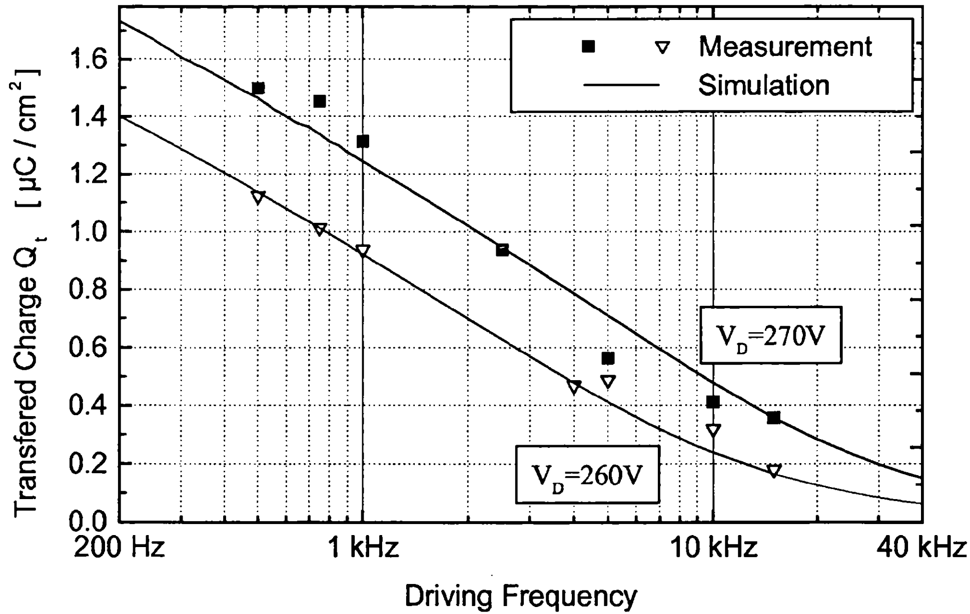

Figure 3.5: $Q_t - f_d$-characteristic in steady state regime; stimulus: sine waveform, device jr3b (non annealed) , simulation: $E_I = 1.32$ eV, $n_0 = 10^{14}$ cm^{-2} (estimated)

due to thermal annealing, experimentally observed in [3]. It is assumed that the change in the B-V-characteristics is related to a change in the interface electron distribution. However, a satisfying fit of the simulation with the measured data seems not to be possible with the single interface model. A model with distributed interface states will be examined later in section 3.4.3.

3.3 Electrical Characterisation by Simulation

3.3.1 Transient Characteristics

A simulation of transient characteristics of the field in the phosphor layer, the transfered charge, the transfer and device current has been done for the device jr2 with a device area of A=0.785 mm^2. The stimulus is a sine wave with a voltage of 270 volt. Figure 3.6 shows a simulation for a device with an initial interface charge $n_{I0} = 5{\cdot}10^{12}$cm^2. The amount of interface charge is lower than the maximal transferable charge at 270 V. As the simulation for the interface level $E_I = 0.9$ eV shows, nearly all charges are transferred. The electrical field in phosphor layer is 'clamped' above threshold until all interface charges are transferred. After all charges are transferred, the field in the phosphor layer follows again the applied external field. Also remarkable, the transfer current for different interface levels starts and ends flowing at different times.

The simulation shown in Figure 3.7 is done for a device with an initial interface charge $n_{I0} = 10^{14}$cm^2. The amount of interface charge is higher than the maximal transferable charge at 270 V. Consequently, charges are transfered until the field in the phosphor layer goes below threshold field strength. The electrical field in the phosphor layer is 'clamped' above a certain field strength. The transfer current for different interface levels starts flowing at different times and ends at

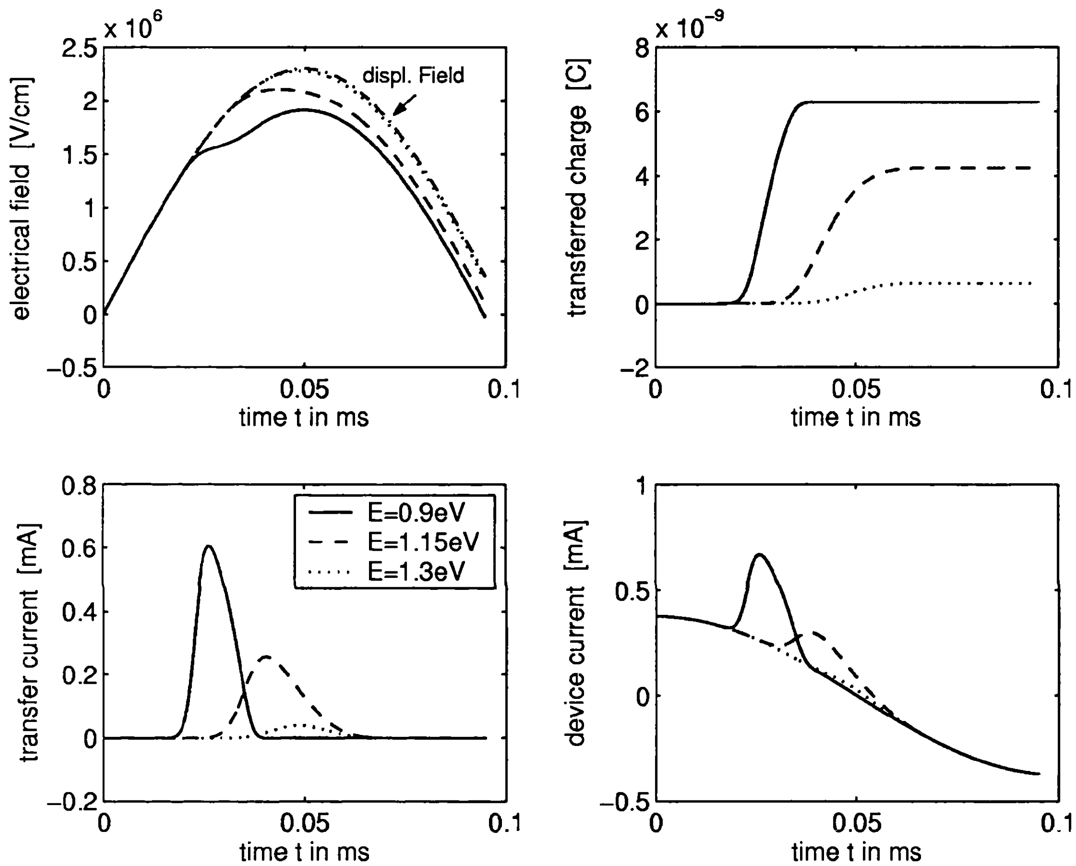

Figure 3.6: Simulation of transient characteristics: field in the phosphor layer, transfered charge, transfer and device current for different interface levels; $n_{I0} = 5 \cdot 10^{12}\text{cm}^2$, stimulus sine wave 270 volt, device jr2

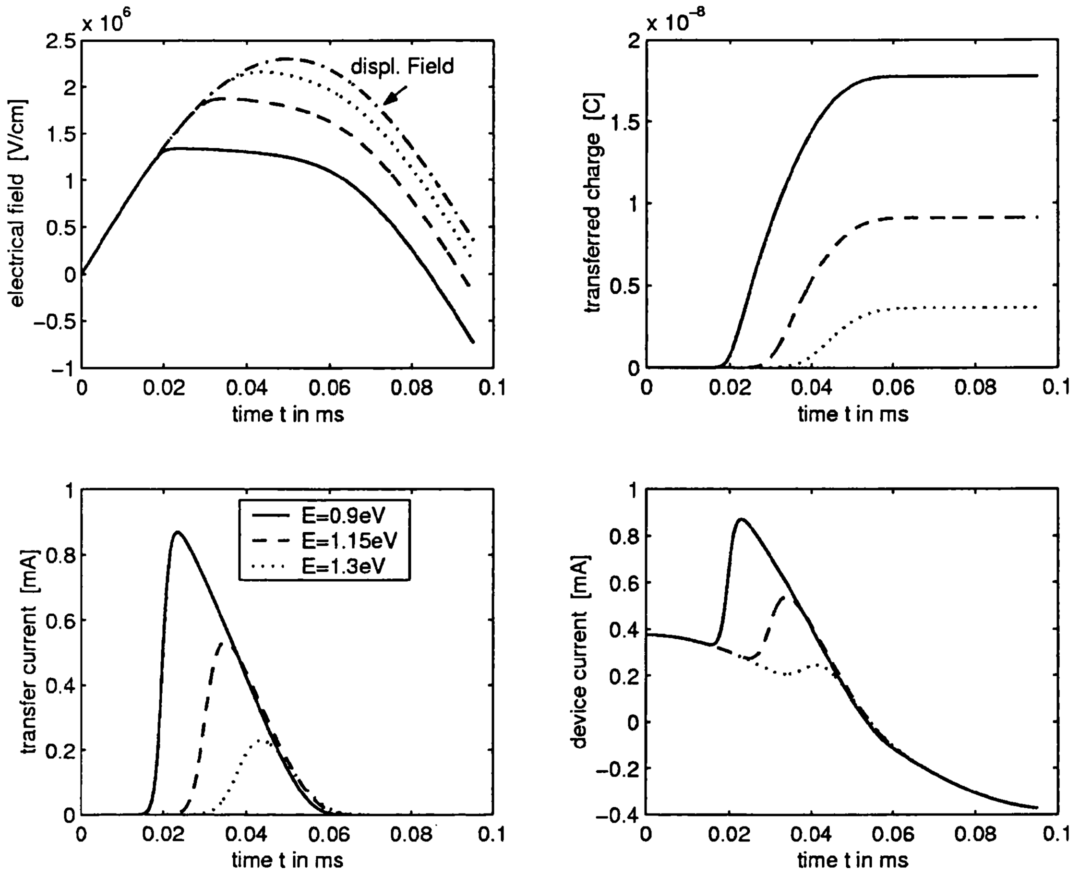

Figure 3.7: Simulation of transient characteristics: field in the phosphor layer, transfered charge, transfer and device current for different interface levels; $n_{I0} = 10^{14}\text{cm}^2$, stimulus: sine wave 270 volt, device jr2

the same time indicating that not all interface charges are transferred.

3.3.2 Current-Frequency-Characteristic

Figure 3.8 shows transfer current and transfered charge upon driving frequency. The transfered charge denotes here the charge transfered in one half period. The higher the frequency the less time to transfer charge and as a consequence, the transfered charge decreases with increasing frequency. The transfer current is the average current, i.e. the transfered charge per second. The higher frequency the more cycles per seconds to transfer charge and thus cause an increasing current.

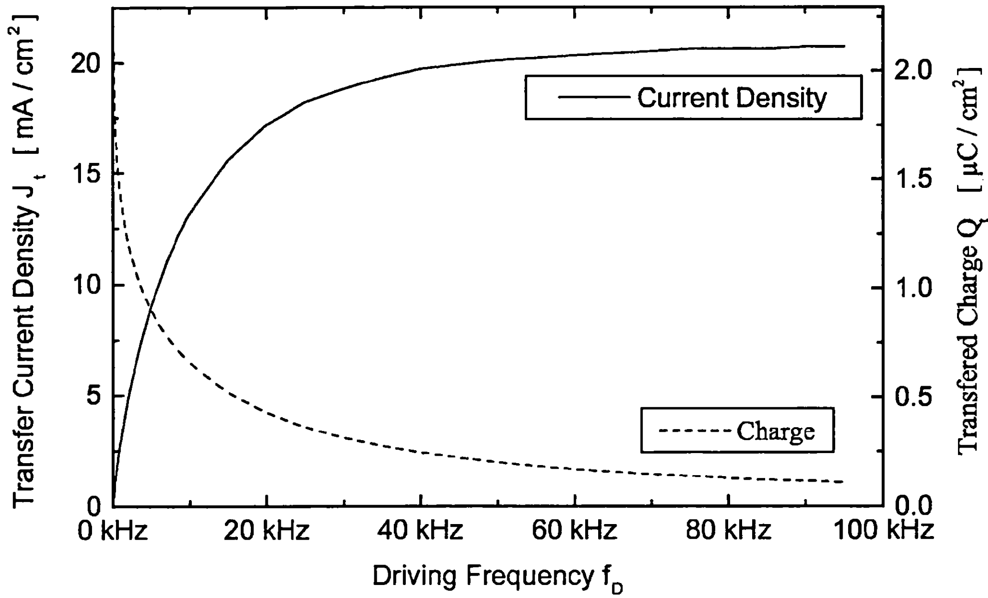

Figure 3.8: Simulation of Transfer Current and Transferred Charge versus Driving Frequency: $V_d = 270\text{V}$, $E_I = 1.3$ eV, $n_0 = 10^{14}$ cm^{-2}

The graph indicates a linear dependency below 10 kHz. The current is limited above 20 kHz. The limitation of the current can be explained as the number of cycles increases , whereas the amount of transfered charge per cycle decreases with an increasing frequency.

3.3.3 Transfered Charge versus Initial Charge

The interface charge $Q_I(T_d/2)$, which is obtained after one half-wave, depends on the interface charge $Q_I^*(t = 0)$, denoted as initial anodic charge, at the beginning of the half-wave. This initial anodic charge has to be taken into account in the simulation as an initial condition. The presence of an initial anodic charge causes an electrical field, which add to external applied field and thus enhances the transfer current. Figure 3.9 shows the interface charge after one half-wave as a function of the initial anodic charge. The dashed line $Q_I(T_d/2) = Q_I^*(0)$ locates the steady state regime. For the given device and driving waveform, the steady

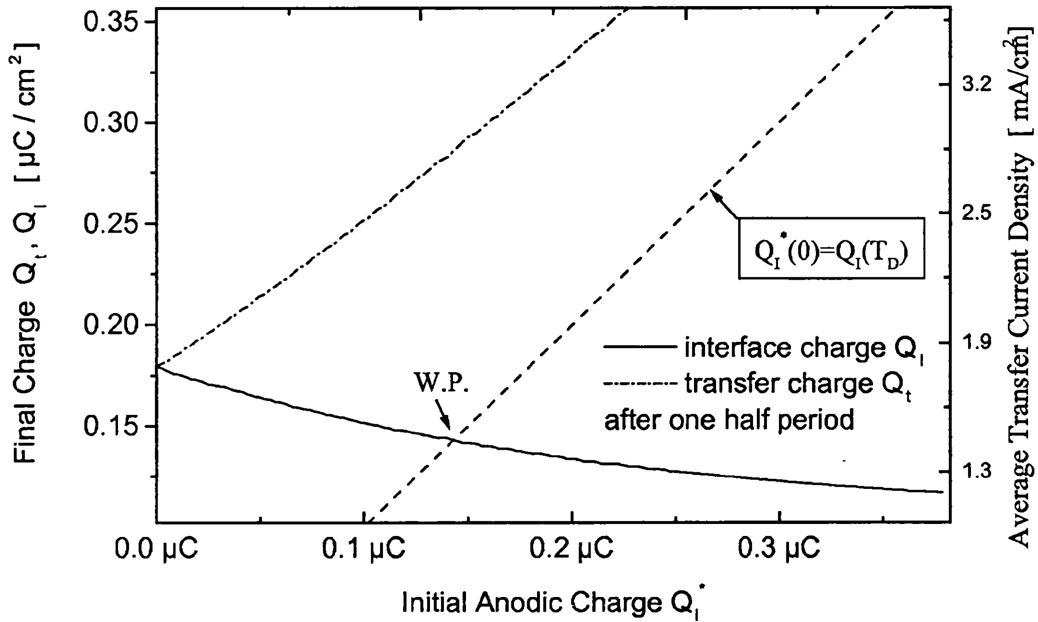

Figure 3.9: Simulation of transfered charge Q_t and interface charge Q_I after one half wave as a function of the initial anodic charge $Q_I^*(t=0)$, $V_d = 270$V, $E_I = 1.3$ eV, $n_0 = 10^{14}$ cm^{-2}, $f_d = 5$kHz, W.P. - steady state working point

state working point is the cross point of the dashed lined with the function of the interface charge. If a TFEL device is switched on, the initial anodic charge is zero. The working points travels along the function of the interface charge until the steady state point is reached. The steady state point is the fix point of $Q_I(T_d/2)$-$Q_I^*(0)$-function.

3.4 Dynamic TFEL Characteristics for Distributed Interface States

The simulation model presented in section 3.2 is based on the assumption that all interface electrons are located at one defined energy level. This might lead to inaccurate results, since the interface electrons are, in reality, rather continously distributed throughout the band gap of the phosphor material. Distributed inter-

face states cause, for example, a smoothing of the B-V-characteristic [3] or can even cause a double peak in the B-V-characteristic [21]. For these reasons, the simulation is refined in this section by introducing a distributed interface electron density.

3.4.1 Assessment of Interface State Properties

Interface states represent additional energy terms within the forbidden bandgap, which act as traps. They can capture and release electrons. As for the Si-SiO_2 interface, interface states are found to be widely separated from one another on the interfacial plane. Interface states are found to be closely spaced in energy and distributed throughout the entire silicon bandgap [31, Sec. 5.2].

Two simple interface state distributions are most likely, a constant distribution over the entire bandgap , $N_S(E) = N_0/E_g$, and a Gaussian distribution $N_S(E) = \frac{N_0}{E_g}\frac{1}{\sigma\sqrt{2\pi}} \exp -\frac{(E-\mu)^2}{2\sigma^2}$. The Gaussian distribution assumes, that a particular bonding with a specific bonding energy is open, so that the interface states are scattered with a certain probability around a mean value. If the interface state distribution $N_s(E)$ is know, the interface electron distribution in thermal equilibrium is calculated with the occupancy function f_0 :

$$n_I(E) = N_S(E) f_0(E) \tag{3.36}$$

where the occupancy function is

$$f_0(E, E_F) = \frac{1}{1 + g\exp(\frac{E-E_F}{kT})}$$

and E_F is the Fermi Energy, g is the degeneracy factor with $g = 1/2$ for donor-like traps [31]. The Fermi level is determined by the total interface electron density

n_I:

$$n_I = \int_0^{E_g} N_S(E) f_0(E, E_F) dE \tag{3.37}$$

If the thermal equilibrium of the interface electron distribution (internal equilibrium) is perturbed, for instance due to emission of electrons, relaxation process towards thermal equilibrium takes place. The relaxation processes are due to thermal stimulation (phonon interaction) or spontaneous and induced transitions (black body radiation) [32]. Hence, the time to reach an equilibrium after perturbation depends on the temperature among other things which include the transition probability, capture cross section etc. For those reasons, it is difficult to estimate the relaxation behaviour.

3.4.2 Electron Emission from Distributed Interface States

Since interface electrons are continously emitted and retrapped during the operation of the TFEL, the interface electron density $n_I(t, E)$ changes with time. Note, that the interface electron distribution $n_I(t, E)$ denotes the amount of electrons per area for the energy interval $[E, E + dE]$. Under an applied field, electron tunneling occurs from all energy levels. Therefore, the contributions of all states are integrated in order to obtain the total transfer current:

$$I_t(t) = q_0 A \int_0^{E_g} n_I(t, E) \mathbf{T} \left[F_p(t), E \right] dE \tag{3.38}$$

The integration is done over the whole bandgap. The initial interface electron distribution $n_{I0}(E)$ is the interface electron distribution in the relaxed state (flatband case, thermal equilibrium). Similar to equation (3.23), the total interface charge is then the difference of the momentary interface electron distribution and the initial interface electron distribution, where all differences must be integrated

over the whole energy range:

$$Q_I(t) = -q_0 A \int_0^{E_g} (n_I(t,E) - n_{I0}(E))dE \tag{3.39}$$

The transfer current is obtained from this equation when the transfer charge is differentiated with respect to the time t:

$$I_t(t) = \frac{dQ_I}{dt} = -q_0 A \int_0^{E_g} \frac{d}{dt} n_I(t,E)dE \tag{3.40}$$

Equating this equation with (3.38) and subsequently differentiating all with respect to energy E leads to

$$\frac{d}{dt} n_I(t,E) = -n_I(t,E)\mathbf{T}\left[F_p(t),E\right] \quad . \tag{3.41}$$

The above differential equation describes the change (kinetics) of the interface electron density for a given energy level solely due to electron emission. The equation is not valid if an exchange of electrons between different interface states occurs, as is the case when relaxation processes take place (see previous section). It is assumed, as known from SiO_2-Si-interface characteristics, that relaxation processes are much slower than the perturbation (caused by the alternating external field). Of course, this assumption need to be proved experimentally [3].

If the thermal equilibrium is reached faster than the perturbation takes place, because of higher temperature or lower driving frequency, a kinetic differential equation for the interface charge can be given by using (3.37) and (3.38)

$$I_t(t) = \frac{dQ_I}{dt} = q_0 A \int_0^{E_g} N_S(E) f_0(E, E_F(Q_I))\mathbf{T}\left[F_p(Q_I),E\right]dE \tag{3.42}$$

where the Fermi energy is a function of the interface charge (3.37).

3.4.3 TFEL with Distributed Interface Charge

The formula in the subsection before is developed for a continuous interface electron distribution. For a practical numerical simulation, the interface electron distribution is approximated as peak-like function (multiple discrete levels). The energy range of the band gap is divided in m discrete energy levels E_n with $n = 1 \ldots m$. Each energy level has a specific electron interface density. For instance, $n_{I.n}(t)$ denotes the number of electrons per area for n.th energy level at the time t. Similarly, let $n_{I0.n}$ be the initial interface electron density for the n.th energy level in the relaxed state (flat-band condition), the initial interface charge for the n.th energy level is then

$$Q_{I0.n} = Aq_0 n_{I0.n} \tag{3.43}$$

and the interface charge for a single energy level is the difference of momentary and initial electron concentration:

$$Q_{I.n}(t) = -q_0 A(n_{I.n}(t) - n_{I0.n}) \quad . \tag{3.44}$$

The total interface charge is the sum of the interface charge of all energy levels :

$$Q_I(t) = \sum_{n=1}^{m} Q_{I.n}(t) \tag{3.45}$$

Similar to equation (3.26), the transfer current due to electron injection from the n.th energy level is

$$\begin{aligned} I_{t.n}(t) &= q_0 A n_{I.n}(t) \mathbf{T}_n \left[F_p(t)\right] & (3.46) \\ &= \left(Q_{I0.n} - Q_{I.n}(t)\right) \mathbf{T}_n \left[F_p(t)\right] & (3.47) \end{aligned}$$

where equation (3.43) and (3.44) have been used and the tunnel function $\mathbf{T}_n[F_p] \equiv \mathbf{T}[F_p, E_n]$. The total transfer current follows then by adding up the injection currents of all energy levels:

$$I(t) = \sum_{n=1}^{m} I_{t.n} = \frac{d}{dt} Q_I(t) = \sum_{n=1}^{m} \frac{d}{dt} Q_{I.n}(t) \tag{3.48}$$

and finally, with the expression for the current $I_{t.n}$ (3.47), one gets the differential equation

$$\sum_{n=1}^{m} \left\{ \frac{d}{dt} Q_{I.n}(t) - (Q_{I0.n} - Q_{I.n}(t)) \, \mathbf{T}_n \left[\frac{\alpha}{d_p} V_d - \frac{1}{d_p} \frac{1}{C_p + C_i} \sum_{n}^{m} Q_{I.n} \right] \right\} = 0 \tag{3.49}$$

which describes the transient characteristics of the interface charges $Q_{I.n}$, where the driving voltage is the independent stimulus function. The above equation leads to a system of m differential equation

$$\frac{d}{dt} Q_{I.n}(t) + (Q_{I.n}(t) - Q_{I0.n}(t)) \, \mathbf{T}_n \left[\frac{\alpha}{d_p} V_d - \frac{1}{d_p} \frac{Q_I}{C_p + C_i} \right] = 0 \tag{3.50}$$

where $n = 1 \ldots m$. The system to solve consists of m first order differential equation, which are all connected together with the total charge Q_I, given by equation (3.45). This system is used for simulation of TFELs with a discrete interface electron distribution.

3.4.4 Comparison with Measurement

The simulation of the $I_t - t$-characteristic is done with the TFEL model with distributed interface electrons, as mathematical represented by equation (3.50). That system of first order differential equations can be solved with a standard

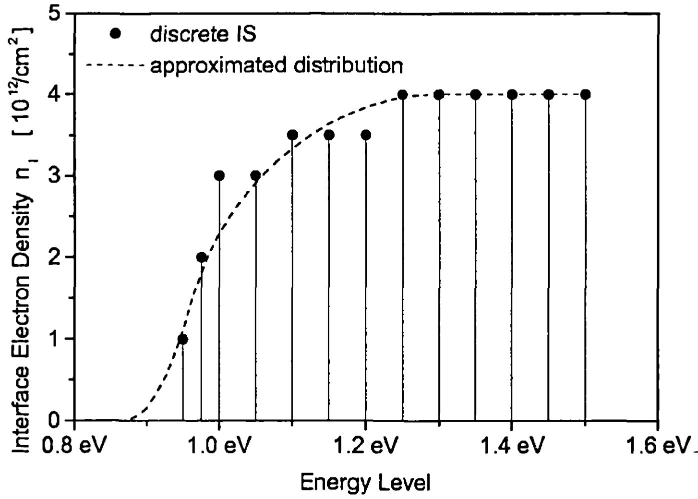

Figure 3.10: Interface Electron Distribution used for simulation, energy is counted downwards from the valence band minimum

numerical solver of the MATLAB package. The solver ode23s (low order method for stiff differential equation, for details see MATLAB package [30]) produced the most stable results. The initial value is a vector with the interface charge $Q_{I.n}(0)$ for each energy level at the time $t = 0$. For the steady state regime, these interface charges are found iteratively, similar to the single interface state model (see 3.2.6). The device parameter used for the simulation are listed in table B.2 of the appendix. The electron interface distribution is found by trial and is shown in Figure 3.10.

The simulated and measured I_t-t-characteristic for the thermal annealed device is compared in Figure 3.3IIb. The simulation with distributed interface electrons shows a much better agreement with the measured characteristic than the simulation with the single interface state model. Especially the decaying part (tail) of the graph is more accurate, whereas the exact peak current could not be achieved.

3.5 Measurement of the Interface Electron Distribution

The measurement of the interface electron distribution has been undertaken by the author with the method presented in [5]. However, problems were encountered, which are pointed out here. The method is carried out by applying a stimulus driving voltage and measuring the transfer current as function of time. Knowing $V_d(t)$ and $I_t(t)$, the transfered charge $Q_t(t)$ and the field $F_p(t)$ in the phosphor layer as a function of time can be calculated as described in section 3.1.3. As derived in [5], the transfered charge can be expressed as

$$Q_t(t) = q_0 A \int_0^{E_g} \left[1 - \exp\left(-\int_0^t \mathbf{T}\left[F_p(\tau), E\right] d\tau\right)\right] n_{I0}(E) dE \tag{3.51}$$

For a practical measurement, the time is divided in discrete time steps t_i, so that the voltage and the current is measured at these time points. The interface electron distribution is also divided in discrete intervals as explained in section 3.4.3. Equation (3.51) becomes

$$Q_t(t_i) = q_0 A \sum_{j=1}^{n_g} \left[1 - \exp\left(-\int_0^{t_i} \mathbf{T}\left[F_p(\tau), E_j\right] d\tau\right)\right] \cdot n_{I0.j} \tag{3.52}$$

This equation can be rewritten in a matrix form:

$$\underline{Q} = \underline{\underline{\Psi}} \cdot \underline{n} = \sum_{j=1}^{n_g} n_{I0.j} \cdot \underline{\psi}_j \tag{3.53}$$

where the matrix $\underline{\underline{\Psi}}$ and the column vectors $\underline{\psi}_j$ are

$$\underline{\underline{\Psi}} = \left[\underline{\psi}_j\right] = \left[\psi_{i.j}\right] = \left[q_0 A \left(1 - \exp\left(-\int_0^{t_i} \mathbf{T}\left[F_p(\tau), E_j\right] d\tau\right)\right)\right] \quad , \tag{3.54}$$

the vector of the transfered charge is $\underline{Q} = [Q(t_i)]$ and the vector of interface electron density is $\underline{n} = [n_{I0.j}]$. The vector $\underline{Q}$ is measured and the matrix $\underline{\underline{\Psi}}$ can be calculated since the field in the phosphor layer is known. The vector $\underline{n}$, containing the interface electron distribution for each energy level, is the unknown variable and must be found. The concept presented in [5] is to find $\underline{n}$ by solving system 3.53. This can be done by calculating the inverse matrix of $\underline{\underline{\Psi}}$, provided the matrix $\underline{\underline{\Psi}}$ is a square matrix, or by using an approximation algorithm. Either way, in order to solve the system, it is an absolute necessary condition that the matrix is nonsingular, or in other words, the vectors $\underline{\psi}_j$ must be linear independent. If the they are not linear independent, the solution is not unique, many different solution (interface electron distributions) are possible to match the current response for a given stimulus. For example, if the set of vectors $\underline{\psi}_j$ is linear dependent, then a vector $\underline{c} = [c_j]$ with constants c_j exits, so that

$$\underline{0} = \sum_{j=1}^{n_g} c_j \cdot \underline{\psi}_j \quad and \quad \exists c_j \neq 0 \tag{3.55}$$

If $\underline{n}$ is one solution of the system 3.53, so is also $\underline{n} + \underline{c}$ a solution because

$$\underline{Q} = \underline{Q} + \underline{0} = \sum_{j=1}^{n_g} (n_{I0.j} + c_j) \cdot \underline{\psi}_j \tag{3.56}$$

which gives the same charge (current) - time response.

These kind of problems were encountered with the measured data. The matrix $\underline{\underline{\Psi}}$ were tested on singularity with MATLAB. It could be proved that the matrix is singular for the given number precision and the used stimulus voltage. Figure 3.11 demonstrates this aspect. It shows a simulation with a) a single interface level and b) with two distinct energy levels. Both distributions produce a similar response of the transfer current. As a conclusion, the estimation of the interface

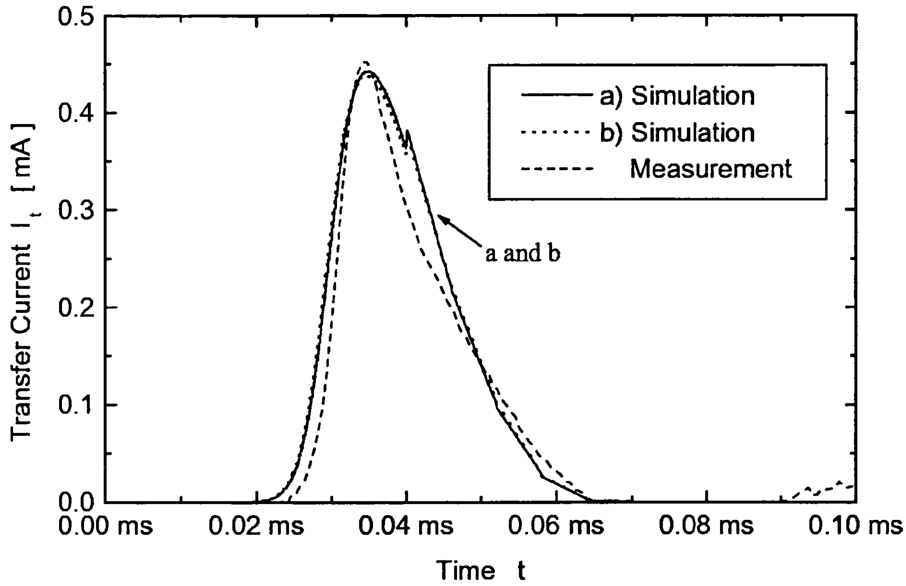

Figure 3.11: Simulation of Transfer Current: a) with one interface state $E_I = 1.16$ eV, $n_0 = 5 \cdot 10^{12}$ cm^{-2}, b) with two interface states $E_{I.1} = 1.14$ eV, $n_{0.1} = 2 \cdot 10^{12}$ cm^{-2} and $E_{I.2} = 1.2$ eV, $n_{0.2} = 6 \cdot 10^{12}$ cm^{-2}; stimulus sine-wave 270V; measurement: device jr2 non-annealed

electron distribution does not seem to be feasible solely by analysing the measured transfer current for one driving stimulus.

There are two possible ways to overcome this problem. One way is that many different measurements are done with different driving waveforms, for instance different driving voltages or driving frequencies, in order to exclude wrong solutions. Another way, a specific driving waveform has to be found. This waveform must produce a nonsingular matrix $\underline{\underline{\Psi}}$, or respectively the functions $\psi_j(t)$ are linear independent.

Chapter 4

Electrical Characteristics of LETFEL Devices on Silicon

4.1 Influence of the MIS-Capacity

The LETFELs as used in this research programme are grown on a silicon wafer, which function as a back electrode. The TFEL stack - Y_2O_3, ZnS, Y_2O_3 - can be considered as an insulator as long as no significant charge transfer occurs in the ZnS layer. These insulator layers along with the metal contact and the silicon substrate form metal-insulator-semiconductor structure (MIS) as known from MOS transistors [26], [34], [33]. MIS effects can thus influence the characteristics of the TFEL device during the operation. Therefore, it is of interest to estimate the change of the TFEL characteristics due to the MIS effects in order to separate MIS effects from the pure TFEL phenomena.

The most important effect to consider is the influence of the space charge layer since the silicon possesses a low carrier concentration. The used silicon is n-conducting and has donor concentration of $N_D \approx 5 \cdot 10^{14} cm^{-3}$. For a n-conducting

silicon, a space charge layer is created when a negative voltage is applied on the metal gate (ground on the bulk). Under these conditions, electrons (majority carriers) are pulled away from silicon insulator (Y_2O_3) surface into the bulk - a depletion of mobile carries occurs. Positively charged donors, which are immovable, remain and form a positive space charge layer, which compensate the field in the semiconductor. Due to carrier generation processes in the silicon and on the silicon insulator surface , holes (here minority carriers) are generated. These holes flow to the surface and form there an inversion layer, which compensate the field in semiconductor and reduce the width of the space charge layer. This process continues until an equilibrium is reached.

The space charge layer in the semiconductor causes a voltage drop, which reduces the voltage across the insulator and consequently influences the characteristic of the TFEL. For example, an asymmetric current characteristic and characteristic of the outcoupled light has been observed for a symmetric driving voltage. This asymmetric behavior can be explained by the characteristics of the MIS structure. A formation of a space charge layer occurs when a negative voltage is applied on the metal gate, whereas a formation of a accumulation layer (layer of mobile carriers) occurs, when a voltage is applied in the opposite direction. The accumulation layer causes, in contrast to the space charge layer, no significant voltage drop. The voltage drop across the space charge layer might result in a shift of the B-V-characteristic towards higher voltage causing a asymmetric B-V-characteristic. The formation of the space charge layer also causes an additional current to the displacement current of the TFEL capacity.

Firstly, the equilibrium state of the MIS structure is investigated in order to find out how much the TFEL characteristic is altered. The MIS structure is in an equilibrium when the total generation rate (surface and space charge layer) of

electrons is equal to the total recombination rate of electrons. The equilibrium is also characterized by the formation of an inversion layer. The analysis of the voltage across the space charge layer is described for a p-type semiconductor in equilibrium in [26] and is here developed for n-type semiconductor. For the typical TFEL, the contact potential (metal semiconductor potential) and the interface charges (Y_2O_3 -silicon) can be neglected for this analysis since the applied device voltage is high. The external device voltage V_d as function of the voltage V_{SC} across the space charge layer is for n-type silicon

$$V_d(V_{SC}) = V_{SC} - \frac{A\epsilon_{Si}F_S(V_{SC})}{C_{ip}} \tag{4.1}$$

where A is the active TFEL area, ϵ_{Si} is the permittivity of the silicon and C_{ip} is the total TFEL capacity. F_S is the electrical field strength at the silicon surface :

$$F_S(V_{SC}) = \sqrt{\frac{4q_0 n_i V_T}{\epsilon_{Si}}\left(\cosh\frac{V_F - V_{SC}}{V_T} - \cosh\frac{V_F}{V_T} + \frac{V_{SC}}{V_T}\sinh\frac{V_F}{V_T}\right)} \tag{4.2}$$

where n_i is the intrinsic carrier concentration ($n_i \approx 10^{10} cm^{-3}$), q_0 is the elementary charge and the thermal voltage $V_T = kT/q_0$, Boltzmann's constant k. V_F is given by donor concentration N_D with $V_F = -V_T \ln \frac{N_d}{n_i}$.

Substitution of F_S in equation (4.1) with equation (4.2) leads to an expression for the device voltage as a function of the voltage drop across the space charge layer. This expression is exact as long as the external device voltage remains below the threshold voltage of the TFEL, i.e. no charges in the insulator-phosphor layers are transfered. The absolute value of device voltage as a function of the voltage drop across the space charge layer is shown in Figure 4.1. It reveals that the voltage drop across the space charge layer is (in both directions) less than 1.5 V for the TFEL device under typical driving conditions and can therefore be neglected if

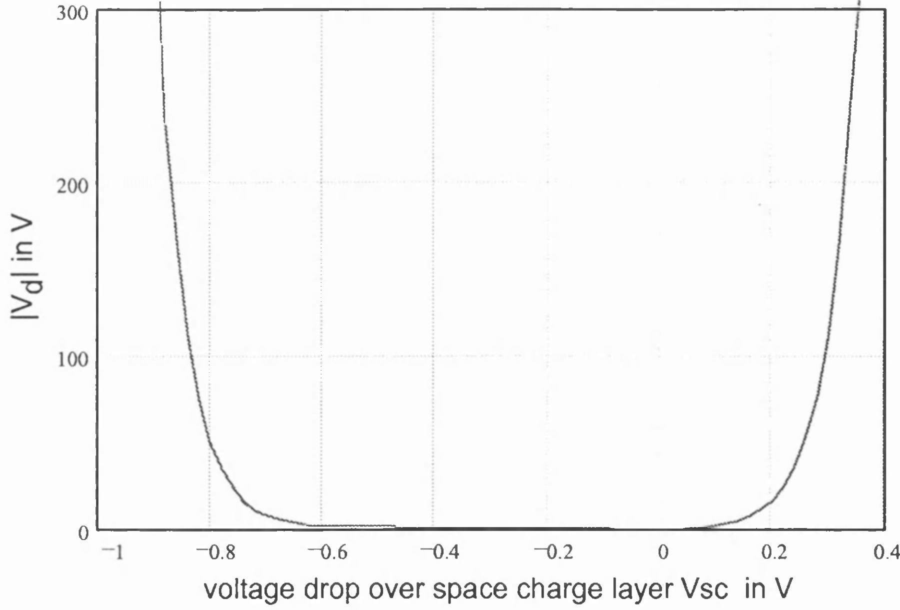

Figure 4.1: MIS in Equilibrium: absolute value of the applied device voltage as function of the voltage drop across the space charge layer for a TFEL with silicon back contact; donor concentration $N_D = 5 \cdot 10^{14} cm^{-3}$

the device has reached the equilibrium state. The equilibrium state can thus not explain the asymmetric characteristics of the LETFEL on silicon.

With this result, it follows that non-equilibrium states need to be analysed in order to explain non-symmetric characteristics. Shortly after applying a voltage step the space charge layer is created, which is depleted of free carriers. Under the assumption that the space charge layer is completely empty of free carriers (deep depletion approximation), the voltage drop across the space charge layer can be estimated as follows [34]:

$$V_{SC} = V_d - V_0 \left(\sqrt{1 + 2V_d/V_0} - 1 \right) \tag{4.3}$$

where $V_0 = N_d \epsilon_{Si} q_0 / C_{ip}^2$. Figure 4.2 shows the voltage drop V_{SC} across the space charge layer as function of the applied device voltage. As can be seen, the voltage drop is high, which means that the TFEL characteristics are strongly influenced

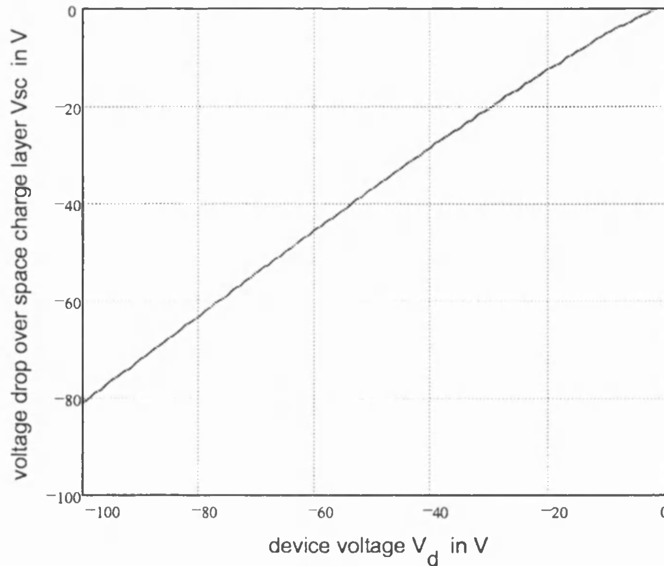

Figure 4.2: MIS in Deep Depletion: voltage drop across space charge layer versus applied device voltage for TFEL with silicon back contact; donor concentration $N_D = 5 \cdot 10^{14} cm^{-3}$

right at the beginning of voltage pulse.

To answer the question of how much the MIS-effect influences the characteristics and efficiency of the LETFEL, it is necessary to investigate how fast the MIS-system returns from the deep depletion, meaning high voltage drop across the space charge layer, to the equilibrium with a negligible voltage drop across the space charge layer.

The state of deep depletion occurs shortly after a voltage step (rectangular driving voltage) is applied to the device. Since the number of carriers is reduced, the recombination rate is lower than the generation rate of electron-hole pairs. This carrier generation processes during the carrier depletion causes the device to return to the equilibrium. Important factors, which influence this relaxation process, are the generation in the space charge region (I_{SC}), generation and diffusion of carriers from the bulk (I_D) and generation on surface (G_S). Generation in the space charge layer can be deduced from the hole mobility μ_p and hole life time τ_p,

which are known material constants for silicon. The surface generation density for insulator-silicon interface needs to be obtained experimentally. The relaxation process is described with differential equation

$$\frac{dV_d}{dt} = \left(1 + \frac{KA}{C_{ip}\sqrt{-2KV_{SC}}}\right)\frac{dV_{SC}}{dt} - \frac{A}{C_{ip}}(I_{SC}(V_{SC}) + I_D + G_S) \qquad (4.4)$$

where $K = N_d \epsilon_{Si} q_0$, the generation current I_{SC} in the space charge layer is

$$I_{SC}(V_{SC}) = q_0 \frac{n_i}{\tau_g}\left(\sqrt{-\frac{2\epsilon_{Si}}{q_0 N_d} V_{SC}}\right)$$

and the diffusion current from the bulk is $I_D = q_0 \frac{D_p}{\sqrt{\tau_p D_p}} \frac{n_i^2}{N_d}$, see [34]. The generation lifetime τ_g, the low level injection hole recombination lifetime τ_p and the hole diffusion coefficient D_p are known material constants. The surface generation density G_S needs to be measured for the Si-Y_2O_3 interface. The differential equation (4.4) can be solved for a rectangle pulse by integrating it once. The solution is subsequently solved numerically in order to get V_{SC} as function of time.

This has been done for a rectangular driving voltage with $V_d = -200$ V, see Figure 4.3. It shows the time response of the voltage drop across the space charge layer after applying a rectangular voltage step. The simulation reveals that the time to return in the equilibrium strongly depends on surface generation rate. If the surface generation rate is high, the MIS-system returns faster to the equilibrium and the influence on the operation of the TFEL is low. Therefore, it is necessary to measure the surface generation rate in order to estimate the influence of the MIS-effect. A way to avoid the influence of the MIS-effect and resulting disadvantages is to use a metal base layer between the TFEL stack and silicon contact.

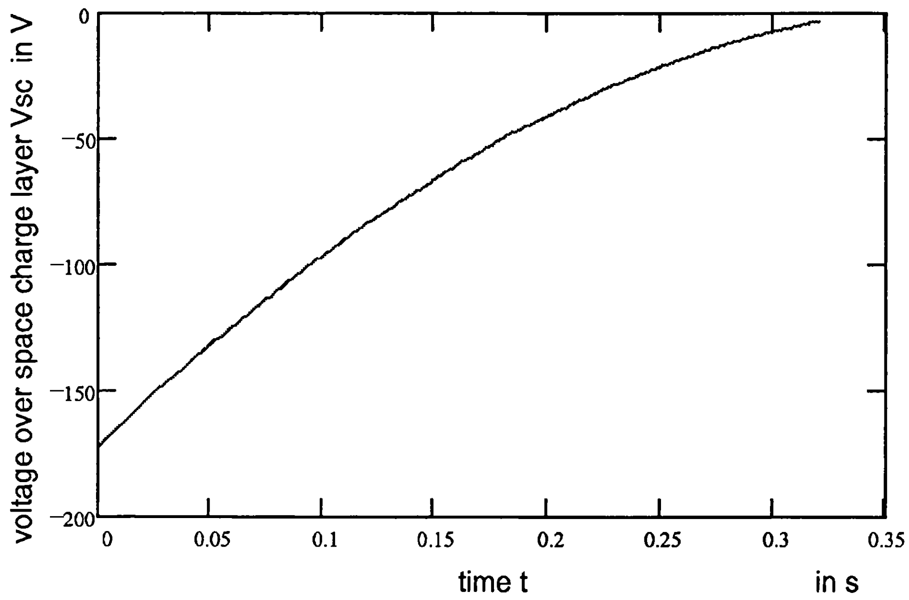

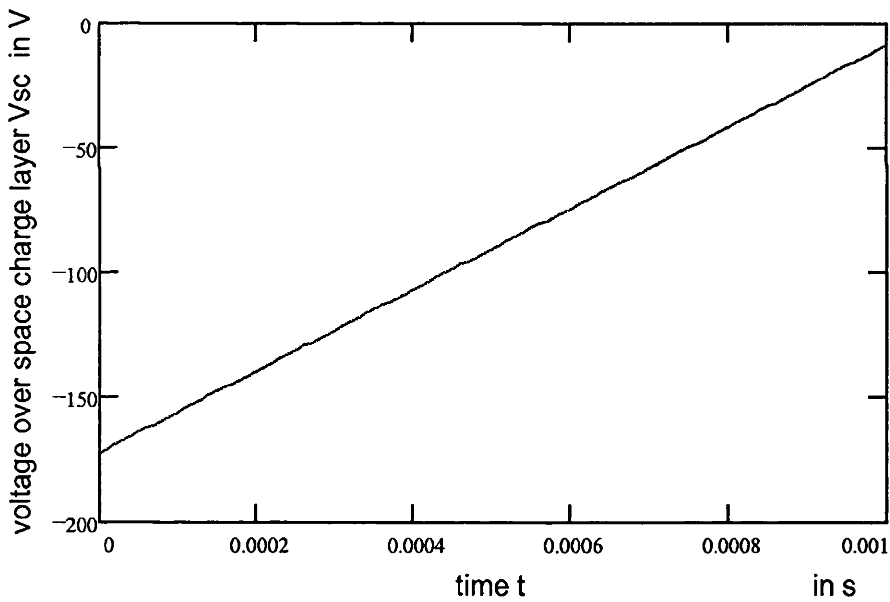

Figure 4.3: MIS Relaxation Process: time response of the voltage across the space charge layer after after applying a rectangular voltage step for TFEL with silicon back contact; surface generation rate
a) $G_s = 0$
b) $G_s = 1mA/cm^2$
applied voltage $V_d = -200V$, donor concentration $N_D = 5 \cdot 10^{14} cm^{-3}$,

4.2 Electrostatic Field Distribution in LETFELs

LETFEL devices operate normally under a high driving voltage with about 300 V to 500 V peak to peak voltage. Because the high voltage drops across very thin dielectric layers (TFEL-stack), a high electrical field strength appears in the insulator and phosphor layers which can lead to the damaging of the device. Therefore, it is essential to study the field distribution in LETFEL devices, especially the field strength between the tip of the micro mirror and a possible second metal layer. Of interest for the study of the field distribution is only the compensated state as a worst case estimation since the entire voltage drops across the insulator layer (Y_2O_3) and therefore, the highest field strength in the insulator layer is expected for this state of operation.

4.2.1 Simulation Method

Simulations of the electric static field distribution for a typical LETFEL device has been performed with the Silvaco Process and Device Simulator [35][36]. A simulation under an alternating driving voltage is not possible because the physical behavior of electron tunneling from interface states is not implemented in the simulator at the present time. Also the simulator programming interface does not allow the programming of electron tunneling from the interface states. For those reasons and since a transient field simulation is not necessary for a worst case estimation of the electrical field strength, a simulation of the electro static field in a LETFEL has been performed for the compensated state and a typical device voltage.

For an electro static field simulation, it is necessary to obtain the correct relation of transferred charges under an applied voltage. This is achieved by introducing

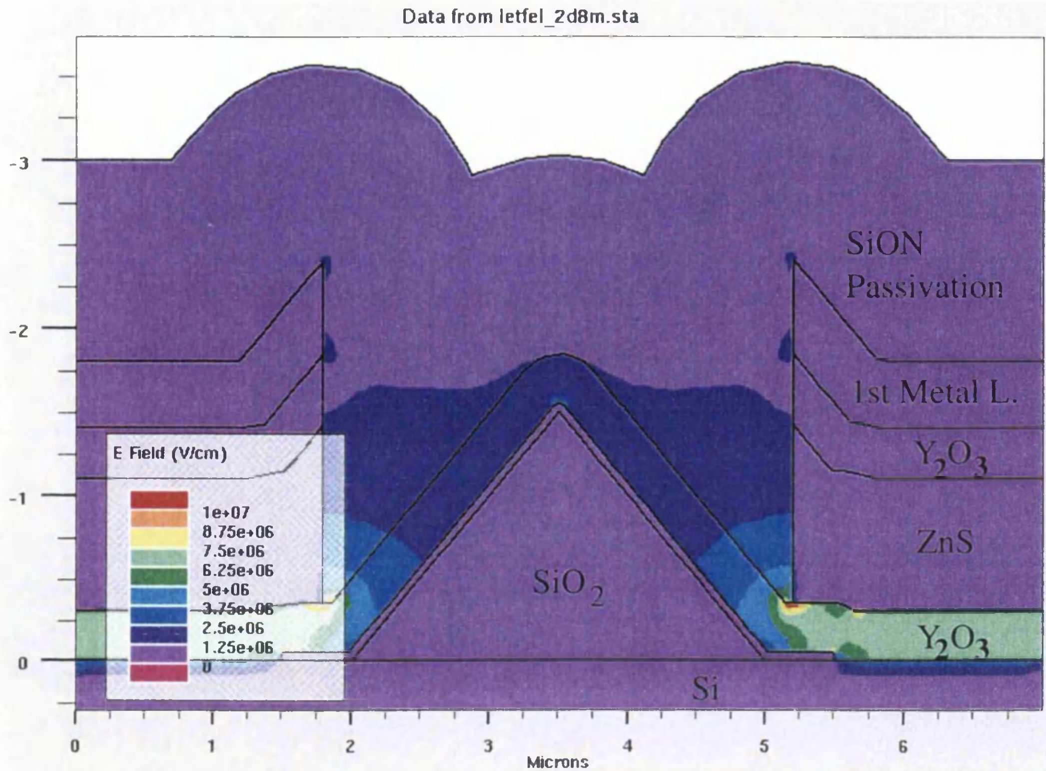

Figure 4.4: Field Distribution in a LETFEL Device for V=200V, etched facets, metalised mirror, mirror metalisation etched, distance between mirror and facet: 0.2 μm

a thin n-doped ZnS layer between ZnS-phosphor and Y_2O_3-insulator layer, which emulates the interface charge layer. The amount of free electrons in this n-doped ZnS layer correspond to the equal amount of transferred charges for a typical LETFEL device. If a voltage is applied, the electrons of the n-doped layers move through the ZnS-phosphor layer to the positive side, thereby creating similar condition as in a LETFEL device in the compensated state. The simulation is done by applying and simulating a stepwise voltage until the final voltage is reached. This procedure ensures convergence of the numerical simulation.

4.2.2 Simulation Results

The simulation has been done for a LETFEL device with a 0.8 μm ZnS-phosphor and a 0.3 μm Y_2O_3 -insulator layer. The concentration and the thickness of the n-doped layer is chosen to be equivalent to an interface electron concentration of $n_I = 10^{14}\text{cm}^{-2}$. Figure 4.4 shows the field distribution in a LETFEL device for an applied device voltage of 200 V. The distance between mirror and facet is 0.2 μm. The mirrors are metalised (reflecting coating). This metalisation continues to 0.5 μm underneath the TFEL stack, which models the production precision. The facets are etched and the display is covered with a SiON passivation. The simulation reveals, as expected, that field concentration occurs on the edges of the facets and on the edge of the metalisation for mirror. The field strength is, according to simulation results, up to 10 MV/cm in Y_2O_3 insulator layer and 7.5 MV/cm in SiON passivation layer. Therefore, sharp edges at and underneath the TFEL stack should be avoided as much as possible.

Figure 4.5 shows the field distribution in a LETFEL device for an applied device voltage of 200 V. The distance between mirror and facet is 1 μm. The mirror metalisation is not etched and runs underneath TFEL stack. Additionally, a second metal layer is on top of the passivation layer. The simulation shows that the field concentration over the tip of the mirror is weak and should not cause any problems. As in the previous example, field concentration occurs on the edges of facets. The field strength is 9 MV/cm in the Y_2O_3 insulator layer and 7 MV/cm in the SiON passivation layer.

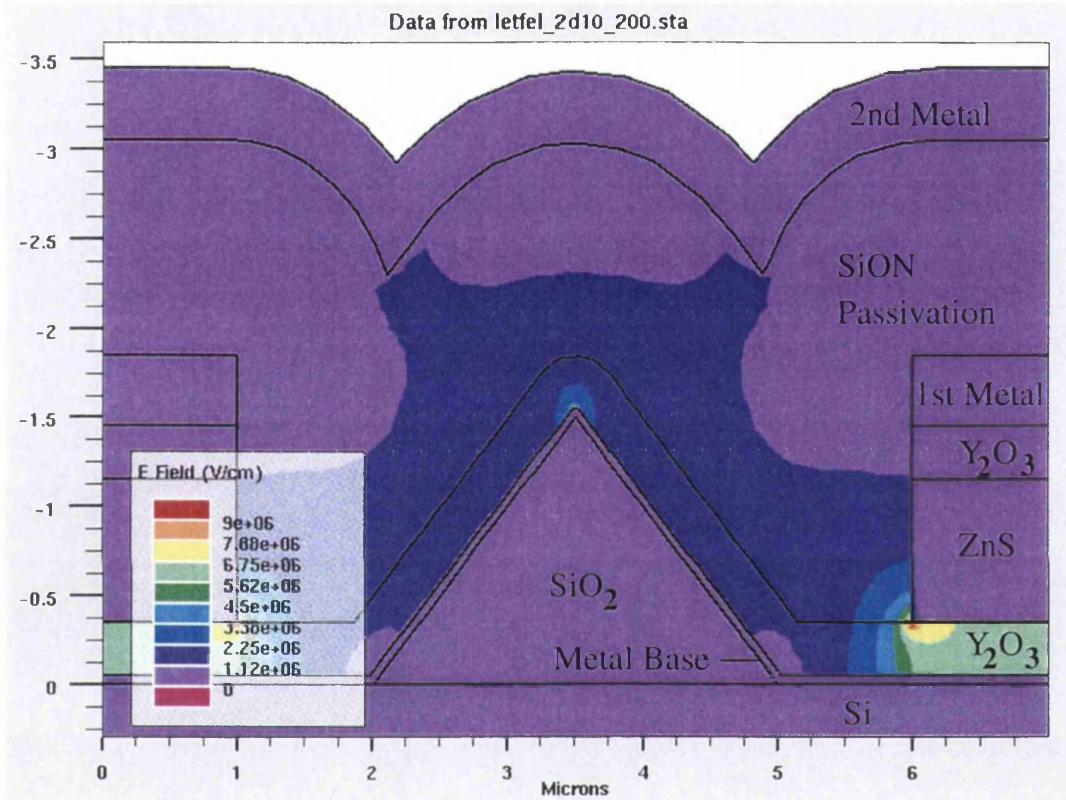

Figure 4.5: Field Distribution in a LETFEL Device for V=200V, etched facets, metalised mirror, with metal base layer and 2nd metalisation, distance between mirror and facet: 1 μm

Chapter 5

RC-Models for TFEL Devices

In this chapter, equivalent nonlinear RC-models are developed for AC thin film electroluminescent devices. These RC models enable the simulation of TFELs and driver electronics with a conventional SPICE-circuit simulator. Several equivalent electrical models for TFEL devices have been developed, for example see [37], [38], [39], [40], [41]. These models are primarily based on observation. The equivalent nonlinear RC models are here derived starting from the physical equations.

The analysis is based on tunneling from interface states as the only electron source, traps and memory effects are not considered in order to keep these models as simple as possible. Therefore, the interface charge distribution is the important parameter to be measured for modeling the TFEL for different driving wave forms. Furthermore, distributed charges in the phosphor layer are neglected. As explained in the previous chapters, those assumptions are quite valid for the Y_2O_3-ZnS LETFEL devices under investigation. The models are developed for the case of a AC-TFEL with single and multiple interface states, as well as for the case of low and high interface charge. They can be used for simulation of driver electronics with different driving wave forms and frequencies. A validation of the models

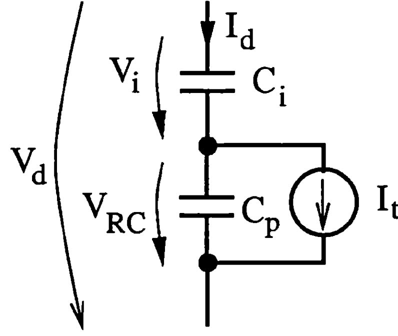

Figure 5.1: Equivalent Circuit for a TFEL, current source represent the transfer current due to tunneling from interface states

is done by comparing the simulation results of the RC-circuit with measured data.

5.1 RC-Model for Layered Structure

As a first step, an RC-model is developed for the layered TFEL structure with an injection current from the insulator-phosphor interface. Hereby, the kind of the injection process (tunneling, phonon assisted tunneling etc.) is not specified yet. If any current source is given as I_t, the device current for the physical model of the TFEL is given as

$$I_d = C_{ip}\frac{dV_d}{dt} + \alpha I_t \quad , \tag{5.1}$$

see equation (A.16) in the appendix. The first term on the right hand side is the the displacement current of an ordinary layered capacitor and the second term represents the transfer current within the phosphor layer. The equivalent circuit of the TFEL structure represented by equation (5.1) is shown in Figure 5.1, where the transfered current due to tunneling from interface states is modeled as a current source. This RC-model is validated by developing the equation for the RC-circuit and comparing it with the equation for physical model of the TFEL.

With the current equation $I_p = C_p \frac{dV_{RC}}{dt}$ for the capacitor C_p and with the equation for the device voltage $V_d = V_i + V_{RC}$, one obtains:

$$I_p = C_p \frac{dV_d}{dt} - C_p \frac{dV_i}{dt}$$

With the equation $I_d = C_i \frac{dV_i}{dt}$ for the capacitor C_i and with the equation for the device current $I_d = I_p + I_t$, this equation becomes

$$I_d = C_p \frac{dV_d}{dt} - \frac{C_p}{C_i} I_d + I_t$$

Solving this equation with respect to I_d, one gets

$$I_d = \frac{C_i C_p}{C_i + C_p} \frac{dV_d}{dt} + \frac{C_i}{C_i + C_p} I_t$$

and finally, by introducing α and C_{ip} as defined in (3.5) previous chapter, the equation for the equivalent RC-circuit is

$$I_d = C_{ip} \frac{dV_d}{dt} + \alpha I_t \tag{5.2}$$

A comparison of this equation with equation (5.1) proves that the RC model is equivalent to the physical model.

5.2 RC-Model for TFELs with Single Interface State

5.2.1 Physical Model of the TFEL

The above model describes the characteristics of the layered TFEL structure. The next step is to find an equivalent RC circuit that describes the current injection

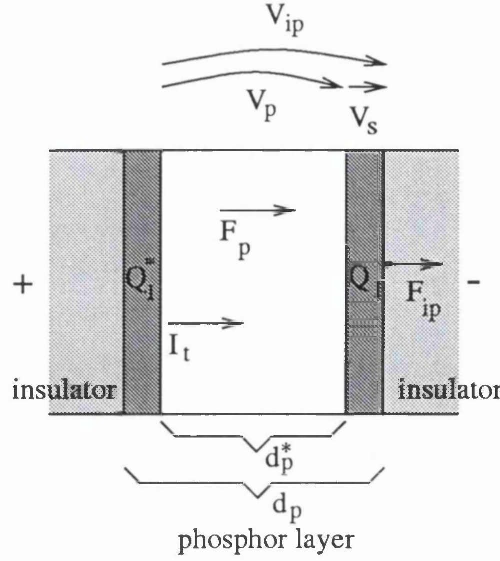

Figure 5.2: Phosphor layer of a TFEL

process in order to replace the current source. For this purpose, the phosphor layer and the interface layers, as shown in Figure 5.2, are analysed independently of the insulator layers. As in the previous chapter, the transfer current in the phosphor layer is

$$I_t(t) = q_0 A n_I(t) \mathbf{T}\left[F_p(t)\right] \tag{5.3}$$

where $F_p(t)$ is the electrical field in the phosphor layer at time t, $n_I(t)$ is the interface electron density, A is the device area, $\mathbf{T}$ is the tunneling function (3.21). The electrical field in the phosphor layer (region d_p^*) consists of two components, the external field F_{ip} at the interface and the field caused by interface charge (Gauss Law) :

$$F_p(t) = F_{ip} + Q_I^*(t)/(A \cdot \epsilon_p) \quad , \tag{5.4}$$

subsequently with $Q_I = -Q_I^*$, for the same reasons as explained in the previous chapter, and C_p:

$$F_p(t) \quad = \quad F_{ip} - Q_I(t)/(C_p d_p) \tag{5.5}$$

$$= \frac{1}{d_p}(V_{ip} - Q_I(t)/C_p) \tag{5.6}$$

where V_{ip} is the voltage across the phosphor layer (including the interface charge layer), $V_{ip} = F_{ip}d_p$, since the interface charge layer is assumed to be thin so that $d_p \approx d_p^*$. Eliminating I_t in equation (5.3) with (3.27) and substitution of n_I with equation (3.25) gives

$$\frac{d}{dt}Q_I(t) = (Q_{I0} - Q_I(t))\,\mathbf{T}\,[F_p(t)] \tag{5.7}$$

and on eliminating F_p with (5.6), one finally obtains the differential equation for the transfered charge in the phosphor layer:

$$\frac{d}{dt}Q_I(t) = (Q_{I0} - Q_I(t))\,\mathbf{T}\left[\frac{1}{d_p}(V_{ip} - Q_I(t)/C_p)\right], \tag{5.8}$$

which is a first order nonlinear differential equation. Since $V_{ip} = \alpha(Q_I/C_p + V_d)$, this differential equation for the transfered charge is equivalent to equation (3.33) but with the difference that the stimulus is the voltage drop across the phosphor layer. The transfer current I_t is obtained by differentiating $Q_I(t)$ with respect to time and the field F_p in the phosphor layer with equation (3.9).

5.2.2 Equivalent RC-Network

The goal here is to develop an electrical circuit that describes the transfer current in the phosphor layer (current source in Fig. 5.1) as given by equation (5.8). The proposed equivalent RC-circuit is shown in Fig.5.3 and includes a nonlinear resistor $G(V_R)$, modeling the tunneling behavior, and a nonlinear capacity $C_S(V_S)$, modeling the current limiting due to the finite number of interface charges. The

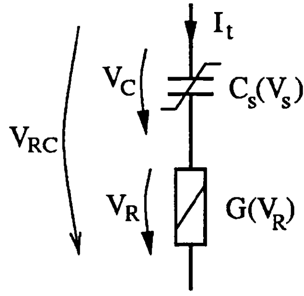

Figure 5.3: Equivalent RC-circuit of the phosphor layer modeling current injection from interface states into phosphor layer

equation for the equivalent circuit is

$$I = \frac{d}{dt} Q_C(t) = G(V_R) \tag{5.9}$$

where Q_C denotes the charge stored in the nonlinear capacitor C_S.

Two cases will be considered: I) the interface charge Q_I is much smaller than initial interface charge Q_{I0} and II) the interface charge is about the same as initial interface charge.

Case I: Under the condition $Q_I \ll Q_{I0}$, the initial charge Q_{I0} can be considered as constant and the differential equation (5.8) for the interface charge reduces to

$$\frac{d}{dt} Q_I(t) = Q_{I0} \mathbf{T} \left[\frac{1}{d_p} (V_{ip} - Q_I(t)/C_p) \right] \quad . \tag{5.10}$$

Assuming for the moment that this equation can be expressed as an equivalent circuit with a linear capacity $Q_C = C_S V_C$. By replacing the voltage $V_R = V_{RC} - V_C = V_{RC} - Q_C/C_S$, equation (5.9) becomes

$$\frac{d}{dt} Q_C(t) = G(V_{RC} - Q_C/C_S). \tag{5.11}$$

If the capacity and the nonlinear resistor is defined as following

$$C_S := C_p \tag{5.12}$$

$$G(V) := Q_{I0}\mathrm{T}\left[V/d_p\right] \tag{5.13}$$

one gets with (5.11) an equation for the equivalent RC-circuit

$$\frac{d}{dt}Q_C(t) = Q_{I0}\mathrm{T}\left[\frac{1}{d_p}(V_{RC} - Q_C/C_S)\right] \tag{5.14}$$

which is equal to physical equation (5.10) and one can identify $Q_s(t) \equiv Q_c(t)$ and $V_{ip} \equiv V_{rc}$. Therefore, the RC circuit in Figure 5.3 together with (5.12) and (5.13) for the components describes the physical behavior of the phosphor layer.

Case II: The transfered charge cannot be neglected if the transfered charge is high compared to initial charge ($Q_I \leq Q_{I0}$). With (5.5), the transfered charge can be expressed as function of V_s :

$$Q_I(t) = C_p V_s \; ; \; V_s = d_p(F_{ip} - F_p) \tag{5.15}$$

where V_S is the voltage drop over the interface charge layer, F_p is the field in the phosphor layer and F_{ip} is field in the phosphor layer at the insulator-phosphor interface. Using this equation to eliminate Q_I in the differential equation (5.8) for transfered charge, one gets

$$C_p \frac{d}{dt} V_s = (Q_{I0} - C_p V_s)\,\mathrm{T}\left[\frac{1}{d_p}(V_{ip} - V_s)\right] \tag{5.16}$$

and with $G(V)$ as defined in (5.13)

$$\frac{dV_s}{dt} = \frac{Q_{I0} - C_p V_s}{Q_{I0} C_p} G\left(V_{ip} - V_s\right), \tag{5.17}$$

which are differential equations describing the voltage drop across the interface charge layer, V_{ip} represents the driving voltage across the phosphor layer. To match the equivalent RC-circuit with the above equation, a function for the RC components needs to be found. If the capacitor C_S is nonlinear, the stored charge as function of voltage is expressed as

$$\frac{d}{dt}Q_C(V_C) = \frac{dQ_C}{dV_C}\frac{dV_C}{dt} = C_S(V_C)\frac{dV_C}{dt} \tag{5.18}$$

where C_S is called the differential capacitance with $C_S(V_C) = \frac{dQ_C}{dV_C}$. With this expression and with $V_R = V_{RC} - V_C$, the equation for the equivalent RC-circuit (5.9) leads to

$$\frac{d}{dt}Q_C(t) = C_S(V_C)\frac{dV_C}{dt} = G(V_{RC} - V_C) \tag{5.19}$$

and finally

$$\frac{dV_C}{dt} = \frac{1}{C_S(V_C)}G(V_{RC} - V_C) \tag{5.20}$$

which is a differential equation describing the voltage across the nonlinear capacitor depending on the driving voltage V_{RC}. Comparing this equation with the physical equation for the voltage across the interface charge layer (5.17) leads directly to an expression for the nonlinear capacitor

$$C_S(V_C) := \frac{Q_{I0}C_p}{Q_{I0} - kC_pV_C} = \frac{C_p}{1 - kC_pV_C/Q_{I0}} \tag{5.21}$$

and for the nonlinear resistor G as defined in (5.13), so that both equations become equivalent and one can identify the voltages in the models as $V_s \equiv V_C$ and $V_{RC} \equiv V_{ip}$. The factor k is a fitting factor, which however has been found to be $k = -1$ for a best fit. That makes sense, as the capacity decreases while the capacitor is charged up with increasing V_C, so that the stored charges on capacitor approaches a maximum value Q_{I0} similarly to properties of the interface charge layer.

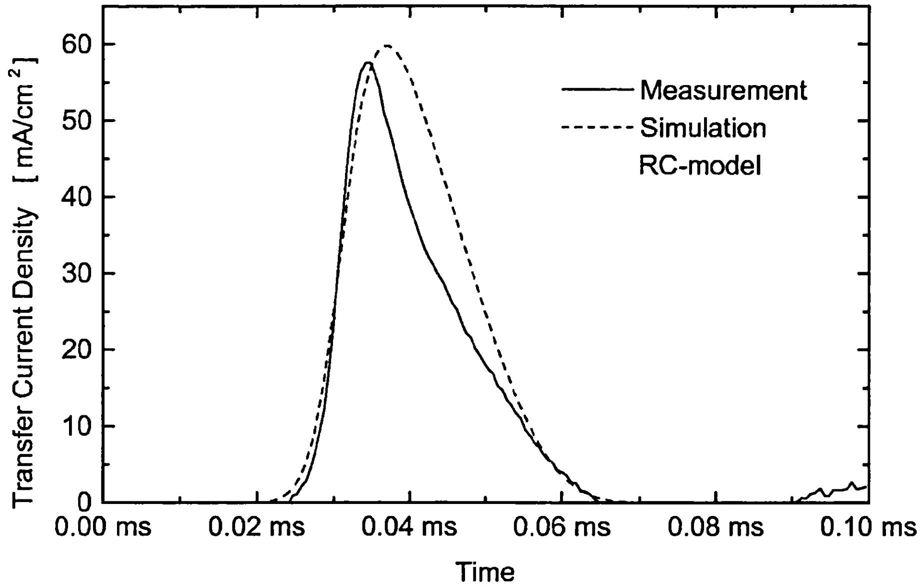

Figure 5.4: RC-model of a TFEL with single interface state: comparison between experimental and simulated transfer current as function of time, sine wave stimulus $V_d = 270$ V and $f_d = 5$ kHz in steady state regime, non annealed device (jr2b), $E_I = 1.16$ eV, $n_0 = 4 \cdot 10^{12}$ cm^{-2} (estimated)

5.2.3 Comparison RC-Model with Measurement

The transfer current as function of time ($I_t - t$-characteristics) are simulated in steady state regime and compared with measured data in Figure 5.4. The complete equivalent RC-circuit of a TFEL with single interface state is shown Figure 5.5, where

$$C_S(V_C) := \frac{C_p}{1 + C_p \left|V_C\right| / Q_{I0}} \tag{5.22}$$

$$G(V) := sign(V) Q_{I0} \mathrm{T}\left[\left|V\right| / d_p\right] . \tag{5.23}$$

The components G and C_s are modified so that both voltage direction can be simulated with these components. This makes it possible to simulate many cycles until a steady state regime is reached. The circuit simulation is done with the SmartSpice simulator of the Silvaco simulation package [42]. The spice program

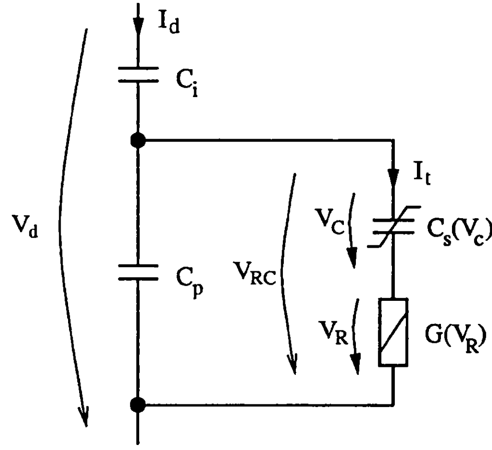

Figure 5.5: Circuit diagram of TFEL model with single interface state

listing is in appendix F. As shown in the diagram, the transfer current obtained with the equivalent RC-circuit is in good agreement with the measured characteristic. The interface electron density $n_0 = 4 \cdot 10^{12}$ cm^{-2} and the interface level $E_I = 1.16$ eV has been obtained by trial and is in accordance to the values used in the previous chapter. The deviation in the curves might be caused by an error of the insulator and phosphor layer capacities. Thus, a better fit of the curves could be obtained if the layer capacities are directly measured for the device to model.

5.3 RC-Model for TFELs with Distributed Interface States

5.3.1 TFEL with Distributed Interface States

The assumption of a discrete interface state at a specific energy level, which has led to a simply equivalent RC-model, might be inaccurate since the interface states maybe continously distributed throughout the band gap of the phosphor material. Thus, the RC-model shall be refined for distributed interface states, in that the

interface electron distribution is approximated as a step function. Equations of section 5.2 needs to be rewritten for the case of discrete energy levels. As explained in section 3.4.3 of the previous chapter, the injection current as function of field and interface charge distribution is

$$I_t(t) = \sum_{n=1}^{m} I_{t.n}(t) \tag{5.24}$$

$$= \sum_{n=1}^{m} \left(Q_{I0.n} - Q_{I.n}(t)\right) \mathbf{T}_n \left[F_p(t)\right] \tag{5.25}$$

where symbols are defined as in chapter 3. Under the condition $Q_{I.n} \ll Q_{I0.n}$, which means that the change of the interface electron density can be neglected, this equation simplifies to

$$I_t(t) = \sum_{n=1}^{m} Q_{I0.n} \mathbf{T}_n \left[F_p(t)\right] \quad . \tag{5.26}$$

The transfer current is also given by equation (3.50):

$$I_t(t) = \frac{d}{dt} Q_I(t) = \frac{d}{dt} \sum_{n=1}^{m} Q_{I.n}(t) \tag{5.27}$$

Equating (5.26) and (5.27), one has with (5.15)

$$C_p \left(\frac{d}{dt} V_{ip}(t) - \frac{d}{dt} V_p(t) \right) = \sum_{n=1}^{m} Q_{I0.n} \mathbf{T}_n \left[F_p(t)\right] \tag{5.28}$$

and finally

$$\frac{d}{dt} V_p + \frac{1}{C_p} \sum_{n=1}^{m} Q_{I0.n} \mathbf{T}_n \left[V_p / d_p\right] = \frac{d}{dt} V_{ip}, \tag{5.29}$$

which is a first order nonlinear differential equation for the voltage V_p across the phosphor layer (excluding the interface charge layer). This differential equation is valid as long as the transfered interface charge $Q_{I.n}$ is small compared to the initial interface charge $Q_{I0.n}$ for each energy level.

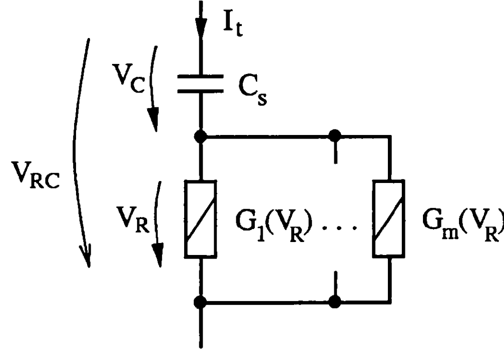

Figure 5.6: Equivalent RC-circuit for phosphor layer with distributed interface electron density

Case II: Under the condition that the transfered charge of one or more energy levels cannot be neglected, or in other words $Q_{I.n} \leq Q_{I0.n}$, a differential equation equal to the equation above can be derived on the same way:

$$\frac{d}{dt}V_p + \frac{1}{C_p}\sum_{n=1}^{m}(Q_{I0.n} - Q_{I.n}(t))\mathbf{T}_n\left[V_p/d_p\right] = \frac{d}{dt}V_{ip}, \tag{5.30}$$

5.3.2 RC-Model for TFEL with Distributed Interface States

Assuming for the beginning, that the physical model with multiple discrete interface states as developed in the previous section can be represented with a RC-circuit as shown in Fig 5.6. The capacitor C_s models the limitation of the transfer process due to compensation of the electrical field by transfered charges. The tunneling characteristic of the different energy levels are modeled by m parallel nonlinear resistors. The current equations for the equivalent circuit are

$$I = \sum_n I_n = \sum_n G_n(V_R) \tag{5.31}$$

and

$$I = C_S \frac{d}{dt} V_C \quad . \tag{5.32}$$

Combining these two equations and replacing the voltage V_C with $V_C = V_{RC} - V_R$, one obtains

$$\sum_n G_n(V_R) = C_S \frac{d}{dt} V_R = C_S \left(\frac{dV_{RC}}{dt} - \frac{dV_R}{dt} \right) \tag{5.33}$$

and rewriting, one finally gets a differential equation for equivalent RC-circuit

$$\frac{dV_R}{dt} + \frac{1}{C_S} \sum_n G_n(V_R) = \frac{dV_{RC}}{dt} \quad . \tag{5.34}$$

If this equations is compared with physical equation (5.29) one can identify the capacitor as capacity of the phosphor layer

$$C_S \equiv C_p \tag{5.35}$$

and the nonlinear resistors as the product of tunneling function and initial interface charge for each discrete energy level:

$$G_n(V) \equiv Q_{I0.n} \mathrm{T}_n \left[V/d_p \right] \quad . \tag{5.36}$$

The nonlinear resistor is given as function of the interface electron density and energy level.

5.3.3 Comparison with Measurement

The complete RC-model of a TFEL with distributed interface states is obtained when the current source in the circuit in Figure 5.1 is replaced with circuit in Figure 5.6 analogous to Figure 5.5 . For the demonstration of the RC-model, the

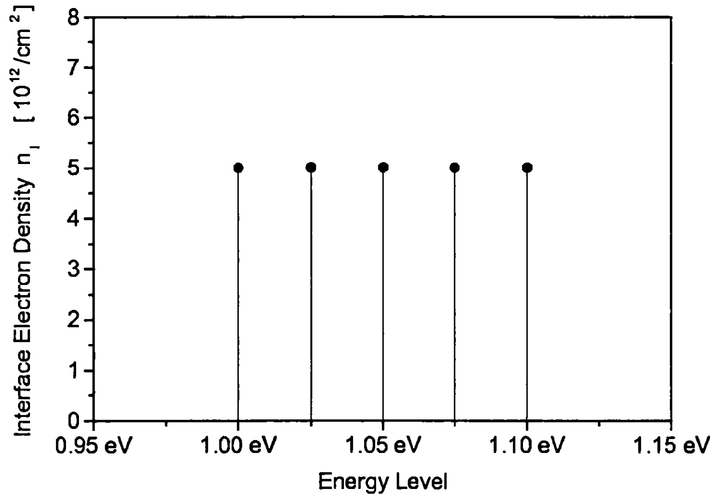

Figure 5.7: Interface electron distribution used for RC-model with distributed interface states

interface distribution is assumed to be a constant function as shown in Figure 5.7. If an exact simulation of a real device is to be made, the interface electron distribution needs to be measured. The transfer current as a function of time ($I_t - t$-characteristics) are simulated for steady state regime and compared with measured data in Figure 5.8. The components G_n are modified so that both voltage directions can be simulated:

$$G_n(V) := sign(V) Q_{I0.n} \mathbf{T} \left[|V| / d_p \right] . \tag{5.37}$$

The steady state regime is obtained by simulating many driving cycles. As can be seen in the diagram, the transfer current obtained with the equivalent RC-circuit is in satisfying agreement with the measured characteristic. A better fit of the curves could be obtained if the correct interface electron distribution can be measured.

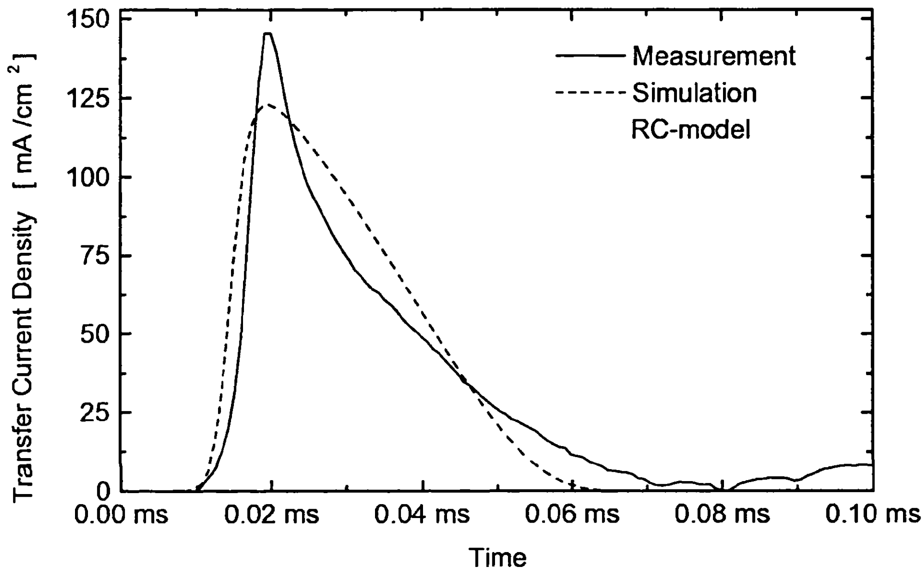

Figure 5.8: RC-model of a TFEL with distributed interface states for thermally annealed devices: comparison between measured and simulated transfer current as function of time, sine wave stimulus V_d = 270 V and f_d = 5 kHz, steady state regime, thermal annealed device (jr2a), interface electron density used for RC-model in Figure 5.7

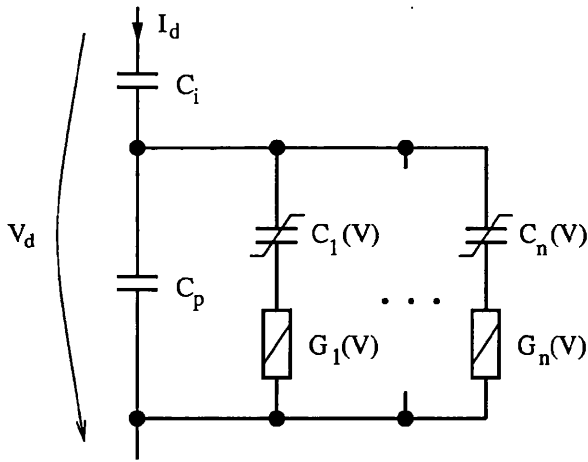

Figure 5.9: Proposed RC-model of a TFEL with low density interface electron distribution

5.4 Conclusion

The presented equivalent RC-models are shown to be a realistic electrical model of TFELs. They are in a good agreement with measured characteristics, especially for non annealed devices, and therefore sufficient for embedded simulation of driver electronics and TFELs together. The exact measurement of the insulator and phosphor layer capacities and the estimation of the interface electron distribution are essential. Although the models are validated by comparing the simulation with the measurement for one driving voltage and frequency, they need to be proved for a wider frequency and voltage range. By doing that, the estimated interface electron distribution should be kept independent of driving frequency and voltage. This validation is recommended for future work.

The RC-model of TFELs with distributed interface states is developed for the case that the transfered charge is small compared to the initial interface charge of each energy level. If this restriction is dropped, an equivalent RC-model with distributed interface charge could be deduced from the existing models as shown in Figure 5.9. So far, this RC-model could not be proved on a theoretical basis.

Chapter 6

Optical Characteristics of LETFELs

6.1 Introduction

The aim of this chapter is to investigate the optical characteristics of a LETFEL pixel. The LETFEL pixel can be considered as a two-dimensional planar optical structure. In fact, the phosphor layer (ZnS) and the insulator layers (Y_2O_3) along with the metalisation layers form a step-index waveguide with distributed light sources (active waveguide). Principally, the analysis of the optical characteristics of the pixel structure can be done by solving Maxwell's wave equations or by ray tracing (ray optics). Since the light generating layer can be considered as an ensemble of homogeneously distributed and isotropic light sources, a simulation must be performed for each point and each direction. The analysis of the entire pixel structure cannot be done by rigorously solving Maxwell's wave equation, since the pixel structure is too large and such an analysis would require excessive computing resources. Likewise, the analysis can not be done completely with ray tracing, as the film thickness is in the range of the wave length and thus, it can only be analysed by solving the wave equations. Therefore, the investigation,

either by experiment or by analysis, is to be done separately for each part of the optical structure. These parts are the planar waveguide, the two-dimensional geometrical shape of the pixel and the outcoupling process (facets). It has been attempted in [16] and [15] to solve the problem of an active waveguide by using a cladded waveguide without internal light sources. The outcoupling process of the waveguide is investigated in [15]. This chapter focus on the two-dimensional pixel structure.

A simplified one-dimensional active optical structure is analysed in section 6.2. Subsequently, a novel two-dimensional optical model for different shaped pixel structures is developed in section 6.4.

6.2 Attenuation in a Luminescent Waveguide

It is instructive to start with an one-dimensional optical structure. The attenuation coefficient α of an optical media characterises the relative intensity loss for an infinitesimal length dx and is defined as [44]

$$\alpha = -\frac{1}{I}\frac{dI}{dx} \tag{6.1}$$

where I is the intensity of the incoming light. In our case, the attenuation coefficient α is the attenuation coefficient of the waveguide (passive waveguide), which can be measured or estimated by analysing the waveguide. Solving the above differential equation (separation of the variable) leads to the intensity I_p at $x = 0$ for a passive waveguide:

$$I_p = I_0 e^{-\alpha x} \tag{6.2}$$

where I_0 is the initial intensity of the light at the position x. Measured data are in good agreement with equation (6.2), see Figure 6.2.

If the waveguide contains homogeneously distributed light sources (active guide), as it is the case in a LETFEL, the waveguide can be calculated in that the waveguide is separated in infinitesimal thin slabs of the thickness dx. Each slab at the distance x and thickness dx generates light of the intensity

$$dI_a = i_g A dx \tag{6.3}$$

where i_g is the intensity generation density as defined in equation 6.11, A is the cross section area of the waveguide and the slab thickness is dx. Emitted light of such a slab is attenuated with $e^{-\alpha x}$ when it travels to interface at $x = 0$. The light contributions of all slabs from $x = 0$ to $x = l$ are integrated in order to obtain the

total light at $x = 0$:

$$I_a(l) = \int_0^l Ai_g e^{-\alpha x} dx = A\frac{i_g}{\alpha}(1 - e^{-\alpha l}) \quad (6.4)$$

where l is length and A is the cross section area of the waveguide. The generated light increases linearly for short active waveguides and reaches a 'saturation' value for long active waveguides. This limitation effect can be explained as, with an increase of l, the total amount of generated light increase linearly, whereas the attenuation of the light increases exponentially. As a matter of fact, the limitation effect has been observed experimentally, see Figure 6.3, as well as in [17] and [16]. The maximal attainable intensity for an infinite long active waveguide is

$$I_{max} = \lim_{l \to \infty} I_a(l) = A\frac{i_g}{\alpha} \sim \frac{1}{\alpha} \ . \quad (6.5)$$

The outcoupled light of a sufficient long active waveguide is proportional to the reciprocal of attenuation coefficient α. For short active waveguides, the attenuation has a minor effect and the intensity of the active waveguide can be approximated by the first order Taylor expansion at $l = 0$:

$$I_a(l) \approx Ai_g l \ \sim l \quad (6.6)$$

The outcoupled light of a short active waveguide is proportional to the generation density i_g. Knowing that, short active waveguides can be utilized as a reference structure for measuring the generated light ($\sim i_g$) independently of the actual attenuation.

The characteristic of the active waveguide can also be described by the differential equation

$$\frac{dI_a}{dl} = i_g A - \alpha I_a \ . \quad (6.7)$$

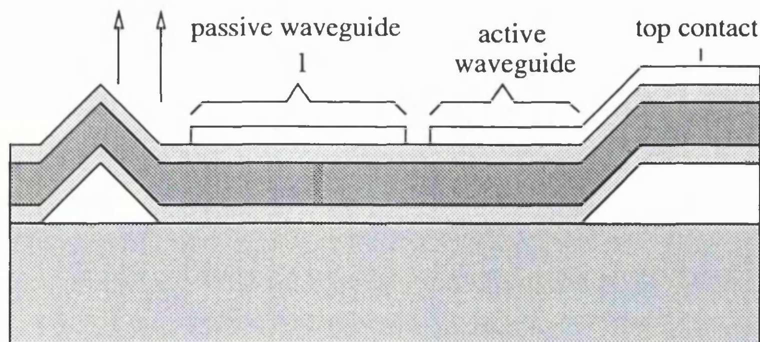

Figure 6.1: Passive waveguide structure for measuring the attenuation

The solution, which satisfy this differential equation, is equation (6.4) for the active waveguide . The left term on the right side of equation (6.7) represent the generated light for a slab of the thickness dl, which is equal to (6.3). The right term indicates the loss of light due to attenuation as in a passive waveguide, equal to equation (6.1).

6.3 Optical Characterisation

6.3.1 Attenuation in a Passive Waveguide

A special LETFEL devices are employed for measuring the attenuation of the passive waveguide. The passive waveguide structure of this kind of displays is formed by a complete TFEL-stack with top electrode whereby the top electrode is not connected as shown in Figure 6.1. This configuration of a passive waveguide ensures that the same conditions as in the active waveguide structure are present provided that the material properties are independent of electric and electromagnetic field. The attenuation in the passive waveguide is estimated by measuring the intensity of the outcoupled light for a set of passive waveguides with various lengths l. Each passive waveguide is illuminated by a constant light source, which is realised with an active TFEL-area of constant length.

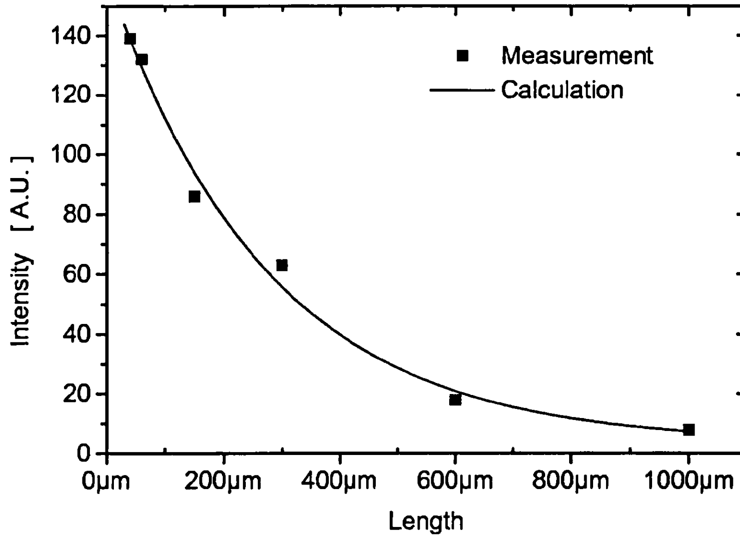

Figure 6.2: Passive Waveguide: intensity I_p versus length l of the waveguide, sample jr1 (Tab. B.4)

The measured intensity upon the waveguide length and a curve fit of equation (6.2) are shown in Figure 6.2. The attenuation coefficient obtained by the curve fit is $\alpha = 3700\ \mathrm{m}^{-1}$.

6.3.2 Attenuation in a Active Waveguide

The attenuation of an active waveguide has been measured with a set of planar active waveguides with different lengths l. The measured intensity of the outcoupled light and the curve fit of function 6.4 are shown in Figure 6.3. The attenuation coefficient obtained by the curve fit is $\alpha = 9200\ \mathrm{m}^{-1}$.

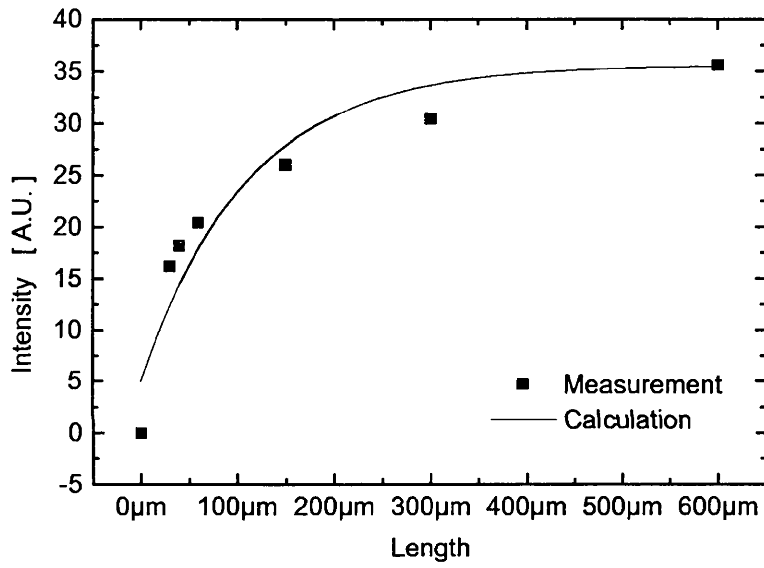

Figure 6.3: Active Waveguide: intensity versus length of the waveguide, sample jr1 (Tab. B.4),

6.4 Simple optical model of electroluminescent pixel structures

6.4.1 Introduction

A simple analytical model of the optical behavior is developed for 2 dimensional laterally emitting pixel structures. The model is applied to circular, square and hexagonal LETFEL pixels (Figure 1.3), which represent 2-dimensional laterally emitting pixel structures and which are the most common geometrical shapes used in dot matrix displays. The outcoupled light of a such pixel can be obtained with the model, and consequently, one can identify the best geometrical shape of a pixel and the optimal pixel dimension. For obtaining the latter, it must be considered that the larger the pixel dimension the more light is produced and the more attenuation in the phosphor film occurs. Consequently, no significant increase of outcoupled light appears beyond a certain pixel size; a limiting effect occurs and hence the ratio of the emitted light flux to the total pixel area decreases. The limiting effect has been experimentally observed for a length of the waveguide greater than 300 μm [17]. On the other hand, if the pixel diameter is chosen too small, more chip area is used for the micro-mirrors. Thus, the ratio of active (phosphor) to passive (mirrors) area lessens and the ratio of the emitted light flux to total pixel area decreases. As a consequence, an optimum pixel size exists for a given mirror width and attenuation coefficient.

A further problem, which can be investigated with the model, is caused by total internal reflection at the interface between the phosphor layer and the surrounding passivation layer (SiON). Light, that is generated within the phosphor and reaches the phosphor-passivation-interface with an angle greater than the angle of total internal reflection, is reflected back into the pixel and attenuated again. The angle

of total reflection is about 43 degrees (referred to the interface normal) for the ZnS-SiON interface. Different pixel geometries such as a circle, a square and a hexagon could thus influence the angular distribution of the incident light and consequently affect the optical efficiency of the pixel.

The developed model is based on a ray optics approximation where the absorption of the light within the light generating medium (phosphor material), the transmission behaviour of the phosphor-air interface and the micro-mirror width is taken into account. Light that is reflected back into the pixel due to total internal reflection is neglected. This simplification of the problem is a good approximation for materials with a high attenuation coefficient, because the back reflected light is attenuated. The effect of this neglect is investigated for square pixels by taking into account the first reflection. Different transmission coefficients depending on polarization and incident angle are not taken into account for the examples under investigation although they can be readily introduced.

A general optical model for a three-dimensional light emitting structure is developed in subsection 6.4.2. The equivalent two-dimensional model for laterally emitting thin film structures is developed in subsection 6.4.3. This model is subsequently applied to circular, square and hexagonal structures in subsection 6.4.4. The results are discussed in subsection 6.4.5.

6.4.2 Model for Three-Dimensional Structures

To begin with, the fundamental relation of a normal light source are recalled here. The total light flux (luminous power) Φ of a light source is calculated as:

$$\Phi = \int I d\Omega \tag{6.8}$$

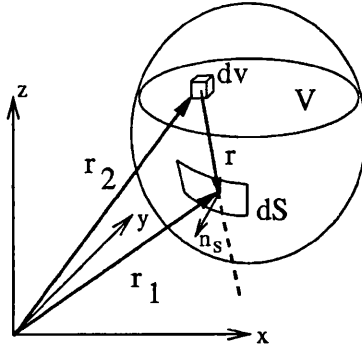

Figure 6.4: Definition of the geometry of a three-dimensional light emitting structure

where I is the luminous intensity, Ω is the solid angle and $d\Omega = \frac{\cos\vartheta}{r^2}dS$ (see [45]), dS is the illuminated infinitesimal area element on the surface of a sphere around the light source, r is the distance between the light source and the area elements dS, see Figure 6.4. The angle between the light ray and the surface normal vector $\mathbf{n}_S$ is ϑ. The light flux of an isotropically luminescent light source ($I(\Omega) = const.$) is $\Phi = 4\pi I$. The illuminance on an area element dS at a distance r from the light source is defined as [45]:

$$E = \frac{d\Phi}{dS} = I\frac{\cos\vartheta}{r^2} \tag{6.9}$$

For a homogeneously distributed isotropic light source, like a phosphor layer, it is necessary to define a light generation density g and an intensity density i_g for an infinitesimal volume dV:

$$g := \lim_{\Delta V \to 0} \frac{\Delta\Phi}{\Delta V} = \frac{d\Phi}{dV} \tag{6.10}$$

$$i_g := \lim_{\Delta V \to 0} \frac{\Delta I}{\Delta V} = \frac{dI}{dV} \tag{6.11}$$

Φ and I denote the light flux and the luminous intensity respectively generated in the volume element dV. The units of g and i_g are $\frac{lm}{m^3}$ and $\frac{cd}{m^3} = \frac{lm}{sr \cdot m^3}$ respectively. The intensity density for isotropically luminescent infinitesimal light sources is

then $i_g = \frac{1}{4\pi}g$. To obtain the illuminance E on an area element dS with position vector $\mathbf{r}_1$ on the surface of the light generating medium, the intensity density i of all points in the light emitting volume V (pixel volume) must be integrated taking into account the attenuation in the medium, see Figure 6.4:

$$E = \int_V a(r)\, i_g \frac{\cos\vartheta}{r^2}\, dV \tag{6.12}$$

where r is the distance between the light source and the area element on the surface $r = |\mathbf{r}_1 - \mathbf{r}_2|$, ϑ is incident angle $\vartheta = \angle(\mathbf{r}_1 - \mathbf{r}_2, \mathbf{n}_A)$, $dV = dx\, dy\, dz$, $\mathbf{r}_2 := (x, y, z) \in V$. The attenuation function is $a(r) = e^{-\alpha r}$ where α is the attenuation coefficient of the intensity. The total outcoupled light flux Φ is obtained by integrating the illuminance over the surface S of the light emitting structure where the transmission function $T(\vartheta)$ of the surface is taken into account:

$$\Phi = \oint_{A_S} \int_V T(\vartheta) a(r) \frac{g}{4\pi r^2} \cos\vartheta\, dV\, dA \tag{6.13}$$

where r_1 is the vector along the surface $\mathbf{r}_1 = (x(u,w), y(u,w), z(u,w)) = \mathbf{r}_1(u,w) \in A_S$, $dA = |\mathbf{r}_{1u} \times \mathbf{r}_{1w}|\, du\, dw$, $\mathbf{r}_{1u} = \frac{\partial \mathbf{r}_1}{\partial u}$ and $\mathbf{r}_{1w} = \frac{\partial \mathbf{r}_1}{\partial w}$. The parameters u and w are the curvilinear coordinates. Light, that is reflected back into the pixel due to total internal reflection, is neglected.

6.4.3 Model for Two-Dimensional Structures

Similar formulae to section 2 can be developed for a two-dimensional, thin layered laterally emitting structure (see Fig. 6.5). The real pixel is, of course, a three-dimensional structure but it can be approximated as a two-dimensional structure if the layer thickness is small compared to the pixel dimension. This is true for LETFEL devices where thin-films are less than $1\mu m$ thick and the pixel size ex-

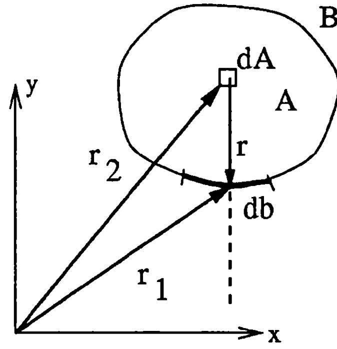

Figure 6.5: Definition of the geometry of a two-dimensional light emitting structure

ceeds $10\mu m$ square. The layers form a planar waveguide. Emitted light propagates therefore only in two dimensions along the planar waveguide. The attenuation coefficient α is, in this case, the attenuation coefficient of the waveguide, which can be experimentally obtained.

For a calculation of a two-dimensional structure, the following definitions need to be introduced (where the prime indicates a two-dimensional parameter):

$$I' := \frac{d\Phi}{d\omega} \tag{6.14}$$

$$E' := \frac{d\Phi}{db} = I'\frac{\cos\vartheta}{r} \tag{6.15}$$

where ω is the angle with $d\omega = \frac{\cos\vartheta}{r}db$, b is the border line length, r denotes the distance between the light emitting area element dA and the boundary element db. The incident angle ϑ is defined as the angle between the light ray and the boundary normal vector. The two-dimensional luminous intensity I' defines the portion of radiated light flux $d\Phi$ per infinitesimal unit of angle. The two-dimensional illuminance E' defines the portion of light flux $d\Phi$ per length db falling on an infinitesimal part db of the pixel boundary.

Furthermore, the two-dimensional luminous intensity density i' and the two-

dimensional light generation density are defined as:

$$g' := \frac{d\Phi}{dA} \tag{6.16}$$

$$i' := \frac{dI'}{dA} = \frac{1}{2\pi}\frac{d\Phi}{dA} \tag{6.17}$$

where A is the active (light emitting) pixel area. The units of the two-dimensional luminous intensity density i' and the two-dimensional light generation density g' are $\frac{lm}{rad \cdot m^2}$ and $\frac{lm}{m^2}$ respectively. The two-dimensional light generation density g' represents the generated light flux Φ per infinitesimal area element dA. The two-dimensional luminous intensity density defines the luminous intensity for an area element dA.

A single area element emits light, which is traveling towards the pixel boundary and results in an illumination of the pixel boundary. The illuminance (of a point on the boundary) per area element dA, e', is calculated from equations (6.15) and (6.17) as follows:

$$e' = \frac{dE'}{dA} = a(r) i' \frac{\cos\vartheta}{r} \tag{6.18}$$

under consideration of the attenuation $a(r)$. The illuminance E' of a point at the pixel boundary is then given by the area integral over the entire pixel area A:

$$E' = \int_A a(r)\, i' \,\frac{\cos\vartheta}{r}\, dA = \int_A a(r)\, \frac{g'}{2\pi r} \cos\vartheta \, dA \tag{6.19}$$

To obtain the total emitted light flux of the pixel, the total illuminance E' along the boundary line B must be integrated, by taking also into account the transmission function $T(\vartheta)$ for the phosphor-passivation interface:

$$\Phi = \oint_B \int_A T(\vartheta)\, a(r)\, \frac{g'}{2\pi r} \cos\vartheta \, dA \, db \tag{6.20}$$

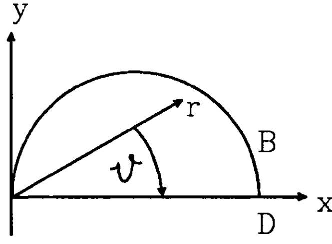

Figure 6.6: Circular Pixel Structure (top view) as used in the calculation

where ϑ is the incident angle, $\mathbf{B}(t)$ is the boundary line of the pixel and $db = |\frac{d}{dt}\mathbf{B}(t)|dt$; t is the transformation parameter. Equation (6.20) can be solved more easily when the area integral is written in polar coordinates with the origin on the boundary ($\mathbf{r}_1 = 0$):

$$\Phi = \oint_B \int_{-\vartheta_t}^{\vartheta_t} \int_0^{R_B} a(r_2) \frac{g'}{2\pi} \cos\vartheta \, dr_2 \, d\vartheta \, db \qquad (6.21)$$

where $\mathbf{r}_2 = (r_2 \cos\vartheta, r_2 \sin\vartheta)$, $R_B = R_B(\vartheta)$ is the distance from the origin to the boundary B and ϑ_t is the angle for total internal reflection. The transmission function is simplified so that $T = 1$ for $\vartheta < \vartheta_t$ and $T = 0$ for $\vartheta \geq \vartheta_t$ (total internal reflection occurs). This means the integration of ϑ is carried out with $T = 1$ in the interval $-\vartheta_t$ to ϑ_t .

6.4.4 Model for Circle, Square and Hexagon Structures

The general solution for a two-dimensional structure is now applied to circular, square and hexagonal pixels as these are the important structures for dot matrix displays. The light flux Φ_c of a circular pixel is solved using equation (6.21). The boundary radius R_B, which is the distance from the origin to the pixel boundary, is given by $R_B = D\cos\vartheta$ (upper integration limit), where D is the pixel diameter of the active area (Figures 1.3 and 6.6). The active area of a circular structure is

$A = \pi D^2/4$. The closed line integral for the pixel boundary is $D\pi$, because the illuminance is identical for each point at the boundary line owing to the symmetry of the circle. The integration with respect to the angle ϑ is carried out between 0 and the angle of total reflection ϑ_t. Thus, the integral must be multiplied by two for the full range $-\vartheta_t \leq \vartheta \leq \vartheta_t$. The attenuation function is $a(r) = \exp(-\alpha r)$ with the attenuation coefficient α in $1/m$. Hence,

$$\begin{aligned} \Phi_c &= 2\pi D \int_0^{\vartheta_t} \int_0^{D\cos\vartheta} \frac{g'}{2\pi} \exp(-\alpha r) \cos\vartheta \, dr d\vartheta \\ &= g' \frac{1}{\alpha} D \int_0^{\vartheta_t} \{1 - \exp(-\alpha D \cos\vartheta)\} \cos\vartheta \, d\vartheta \end{aligned} \qquad (6.22)$$

where the pixel diameter D denotes the diameter of the circle. The integral of equation (6.22) can only be solved numerically.

The light flux Φ_s of the square pixel is obtained by solving equation (6.21) for one side only because of the symmetry. The integration area is to be partitioned into two separate integration areas. The inner area integral can be solved analytically, whereas the integral w.r.t. the angle can only be solved numerically. The integration w.r.t. ϑ is carried out between 0 and the angle of total internal reflection ϑ_t. The result Eq. (6.23) is valid for $0 \leq \vartheta_t \leq \pi/4$ (note $\vartheta_t \approx 43^o$ for our LETFEL pixels):

$$\begin{aligned} \Phi_s &= \frac{4}{\pi\alpha} g' \{D \sin\vartheta_t - \frac{\sin^2\vartheta_t}{2\alpha} + \\ &\int_0^{\vartheta_t} (D\sin\vartheta - D\cos\vartheta + \frac{\sin 2\vartheta}{2\alpha}) \exp(-\alpha \frac{D}{\cos\vartheta}) \, d\vartheta\} \end{aligned} \qquad (6.23)$$

where the pixel diameter D denotes the length along a side of the square. The active area of the square is $A = D^2$.

The light flux Φ_h of a hexagonal structure is calculated by solving equation (6.21) for one side of the hexagon only. The integration area is partitioned into four different integration areas. Only the inner integral of the radius can be solved analytically. The integrals along the border line and over the angle ϑ must be

solved numerically. Equation (6.24) is valid for $\frac{1}{6}\pi \leq \vartheta_t \leq \frac{1}{3}\pi$:

$$\begin{aligned}
\Phi_h = & \tfrac{6}{\pi\alpha} g' \{ \rho \sin\vartheta_t \\
& - \int_0^\rho \int_0^{\alpha_1} \exp(-\alpha \tfrac{\sqrt{3}\rho}{\cos\vartheta}) \cos\vartheta \, d\vartheta \, dy \\
& - \int_{y_g}^\rho \int_{\alpha_1}^{\vartheta_t} \exp(-\alpha \tfrac{y+\rho}{\sin(\vartheta+\pi/6)} \tfrac{\sqrt{3}}{2}) \cos\vartheta \, d\vartheta \, dy \\
& - \int_0^{y_g} [\int_{\alpha_1}^{\alpha_2} \exp(-\alpha \tfrac{y+\rho}{\sin(\vartheta+\pi/6)} \tfrac{\sqrt{3}}{2}) \cos\vartheta \, d\vartheta \\
& + \int_{\alpha_2}^{\vartheta_t} \exp(-\alpha \tfrac{y}{\sin(\vartheta-\pi/6)} \tfrac{\sqrt{3}}{2}) \cos\vartheta \, d\vartheta] \, dy \}
\end{aligned} \tag{6.24}$$

where y is the ordinate (Fig. 6.5) and the integration limits are as follows:

$$\begin{aligned}
y_g &= \tfrac{1}{2}\rho(\sqrt{3}\tan\vartheta_t - 1) \\
\alpha_1 &= \arctan \tfrac{y}{\sqrt{3}\rho} \\
\alpha_2 &= \arctan(\tfrac{2}{3}\sqrt{3}\tfrac{y}{\rho} + \tfrac{\sqrt{3}}{3})
\end{aligned} \tag{6.25}$$

where ρ denotes the distance between the center point and a corner point of the hexagon. This ρ is the radius of the outer circle of the hexagon. The equivalent pixel diameter D is the distance from side to side (inner circle of the hexagon) with $D = \rho\sqrt{3}$. The active area of a hexagonal pixel is $A = 3\rho^2\sqrt{3}/2$. It is again noted that for simplicity the above formulae for the outcoupled light ignore any internally reflected rays and are therefore valid for pixels with phosphor materials that posses a sufficiently high attenuation.

6.4.5 Results and Discussion

The outcoupled light of hexagonal, square and circular pixels is calculated by the numerical solution described in Section 6.4.4 using the program MATHCAD. In all the calculations below, the mirror width w is 2 μm, the angle of total internal reflection ϑ_t is 43 degrees and the attenuation coefficient α is $12000/m$. The light flux generation density g' is set to $1\, lm/m^2$.

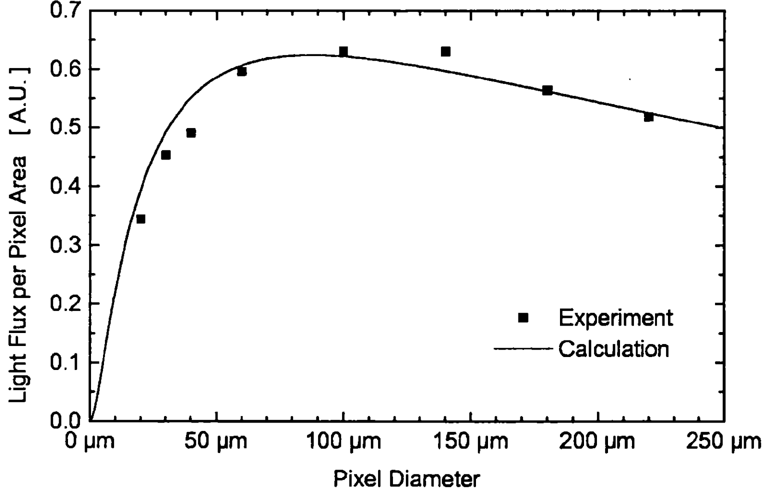

Figure 6.7: Comparison Optical Model with Measurement, square pixel, facets un-etched, simulation with attenuation coefficient $\alpha = 6000$ m^{-1} and angle of total reflection $\vartheta_t = 90°$, $w = 5.5$ μm

A comparison between measurement of a LETFEL display with square pixels and the model (equation 6.27) is shown in Figure 6.7. Since the facets are not etched for the LETFEL display under investigation, the angle of total reflection is assumed to be $\vartheta_t = 90°$, i.e. no total reflection occurs. As can be seen, the simulation is in a good agreement with the measurement.

Figure 6.8 illustrates how the ratio of light flux to the total pixel area Φ/A_t varies with the pixel diameter D for the hexagonal structure (Φ_h/A_{th}), the square structure (Φ_s/A_{ts}), the circular structure (active region) placed in a hexagon (Φ_{tc}/A_{th}) and the circular structure placed in a square (Φ_c/A_{ts}). The total pixel area A_t is the sum of active area and passive area (mirrors). For the square structure, the total pixel area is given by $A_{ts} = (D + 2w)^2$ with D denoting the length along a side of the active square. The total pixel area for the hexagonal structure is given by $A_{th} = \frac{3}{2}\sqrt{3}(\frac{D}{\sqrt{3}} + w)^2$, where the diameter D is the distance from one side to the opposite side of the hexagon (diameter of the inner circle of

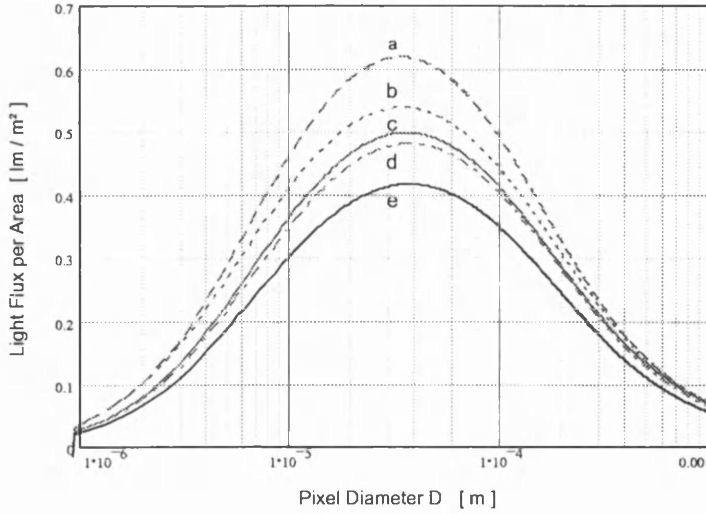

Figure 6.8: Calculated light flux to pixel area ratio as a function of pixel diameter D; (a) square pixel under consideration of the first reflection, under neglect of the first reflection: (b) hexagon pixel, (c) square pixel, (d) circular pixel placed in a hexagon cell, (e) circular pixel placed in a square cell;

Hexagon	54 %	circle in hexagon cell	48 %
square	50 %	circle in square cell	41 %

Table 6.1: Attainable light flux per unit area

the hexagon). For all structures the maximum of light/area ratio occurs at the diameter $D \approx 35\,\mu m$. This corresponds to a display resolution of 725 pixel per inch. The maximum light flux attainable per area is listed in Table 6.1.

The results in Figure 6.8(b-e) were obtained by neglecting the back reflected light. To estimate the error caused by the simplification, a simulation of a square pixel is performed by considering the first reflection (see Fig.6.8a). The equation (6.23) for the square pixel is extended as follows:

$$\begin{aligned}\Phi_{s1} = \Phi_s + \quad & \tfrac{4}{\pi\alpha} g' \int_{\vartheta_t}^{\frac{\pi}{2}} \{ \int_{\min(D, D\tan\vartheta)}^{D} T(\vartheta)(1 - \exp \tfrac{-\alpha y}{\sin\vartheta}) \exp(-\alpha r) dy \\ & + \int_0^{\min(D, D\tan\vartheta)} T(\tfrac{\pi}{2} - \vartheta)(1 - \exp \tfrac{-\alpha D}{\cos\vartheta}) \exp(-\alpha r) dy \} \cos\vartheta d\vartheta \end{aligned} \tag{6.26}$$

where $r = \min(D/\cos\vartheta, (D - y)/\sin\vartheta)$, the transmission function $T = 1$ for $\vartheta < \vartheta_t$ and $T = 0$ for $\vartheta \geq \vartheta_t$. By comparing curves a and c in Fig.6.8 it can be

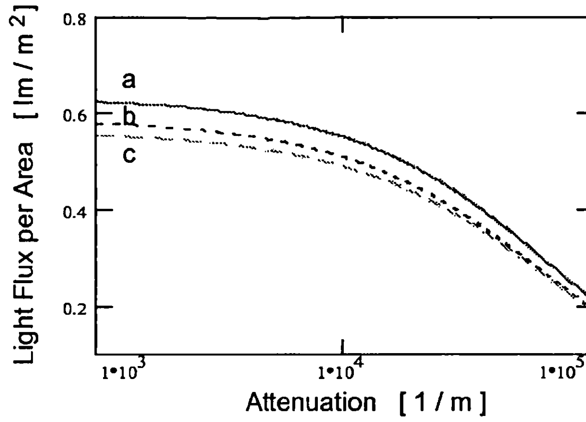

Figure 6.9: Calculated light flux to pixel area ratio as a function of the attenuation coefficient α, (a) hexagon structure, (b) square structure and (c) circle structure placed in hexagon with mirror width $w = 2\mu m$ and pixel diameter $D = 30\mu m$

deduced that the optimal pixel diameter is unchanged and the error due to the neglect of the back-reflected light is approximately 20 percent at the optimal pixel diameter.

In Figure 6.9, the ratio of light flux to pixel area as a function of the attenuation coefficient is shown for three different pixels with a diameter $D = 30\mu m$. The light flux decreases significantly for an attenuation coefficient greater than $10^4/m$. Hence, the luminance of the display can be improved if the attenuation of the waveguide is reduced.

Figure 6.10 shows a plot of the light flux to pixel area ratio as a function of the angle of total internal reflection for a square pixel with different attenuation coefficients. The light flux depends strongly on the angle of total internal reflection for $\vartheta_t \leq 77.5^o$. The intensity of the outcoupled light can thus be improved further with an increasing ϑ_t. This can be achieved, for example, by employing other materials as passivation layers. Note, that for the square pixel, equation (6.23) is

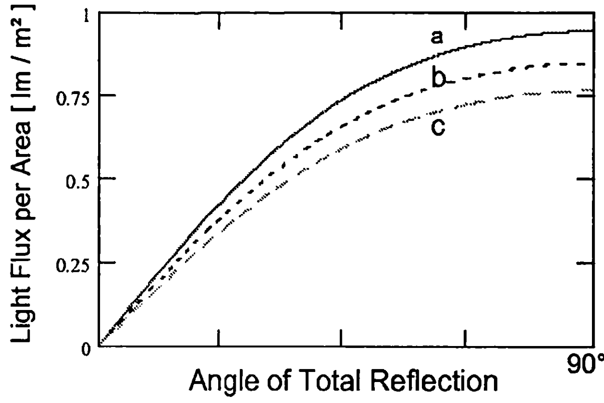

Figure 6.10: Calculated light flux to pixel area ratio as a function of the angle of total internal reflection for a square pixel structure; $0 \leq \vartheta_t \leq \pi/2$; (a) $\alpha = 4000/m$, (b) $\alpha = 12000/m$, (c) $\alpha = 20000/m$; mirror width $w = 2\mu m$, pixel diameter $D = 30\mu m$

not valid for $\vartheta_t > \pi/4$. Thus, the following equation is used instead:

$$\begin{aligned} \Phi_r = \; & \tfrac{4}{\pi\alpha} g' \textstyle\int_0^{\vartheta_t} \{(1 - \exp \tfrac{-\alpha D}{\cos\vartheta})(D - \min(D, D\tan\vartheta)) \\ & + \min(D, D\tan\vartheta) - \tfrac{\sin\vartheta}{\alpha}(1 - \exp \tfrac{-\alpha \min(D, D\tan\vartheta)}{\sin\vartheta})\} \cos\vartheta d\vartheta \end{aligned} \tag{6.27}$$

6.5 Conclusion

A ray optics model for two dimensional pixel structures has been developed. It is useful for the fast estimation of the outcoupled light and for optimisation of the pixel geometry for a given attenuation coefficient. The model is applied to circular, square and hexagonal pixel structures because of their importance in dot matrix displays. For the investigated display type, the optimum pixel diameter is estimated to be about $35\mu m$. The simulation are in good agreement with measured results. However, the validation of the model with experimental results need to be extended and will be objective of future investigations.

Chapter 7

Design and Fabrication of an ASID

7.1 Design of an ASID

In this chapter, a design for an ASID with a fixed legend is proposed where the legend is defined by a single photo mask. The design utilizes a basic device consisting of an array of pixels. Each pixel of the array is insulated with respect to each other, as shown in Figure 7.1 (see also 1.3b for a single pixel). The pixels are connected with a metal layer to form more complex display elements as required. Therefore, the basic device can be produced with a standardised fabrication pro-

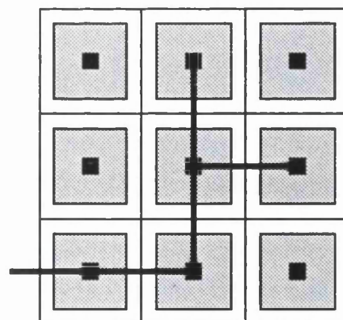

Figure 7.1: Principle of an ASID, top view of an array of TFEL pixels connected with a metalisation layer

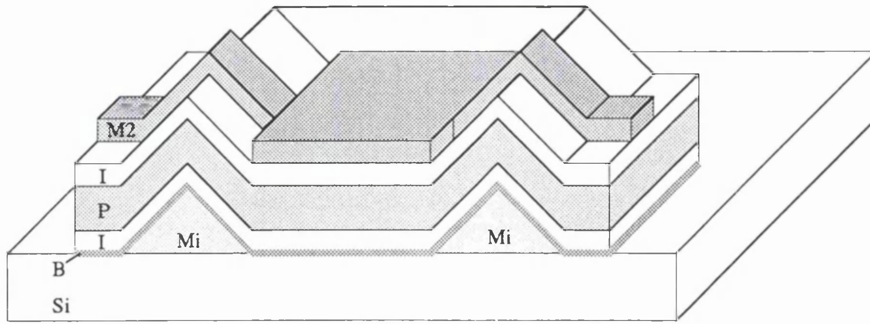

Figure 7.2: Basic LETFEL ASID, without passivation layer; M2 - metal, I - insulator, P - phosphor layer, B - base layer, Si - silicon substrate, Mi - micro mirrors

cess and the adaption to a particular custom defined display requires the redesign of the photo mask (M2) for the etch of the metal layer (M2).

There are different ways to realise an ASID practically. The simplest design of an ASID is shown in Figure 7.2. It consists of a metal base layer, the micro mirrors, the TFEL stack and the first metalisation layer. The metal base layer improves the reflection of the micro mirrors and reduces the influence of the Si-substrate (MIS-effect). The metal base layer can also be omitted. The facets are not etched. The generated light is deflected by the micro mirrors and emitted through the insulator layer with metal layer. The pixels are connected together to display elements and to the bond pads with small metalisation stripes (power rails), which are leading over the micro mirrors and unused pixels. Power rails that go over unused pixels also cause light emission along the power rail. Since the width of the power rail is small, the generated light is insignificant. The whole structure is to be sealed up with a transparent passivation layer for protection (not shown in Figure 7.2). This type of LETFEL ASID without base layer and passivation layer has been used for the demonstration of an ASID reported in section 7.4.

A simple design with etched facets is shown in Figure 7.3. The power rails lead

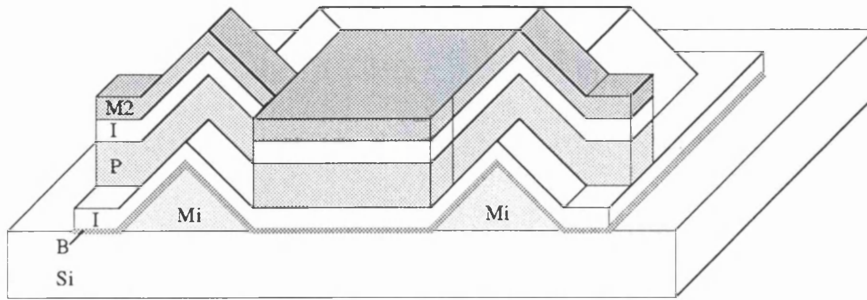

Figure 7.3: Basic LETFEL ASID with etched facets, without passivation layer; M2 - metal, I - insulator, P - phosphor layer, B - base layer, Si - silicon substrate, Mi - micro mirrors

over the mirrors. They are insulated through the TFEL-stack. The etch of the metal layer and TFEL-stack is done simultaneously with the same photo mask (metalisation mask). Alternatively, the etching of the metal layer and the TFEL stack can be done separately. In this case, an additional photo mask for the etch of the TFEL stack is required. The whole structure is to cover with a transparent passivation layer (not shown in Figure 7.3) in order to protect the phosphor layer from erosion.

A more complex ASID can be realised by employing a second metalisation layer. Figure 7.4 shows the Athena [36] process simulation of such an ASID. The basic device of this ASID consist of the metal base layer, the micro mirrors, the TFEL stack, the first metalization layer and the passivation layer with openings. The first metal layer is used for the top electrode. The second metal layer is used to connect the LETFEL pixel to display elements and to connect the display elements with the underplaying electronics and bond pads. The advantage this configuration is that the power rails do not cause any light emission. In addition, the improved design allows connections to underlaying integrated driver electronics and bond pads on SiO_2.

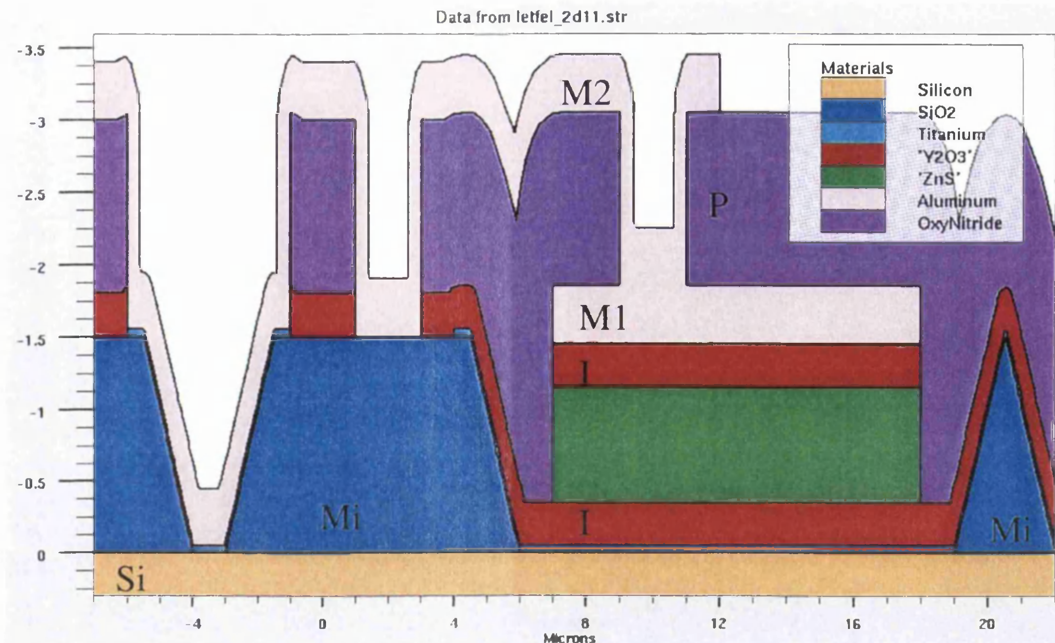

Figure 7.4: Complete ASID (process simulation), Si - silicon substrate, Mi - micro mirrors, Titanium - base layer, I - insulator, ZnS - phosphor layer, M1 - 1st metal, P - passivation, M2 - 2nd metal layer

7.2 Mask Set Design

The photo mask set design consists of 5 photo masks. Table 7.1 gives an overview of the photo masks and its use. Figure 7.5, showing a section of a device with square pixels, demonstrates how the masks are laid one upon another. All mask are designed for the use of positive photo resist.

The photo mask set has been designed in such a way that the most basic ASID without facet etch (masks Mi and M2); the basic ASID with etched facets (masks Mi and M2, optional with mask IPI) and the complete ASID can be realised with the same set of photo masks. The etch of the facets can be done either with the mask for the second metal etch M2 or with a special mask IPI, which is designed to create a distance of 2 μm between the facets of the TFEL stack and metal of the top electrode. So far, two masks of the set - mask Mi for mirror etch and

Mask No.	Mask Name	Process Step	Processed Material	Process Step No.
1	Mi	Etch oxide for micro mirrors	SiO_2	I.b
2	IPI	Etch TFEL stack (facets)	Y_2O_3, ZnS	
3	M1	Etch first metalisation layer (top contact)	Al	
4	P	Etch openings in passivation layer	SiON	
5	M2	Etch second metalisation layer (connections)	Al	III.b

Table 7.1: Overview Photo Masks, column 'Mask Name' refers to Figure 7.2, 7.3 and 7.4; column 'Process Step No.' refers to Figure 2.2

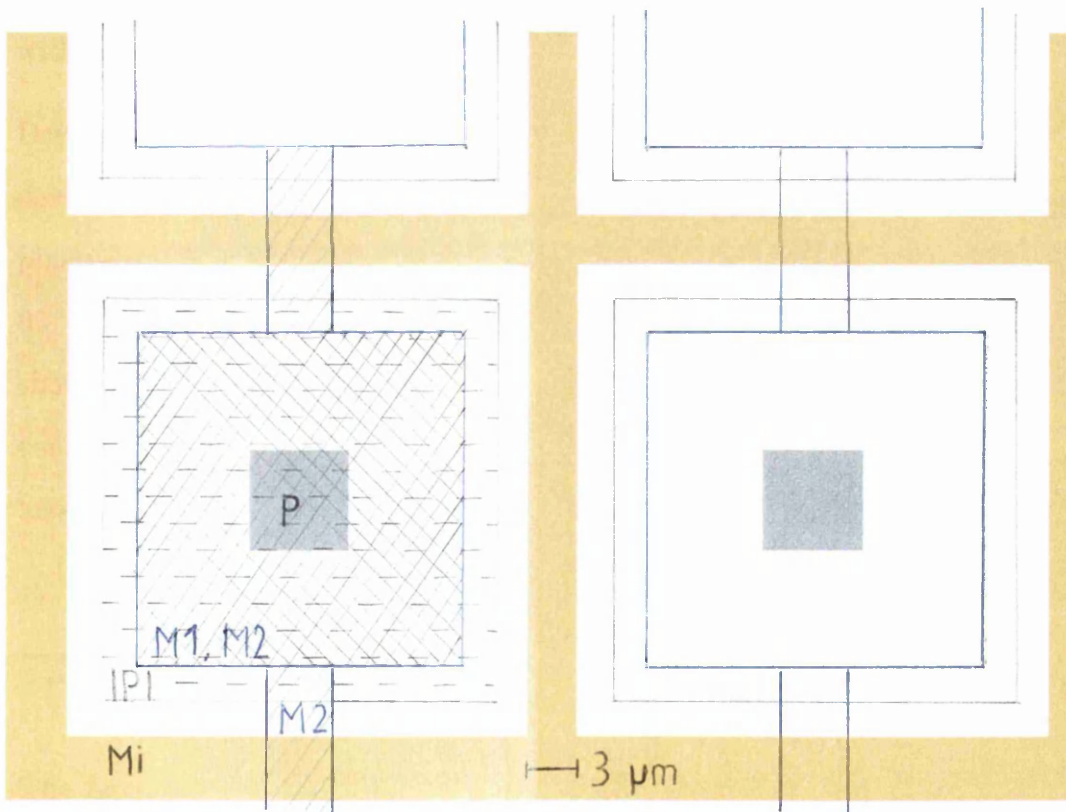

Figure 7.5: Section of Photo Masks, device with square pixels (s1_s02), Mi - micro mirrors, IPI - etch TFEL stack (facet etch), M1 - 1st metal layer, P - opening passivation, M2 - 2nd metal layer, see also Table 7.1

the mask M2 for second metal etch - have been produced and used for optical characterisation and demonstration of an ASID.

The design contains devices of two sizes - small devices with an active area of 1.4 mm by 1.4 mm and large device with an active area of 5 mm by 5 mm. Device set one contains small displays with pixels with different shapes (circular, square, hexagon) and eleven different pixel diameters from 10 μm to 220 μm. The appendix D shows the masks for the micro mirror etch and the second metal etch for displays with circular, square and hexagonal pixels. Device set two contains small devices with active and passive film waveguides (see Figure 6.1) of different length for measuring the attenuation. Devices of set three and four require the etch of the facets. They contain devices with light stripes (waveguides) and displays with pixels where the facets are periodical shaped.

Device set five is used for demonstration of the ASID concept. It contains basic devices with circular, square and hexagonal pixels with a diameter of 30 μm. The pixels are connected to provide light emitting stripes at an angle of 0°, 30°, 45°, 60 °and 90° referred to the direction of the bond pad. Figure D.7 in the appendix shows the photo mask for the metal etch as used for demonstrating the ASID concept. Additionally, devices for electrical characterisation and devices with an array of tips are also included in the mask design.

7.3 Characteristics of Different Pixel Structures

The light flux of displays with different shaped pixels and pixel diameters has been measured. Figure 7.6 shows the flight flux per total pixel area over the pixel diameter for circular, square and hexagonal pixels. The facets of the pixels are not etched. The process parameter are shown in Table B.4 (sample jrl) of the

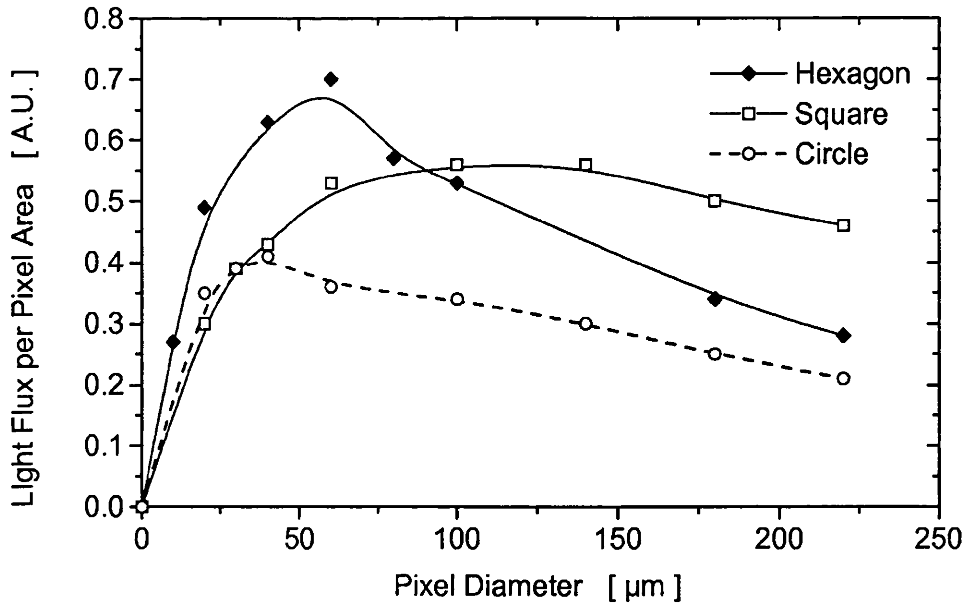

Figure 7.6: Light Flux per Pixel Area as a Function of the Pixel Diameter, for hexagonal, square and circle pixel structures, each dot represent the average of 4 measurementssample jr01 (Tab. B.4),

appendix.

The graph shows a distinct maxima at a diameter of about 40 μm for circular and of about 60 μm for hexagonal pixels. The maxima of a square pixel is less distinct at diameter of 100 μm to 150 μm. As predicted, the hexagonal pixel possesses the highest light area ratio and the circular pixel the lowest ratio. The light area ratio of a hexagonal pixel is about 30% higher than the light area ratio of a square pixel.

7.4 Demonstration of an ASID

Figure 7.7 shows a picture of a LETFEL ASID in operation. The display elements are a circle and stripes in different angles (0°, 30°, 45°,60°, 90°). Three ASIDs with the same legend are produced by employing basic display devices with circular, square and hexagonal pixels. The pixel diameter is 30 μm for all three pixel

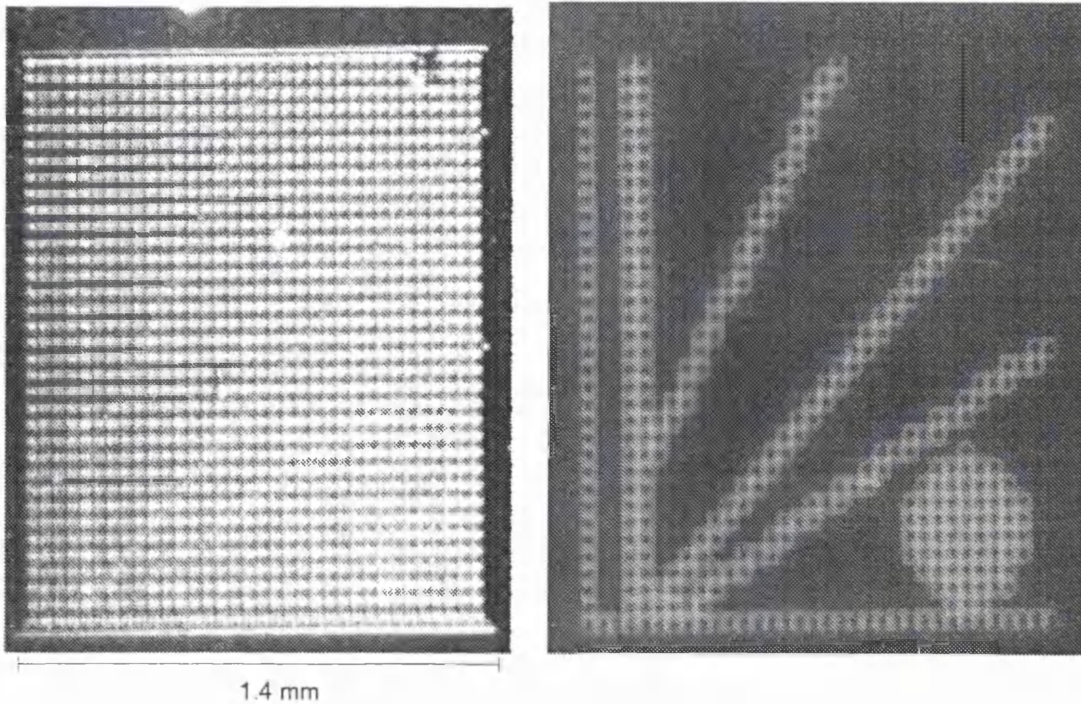

Figure 7.7: Demonstration of an ASID, left display switched off, right display switched on

shapes. The three different displays with the same legend have been compared to see whether any differences in the resolution could be observed with the naked eye. All three displays showed comparable results. Therefore, the shape of the pixels plays a minor role in terms of visibility, so that a basic display with square pixels is recommended, since legends are easier to design with square pixels.

Chapter 8

Conclusion and Future Work

A LETFEL display as an application specific display has been successfully demonstrated in this research programme. During the course of designing a practicable ASID, different theoretical models have been developed in order to estimate the characteristics of the future LETFEL device and thus to realize and avoid problems. Indeed, obtained simulation results did influence the decisions towards a practicable design. The other way round, data obtained by electrical and optical characterisation of the finally produced LETFEL devices have been used to prove the theoretical models.

Concluding, three different designs for an ASID are proposed. Each design is based on a basic display, where the final light emitting legend (contours) is defined by a metalisation layer. In that way, the redesign of photo lithographic masks could be reduced down to one mask for each custom specific display. The three designs are different in terms of fabrication complexity and resulting advantages. The easiest design has been used for demonstrating the ASID working principal and for characterisation purposes. The fabrication route is outlined in this thesis.

Different aspects of the static and transient electrical behavior of TFELs have

been investigated. The static charge-voltage characteristic is studied. It is the basis for transient electrical model and necessary for a correct measurement of the transfered charge and internal electrical field. Electrical models have been developed for the transient characteristics of TFEL devices. One model is based on the assumption that all interface electrons are located on a defined energy level (single interface state model), which led to two equivalent differential equations, similar to results obtained in [20]. The other model assumes distributed interface electron with respect to the energy, which led to a system of differential equations. Furthermore, a third model is discussed for the case that the interface distribution conserves the equilibrium distribution during the emission process. Supposed exchange of interface electrons between different energy levels occurs, a combination of the second and third model might be a more realistic approach.

The first two models are validated with experimental results. The simulated results are in a satisfying agreement with the measured results depending on the preparation method of the samples. However, a more comprehensive validation by using different driving waveforms are necessary and could be part of a future work. Despite its importance, a conclusive picture of the interface properties could not be revealed by matching the model with the observation. Also, the measurement of the interface distribution has been attempted in different ways during the course of research, yet no clear result could be obtained. Principally problems of measuring the interface electron distribution are pointed out.

A method to simulate the electrostatic field distribution has been developed and employed to find out weak points in the design. It could be shown that the field strength between the tip of the micro mirror and the metal layer is not as high as initially expected. Moreover, the influence of the MIS capacity are analysed. MIS effects exist in the presently used LETFEL devices and must thus be taken into

consideration when electrical measurements are carried out. In order to quantify the influence of the MIS on the device operation, the surface generation rate of the Silicon-Yttrium oxide interface needs to be measured, which can be part of a future investigation. A way to avoid the influence of the MIS-effect and resulting disadvantages from the start, is to use a metal base layer between TFEL stack and silicon contact.

Equivalent RC-models are deduced on a theoretical base from the physical model of a TFEL device. The RC-models are developed for TFELs with single interface states and distributed interface states. They could be proved as a realistic electrical model of TFELs. The simulated characteristics are in a good agreement with measured characteristics, especially for non-annealed devices. They are therefore sufficient for embedded simulation of driver electronics and TFELs. Nevertheless, a more extensive validation of the models with experimental results is still to be done as a future work.

The design of the ASID is primarily based on an array of light emitting pixels. That raises the problem, which shape and diameter of the pixel is the most efficient. For estimating the outcoupled light, a general ray optics model for two-dimensional pixel structures has been developed. The model was subsequently applied to circular, square and hexagonal LETFEL pixel structures and the outcoupled light was estimated for these three pixel structures. Since only displays with unetched facets were available with the present technology, the model could only be compared with measurements under the assumption that the pixels have an angle of total reflection of 90°. The simulations are in good agreement with measured results for that particular case. However, the validation of the model with experimental results need to be extended especially for displays with etched facets. This will be objective of future investigations.

For producing LETFEL displays and demonstrating an ASID, a set of photo masks has been designed and partly produced. The ASID principle is demonstrated with the simplest possible design. A more complex and sophisticated ASID can be built with the complete set of photo masks. Last but not least, the mask set contains many more new displays, which still need to be investigated. Despite the achievements and progress in TFELs and LETFELs research, the TFEL principle provides enough room for further research and new concepts.

Bibliography

[1] R. Mach, G. O. Müller: Physical Concepts of High-Field, Thin-Film Electroluminescence Devices; phys. Stat. Sol(a) 69, 11 (1982).

[2] H.Venghaus: Current and Light Generation in UV-irradiated AC TFEL devices, Journal of Crystal Growth 59, 1982, 403-408

[3] Wayne Mark Cranton; PhD Thesis, University of Bradford, 1995

[4] S. Kobayashi, J.F. Wagner and Abu-Dayah: Distribution of Trapped Electrons at Interface States in ACTFEL Devices

[5] A. Aguilera, V. P. Singh, D. C. Morton: Electron Energy Distribution at the Insulator-Semiconductor Interface in AC Thin Film Electroluminescence Display Devices, IEEE Transactions Electron Devices, Vol. 41, No. 8, August 1994.

[6] W. Busse, H.-E. Gumlich, A. Geoffrey and R. Parrot: Spectral Distribution and Decay Times of the Luminescence of Mn^{2+} on Different Lattice Sites in ZnS; phys. stat. sol. (b) 93, 591 (1979)

[7] G. O. Mueller: Electroluminescent Displays; SID 1987, p. 3.1

[8] R. Mach and G.O. Müller: Efficiency and Saturation in AC Thin Film EL Structures; phys. stat. sol. (a) 81, 609 (1984)

[9] R. Törnqvist: Manganese concentration dependent saturation in ZnS:Mn thin film electroluminescent devices; J. Appl. Phys. 54 (7), July 1983, p. 4110

[10] G. O. Mueller: Characterisation of Thin Film Electroluminescent Devices; SID, Electroluminescence Proceedings 1992

[11] R. Stevens, C. B. Thomas and W. M. Cranton: Enhancing the Brightness of Thin-Film Electroluminescent Displays by Improving the Emission Process; IEEE Elec. Dev. Lett., 15 (3),1994, pp.97-99

[12] C. B. Thomas, W. M. Cranton, I. P. Mc Clean, M.R. Craven, and A.H. Abdullah: Laterally emitting TFEL displays devices', Society for Information Display International Symposium, 1995, pp.887-890

[13] R. Stevens, C. B Thomas and W. M. Cranton; Appl. Phys. Lett., 63 (1993), pp. 3119-3121

[14] Y. H. Lee, B. K. Ju, M.-H. Song : White-Light Emitting Thin-Film Electroluminescent Device Using Micromachined Structure; IEEE Transaction on Electron Devices, Vol. 44, No. 1, Jan. 1997, pp. 39-44

[15] S. O. Barros: Enhancement of the light outcoupling of alternating current laterally emitting thin film electroluminescent devices. PhD Thesis, The Nottingham Trent University, July 2000

[16] M.R. Craven; PhD Thesis, The Nottingham Trent University

[17] R. Stevens; PhD Thesis, University of Bradford, 1994

[18] C. B. Thomas, I..P. Mc Clean, R. Stevens and W. M. Cranton: TFEL optoelectronic integrated circuits on Si, Electronic Letters, 1994, Vol.30, No.16, p.1350

[19] P. M. Alt:Thin-Film Electroluminescent Displays: Device Characteristics and Performance; Proceedings of the SID, Vol. 25/2, 1984

[20] E. Bringuier: Charge Transfer in ZnS-type electroluminescence; J. Appl. Phys.66 (3), 1 August 1989.

[21] R. Khormaei and C. Walker: Modeling the Electron Emission in ACTFEL Devices;

[22] K. A. Neyts: Simple Model for Hysteretic Behaviour of Thin Film Electroluminescence Devices, IEEE Transaction on Electron Devices, Vol. 38, No. 12 December 1991, p.2604.

[23] W. E. Howard, O. Sahni, P. M. Alt: A Simple Model for the hysteretic behaviour of ZnS:Mn Thin Film Electroluminescence Devices, J. Appl. Phys. 53 (1), January 1982.

[24] J. M. Jarem and V. P. Singh: A Computational Simple Model for Hysteretic Thin Film Electroluminescent Devices, IEEE Transaction on Electron Devices, Vol. 35, No.11, Nov. 1988

[25] K. A. Neyts and P. De Visschere: Analytical model for thin-film electroluminescent devices; J. Appl. Phys. 68 (8), 15 Oct. 1990

[26] A. Möschwitzer, K. Lunze: ' Halbleiterelektronik 'Lehrbuch, VEB Verlag Technik Berlin, 1988.

[27] A. S. Dawydow: ' Quanten Mechanik ', VEB Deutscher Verlag der Wissenschaften, Berlin 1987

[28] G. Vincent, A. Chantre, D. Bois: Electric field effect on the thermal emission of traps in semiconductor junctions; J. Appl. Phys. 50 (8), August 1979.

[29] D. H. Smith: Modelling a.c. Thin-Film Electroluminescence Devices, J. of Luminescence 23 (1981), 209-235.

[30] Using MATLAB, Version 5.3 (Release 11), The Math Works Inc.

[31] E. H. Nicolian and J. R. Brews: ' MOS Physics and Technology '; A Wiley-Interscience Publication 1982

[32] P. Bräunlich: ' Thermally Stimulated Relaxation in Solids '; Topics in Applied Physics Vol. 37,Springer Verlag, 1979

[33] S. M. Sze: Physics of Semiconductor Devices. A Wiley-Interscience publication

[34] D. K. Schroeder: ' Advanced MOS Devices ' . Addision-Wesley Publishing Company

[35] Atlas User's Manual, Device Simulation Software; Silvaco International, October 1996.

[36] Athena User's Manual, Process Simulation Software; Silvaco International, April 1997.

[37] D. H. Smith: Modeling a.c. Thin-Film Electroluminescent Devices; J. of Luminescence 23 (1981), 209-235.

[38] M. Aberg: An Electroluminescent Display Simulation System and its Application for Developing Grey Scale Driving Methods; Acta Polytechnica Scandinavica, Electrical Engineering Series No. 74, Helsinki 1993.

[39] J. Davidson, J. F. Wager, R. Khormaei: Electrical Characterization and SPICE Modeling of ZnS:Mn ACTFEL Devices; SID 91 Digest, 1991.

[40] V. P. Singh and Qin Xu: Phosphor currents in ZnS:Mn ac thin film electroluminescent display devices; J. Appl. Phys. 72 (9), 1. Nov. 1992, p4148.

[41] M. Ylilammi: Analytical Circuit Model for Thin Film Electroluminescent Devices, IEEE Transaction on Electron Devices, Vol. 42, No. 7, July 1995

[42] Silvaco Smart-Spice Manual; Silvaco International

[43] Yoshima A. Ono: ' Electroluminescent Display ', Series on Information Displays, Vol.1

[44] Ebeling, K. J.: ' Integrierte Optoelektronik ', Springer Verlag, 1992

[45] D. Mende and G.Simon: ' Physik - Gleichungen und Tabellen ' (Fachbuchverlag Leipzig, Leipzig, 1988)

[46] Scanwell LtD. : Documentation LETFEL Ion Etcher

[47] D. M. Manos, D. L. Flamm: ' Plasma Etching - An Introduction ' ; Academic Press Inc., 1989.

[48] V. P. Singh, S. Krishna: Electric field and conduction current in ac thin film electroluminescent display devices; J. Appl. Physics, 70 (3), 1. Aug. 1991

[49] V. P. Singh, W. Z. Majid, D. C. Morton: Analysis Of ZnS:Mn-type ac thin film electroluminescence display devices with bulk traps; SID 1993.

[50] L. E. Tannas : Flat Panel Displays and CRTs.

[51] ONO, Y. A.: ' Electroluminescent Displays ' (World Scientific, 1995)

[52] M. Ylilammi: Preparation and Analysis of Thin Film Electroluminescent Devices; Acta Polytechnica Scandinavia, No. El 86 Helsinki 1996.

Appendix A

Exact Q-V Characteristic

The charge-voltage characteristic is calculated by solving the Poisson's equation. Since the charges in this model are concentrated in thin layers (see Figure 3.1) and possible space charge in the phosphor layer is neglected, the problem can be solved easier with Gauss's Law applied separately for each layer. Firstly, the electrical displacement density D is calculated, with that follows the electrical field F and subsequently the voltage drop V across that layer. For $Q_I = -Q_I^*$, $F_p(x)$ =constant and with equal insulator layers on both sides (symmetrical device), one gets for

Insulator Layer 1 :

$$D_{i1} = Q_d/A \tag{A.1}$$

$$F_{i1} = D_{i1}/\epsilon_i = \frac{Q_d}{\epsilon_i \cdot A} \tag{A.2}$$

$$V_{i1} = d_{i1} \cdot F_{i1} = \frac{1}{2} Q_d/C_i \tag{A.3}$$

Phosphor Layer :

$$D_p = (Q_d + Q_I^*)/A \tag{A.4}$$

$$F_p = D_p/\epsilon_p = \frac{Q_d + Q_I^*}{\epsilon_p \cdot A} \tag{A.5}$$

$$V_p = d_p \cdot F_p = (Q_d + Q_I^*)/C_p \tag{A.6}$$

Insulator Layer 2 :

$$D_{i2} = (Q_d + Q_I^* + Q_I)/A = Q_d/A \tag{A.7}$$

$$F_{i2} = D_{i2}/\epsilon_i = F_{i1} \tag{A.8}$$

$$V_{i2} = d_i \cdot F_{i2} = V_{i1} \tag{A.9}$$

where A is the active device area, $\epsilon_i = \varepsilon_i \varepsilon_0$, ε_i is the relative permeability of the insulator material, $\epsilon_p = \varepsilon_p \varepsilon_0$, ε_p is the relative permeability of the phosphor material, d_p and d_i are the thickness of the phosphor and insulator layer respectively, Q_I is the interface charge and Q_d is the external charge on the electrode. In the formula above the subscripts $i1$, p and $i2$ refer to the insulator layer1 , the phosphor layer and the insulator layer 2 respectively. The device Voltage V_d is then the sum of the voltage drops over all three layers:

$$V_d = V_{i1} + V_p + V_{i2} = 2V_{i1} + V_p \tag{A.10}$$

$$= Q_d \left(\frac{1}{C_i} + \frac{1}{C_p} \right) + \frac{Q_I^*}{C_p} \tag{A.11}$$

$$V_d = \frac{Q_d}{C_{ip}} - \frac{Q_I}{C_p} \tag{A.12}$$

where the TFEL capacity C_{ip} is the TFEL capacity (3.2), the phosphor layer capacity C_p and the insulator layer capacity C_i are defined in (3.3). Rewriting

equation (A.12), one gets

$$Q_I = Q_d/\alpha - C_p V_d \quad . \tag{A.13}$$

Furthermore, by using (A.13), equation (A.5) becomes an equation for the field in the phosphor layer

$$F_p = \frac{1}{d_p}\left(V_d - \frac{Q_d}{C_i}\right) \tag{A.14}$$

$$F_p = \frac{1}{d_p}\left(\alpha V_d - \frac{Q_I}{C_p + C_i}\right) \tag{A.15}$$

The transfer current in the phosphor layer is $I_t = dQ_I/dt$ and the total device current is $I_d = dQ_d/dt$. When equation (A.13) is differentiated with respect to t, it follows the transfer current as

$$I_d/C_{ip} - I_t/C_p = \frac{dV_d}{dt} \tag{A.16}$$

Appendix B

Process and Device Parameter

STEP	PROCESS	DETAILS
I.	base layer deposition	DC sputter deposition, TiW, (at Rutherford Apelton Laboratory)
II.a	deposition insulator layer	Ar- RF- sputter deposition, Y_2O_3, $d =$ 0.3 μm, T=190° C, t$\simeq$ 3h
II.b	deposition phosphor layer	Ar - RF- sputter deposition, ZnS, $d =$ 0.8 μm, T=190° C, t$\simeq$ 2h
II.c	deposition insulator layer	Ar - RF- sputter deposition, Y_2O_3, $d =$ 0.3 μm, T=190° C, t$\simeq$ 3h
II.d	thermal annealing (optional)	t=1h, T=400° C, in vacuum p=10^{-7}mbar
III.	metal layer deposition (top contact)	thermal evaporation, Al through contact mask
IV.	metal layer deposition (back contact)	thermal evaporation, Al

Table B.1: Process steps and process parameter for TFEL devices, sample wafer jr2, jr2a thermally annealed, jr2b non-annealed

	MATERIAL	VALUE	COMMENTS
Insulator Layer	Y_2O_3	$d_i = 0.3$ μm	Interferometry
Phosphor Layer	ZnS	$d_p = 0.8$ μm	Interferometry
	Mn	0.43 wt%	
Top Contact	Al	2 μm thick	
Back Contact	Si	3 μm thick	
Permittivity	ZnS	$\epsilon_p = 7.5\varepsilon_0$	Q-V measurement
	Y_2O_3	$\epsilon_i = 12\varepsilon_0$	Q-V measurement

Table B.2: Process and Device Parameter for Sample jr2a (thermally annealed) and jr2b (non-annealed)

STEP	PROCESS	DETAILS
I.a	Deposition SiO_2	Steps I.a-I.d processed by QUDOS Ltd.
I.b	Photolithography	Positive resist, mask Mi
I.c	Reactive etch	
I.d	Strip resist	
I.a	Deposition insulator layer	Ar- RF- sputter deposition, Y_2O_3, $d = 0.3$ μm,
		T=190° C, t$\simeq$ 3h
II.b	Deposition phosphor layer	Ar - RF- sputter deposition, ZnS, $d = 0.8$ μm,
		T=190° C, t$\simeq$ 2h
II.c	Deposition insulator layer	Ar- RF- sputter deposition, Y_2O_3, $d = 0.3$ μm,
		T=190° C, t$\simeq$ 3h
II.d	Thermal annealing	t=1h, T=400° C, in vacuum p=10^{-7}mbar
III.a	Metal layer deposition (top contact)	thermal evaporation, Al
III.b	Photolithography	positive resist, mask M2
III.c	Etch top electrode	Ar sputter etch
III.d	Strip resist	Asher
IV.	Metal layer deposition (back contact)	thermal evaporation, Al

Table B.3: Process steps and process parameter for LETFEL devices, sample wafer jr1

	MATERIAL	VALUE	COMMENTS
Insulator Layer	Y_2O_3	$d_i = 0.3$ μm	Interferometry
Phosphor Layer	ZnS	$d_p = 0.8$ μm	Interferometry
	Mn	0.43 wt%	
Top Contact	Al	2 μm thick	
Back Contact	Al	3 μm thick	
Annealing	time temperature	1 hour 400° C	

Table B.4: Device Parameter for Sample jr01 (thermally annealed)

Appendix C

Compensator Circuit

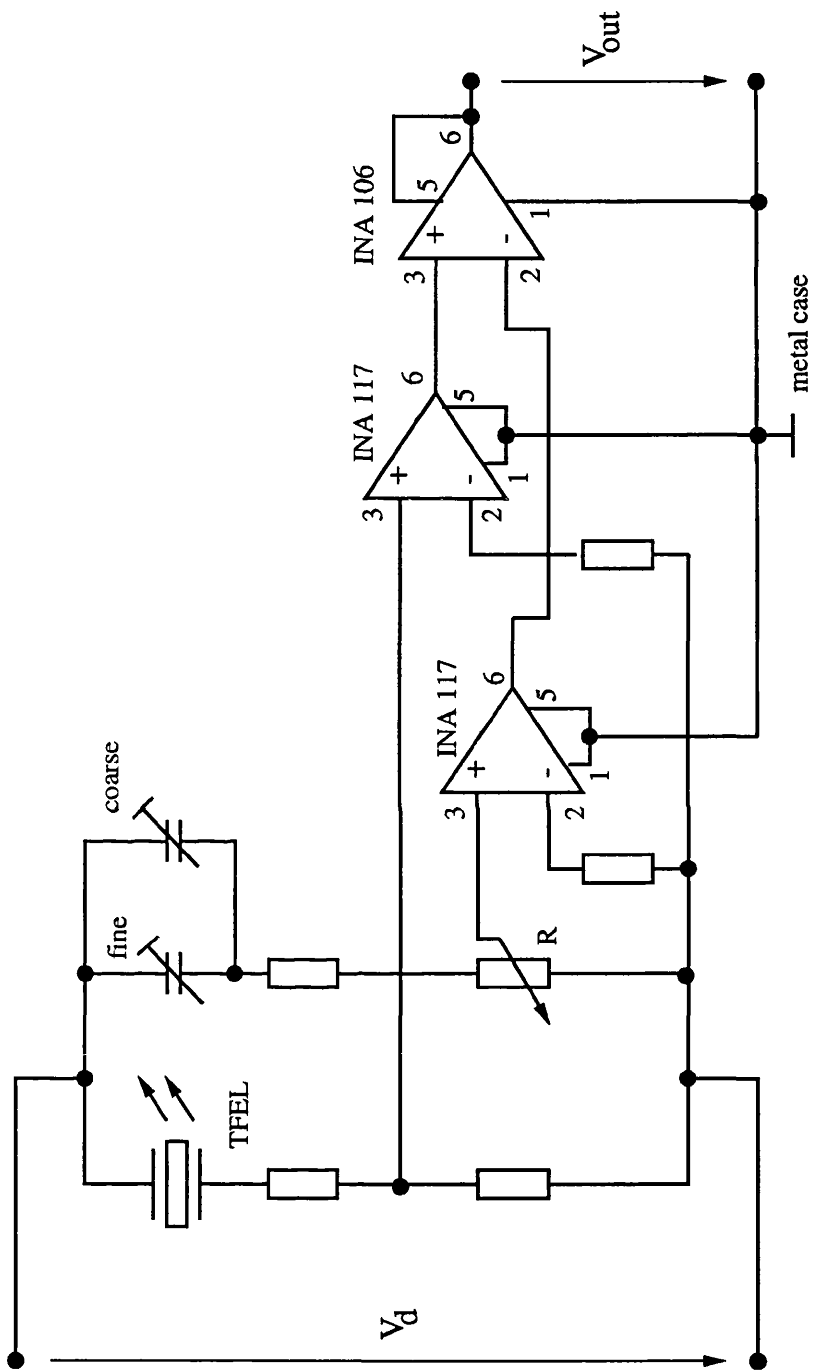

Figure C.1: Compensator circuit for measuring the transfer current

Appendix D

Photolithographic Masks

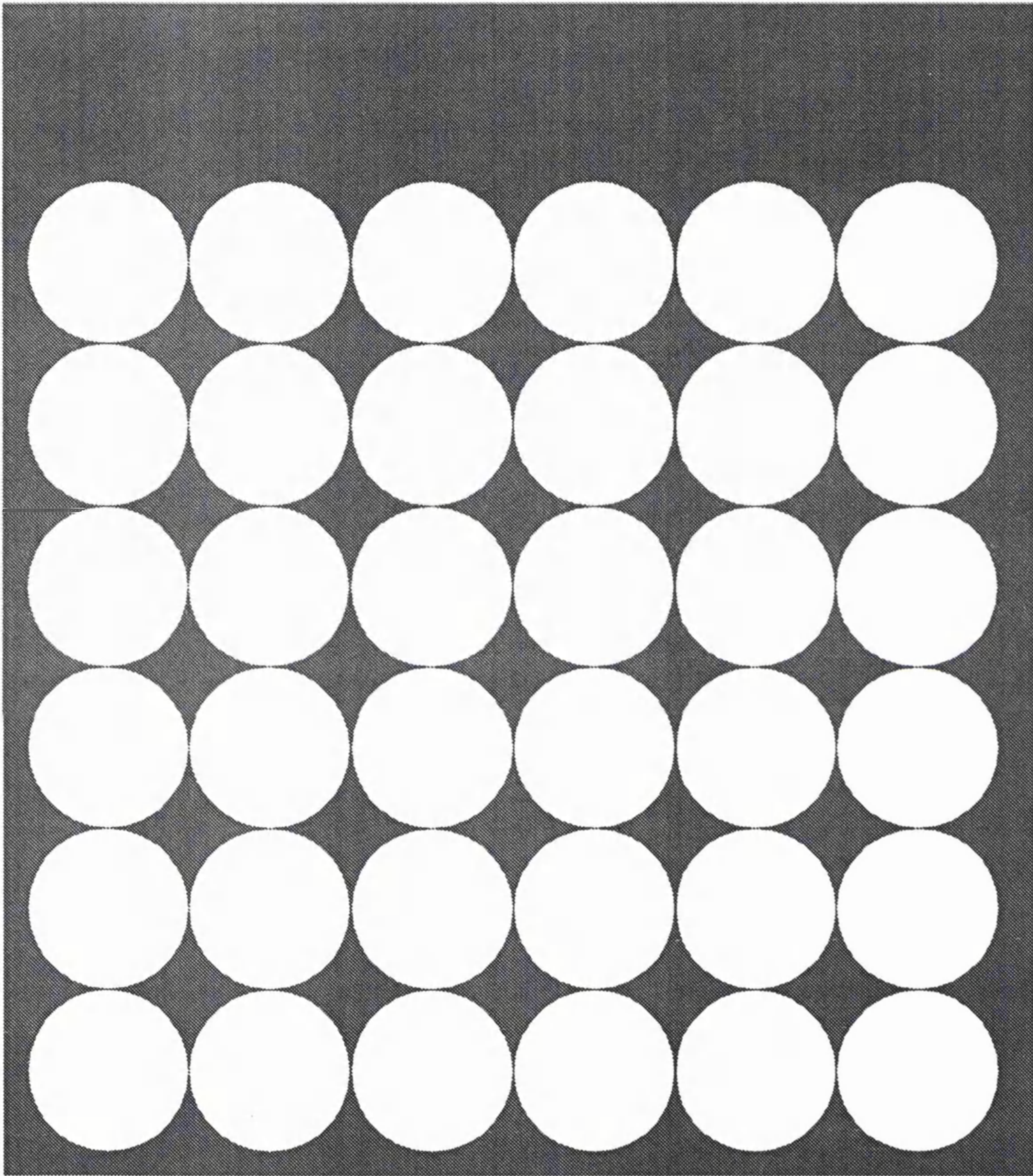

Figure D.1: Photo mask for micro mirror etch (Mi), device s1_c22, circular pixel, pixel diameter D=220 μm

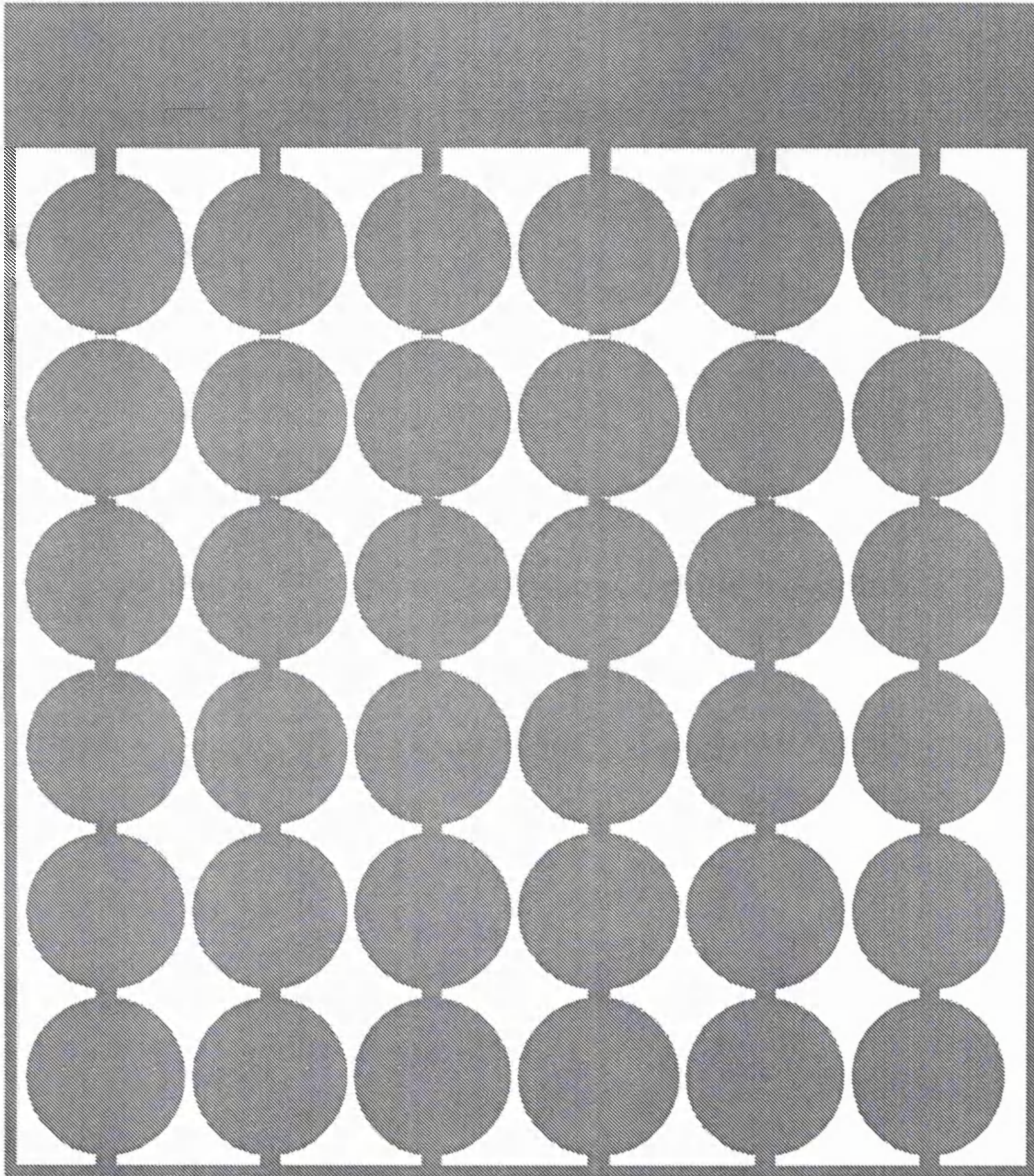

Figure D.2: Photo mask for metal etch (M2), device s1_c22, circular pixels, pixel diameter D=220 μm

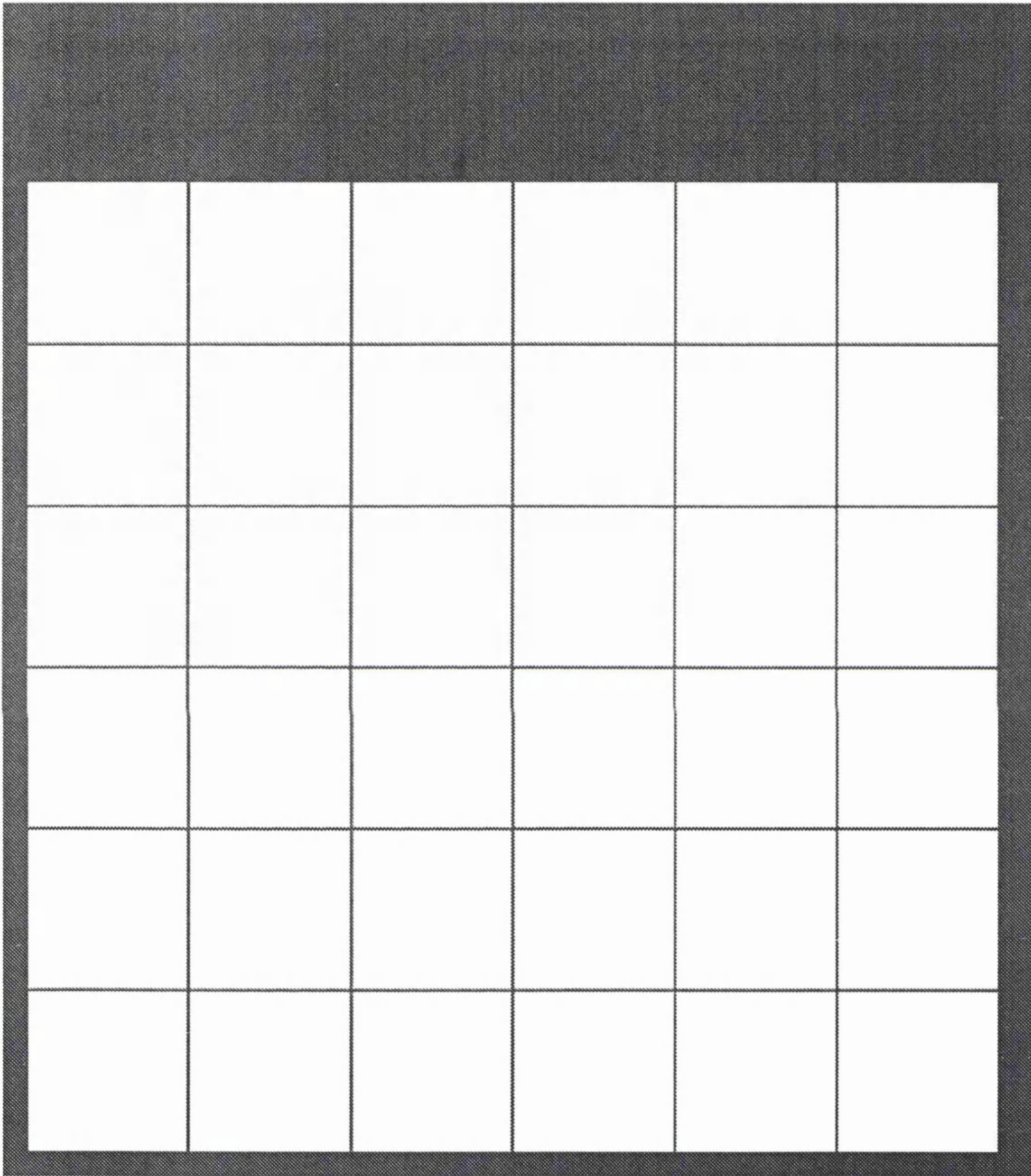

Figure D.3: Photo mask for micro mirror etch (Mi), device s1_s22, square pixel, pixel diameter D=220 μm

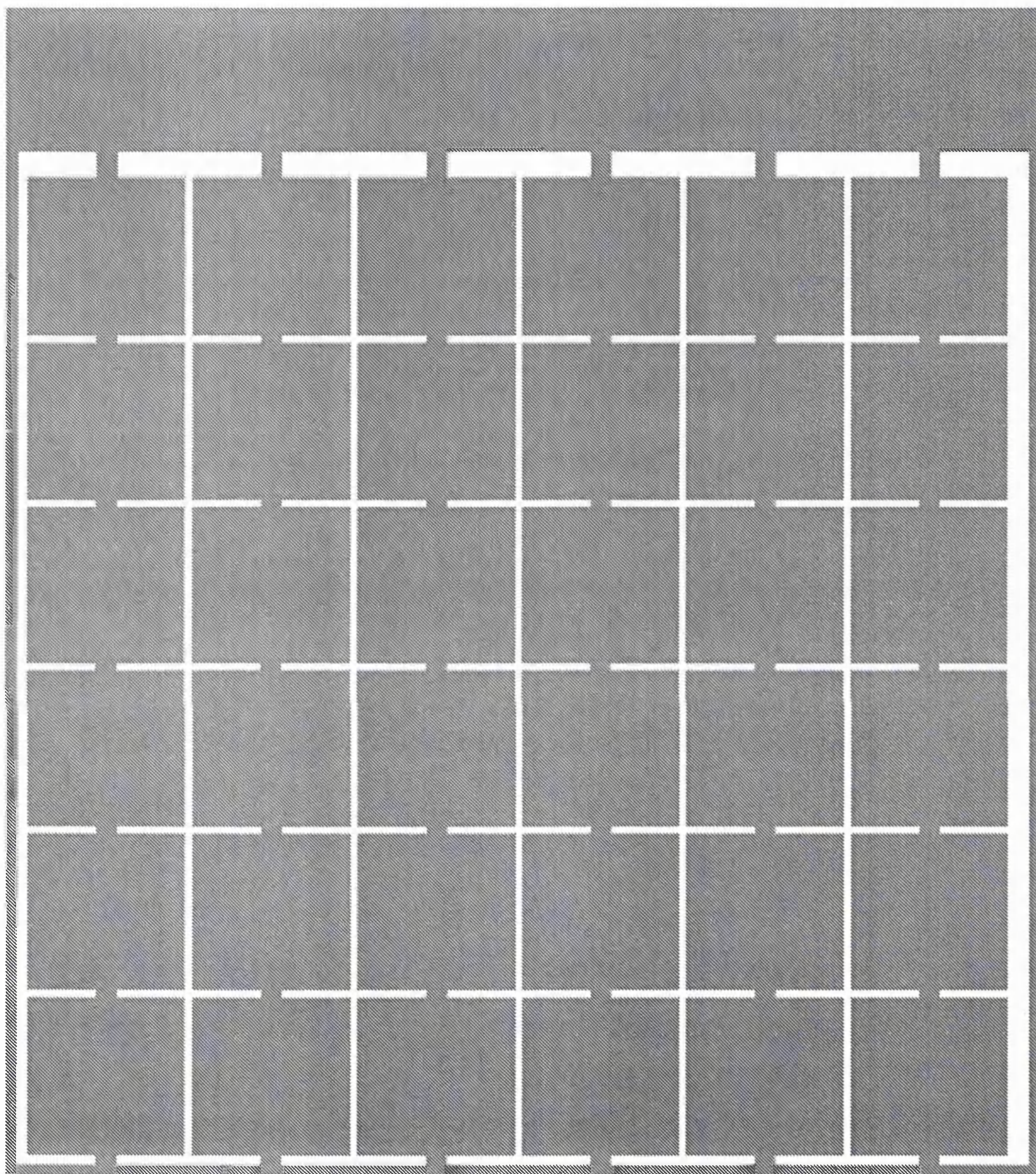

Figure D.4: Photo mask for metal etch (M2), device s1_s22,square pixels, pixel diameter D=220 μm

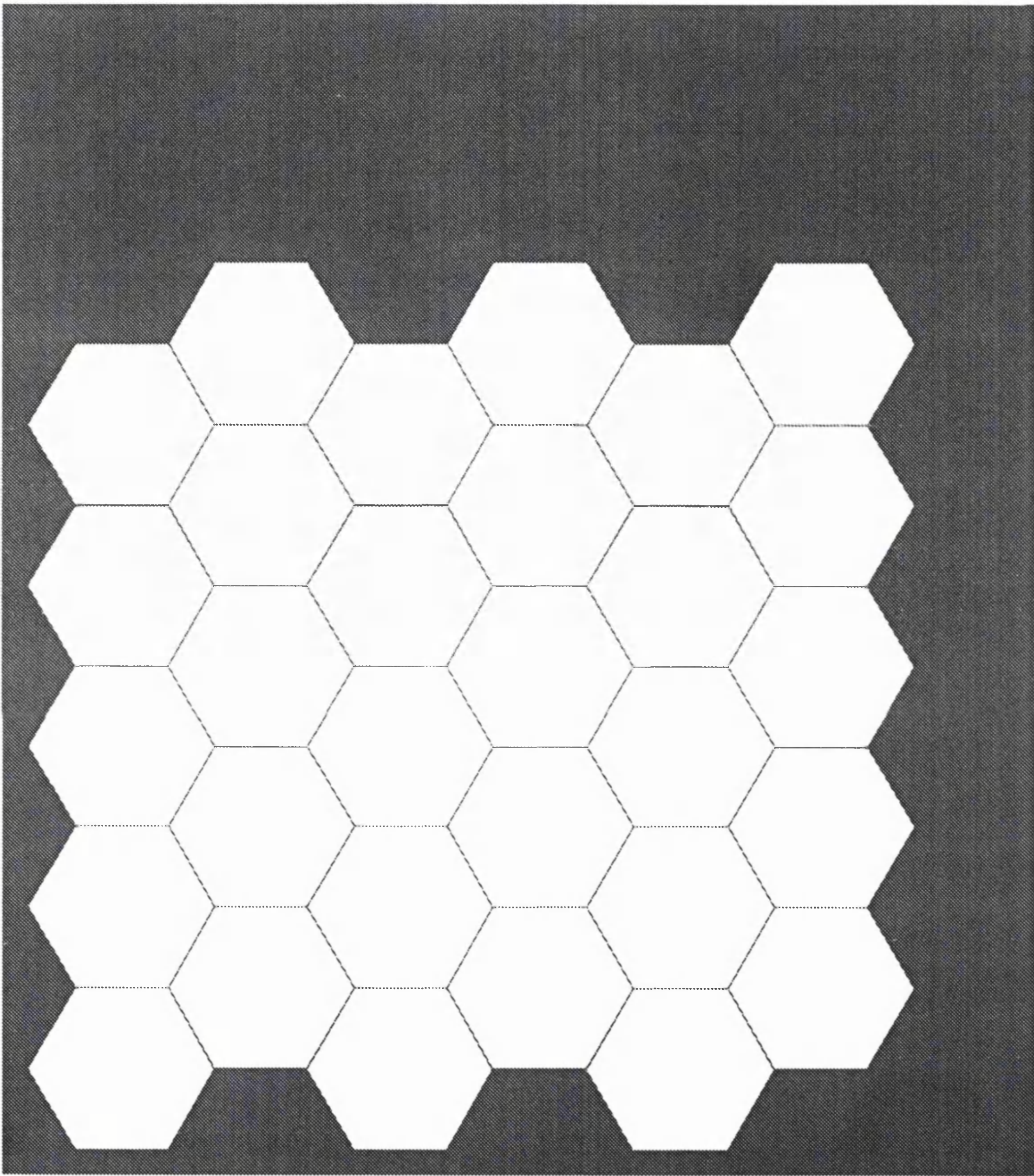

Figure D.5: Photo mask for micro mirror etch (Mi), device s1_h22, hexagonal pixel, pixel diameter D=220 μm

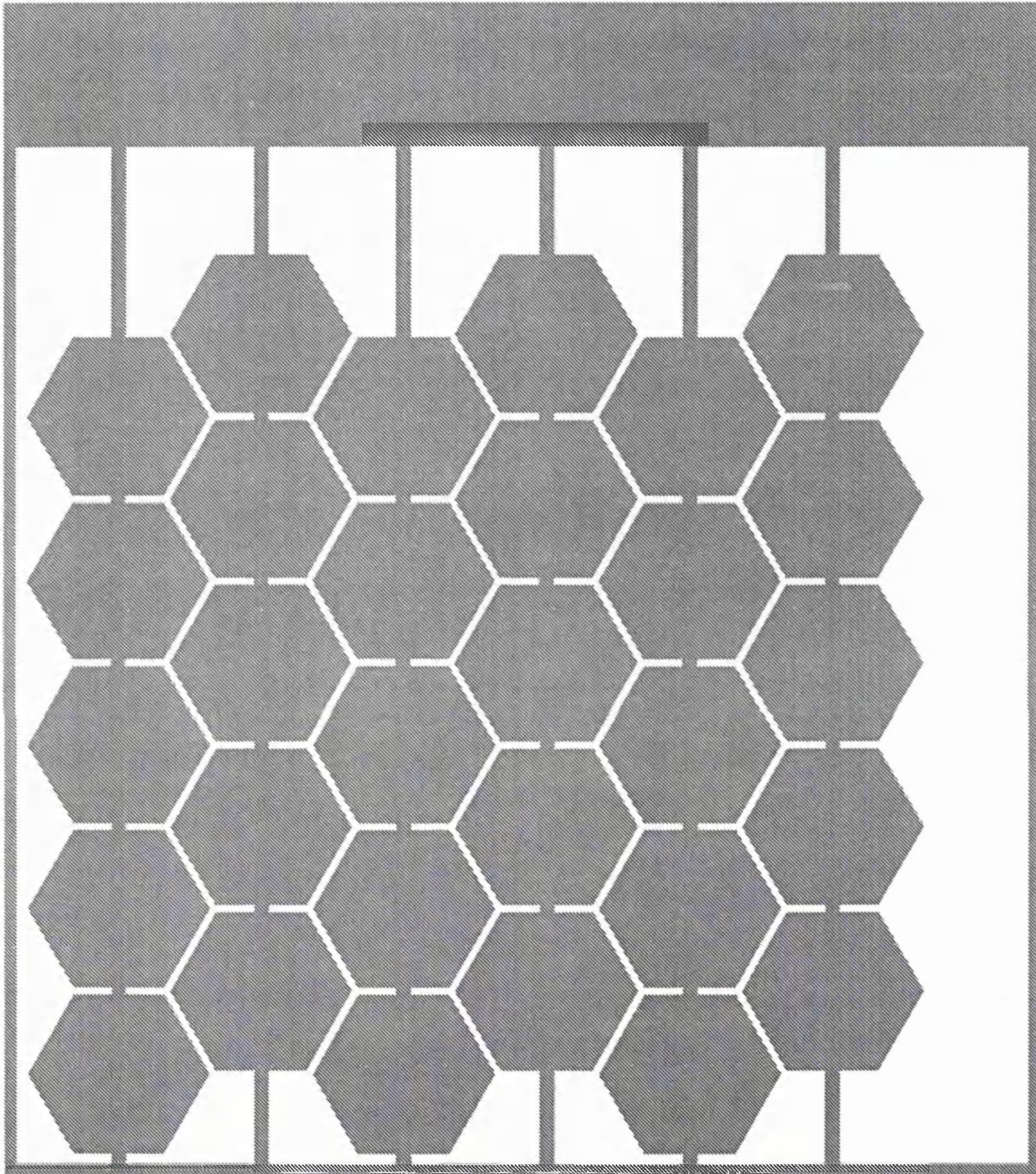

Figure D.6: Photo mask for metal etch (M2), device s1_h22, hexagonal pixels, pixel diameter D=220 μm

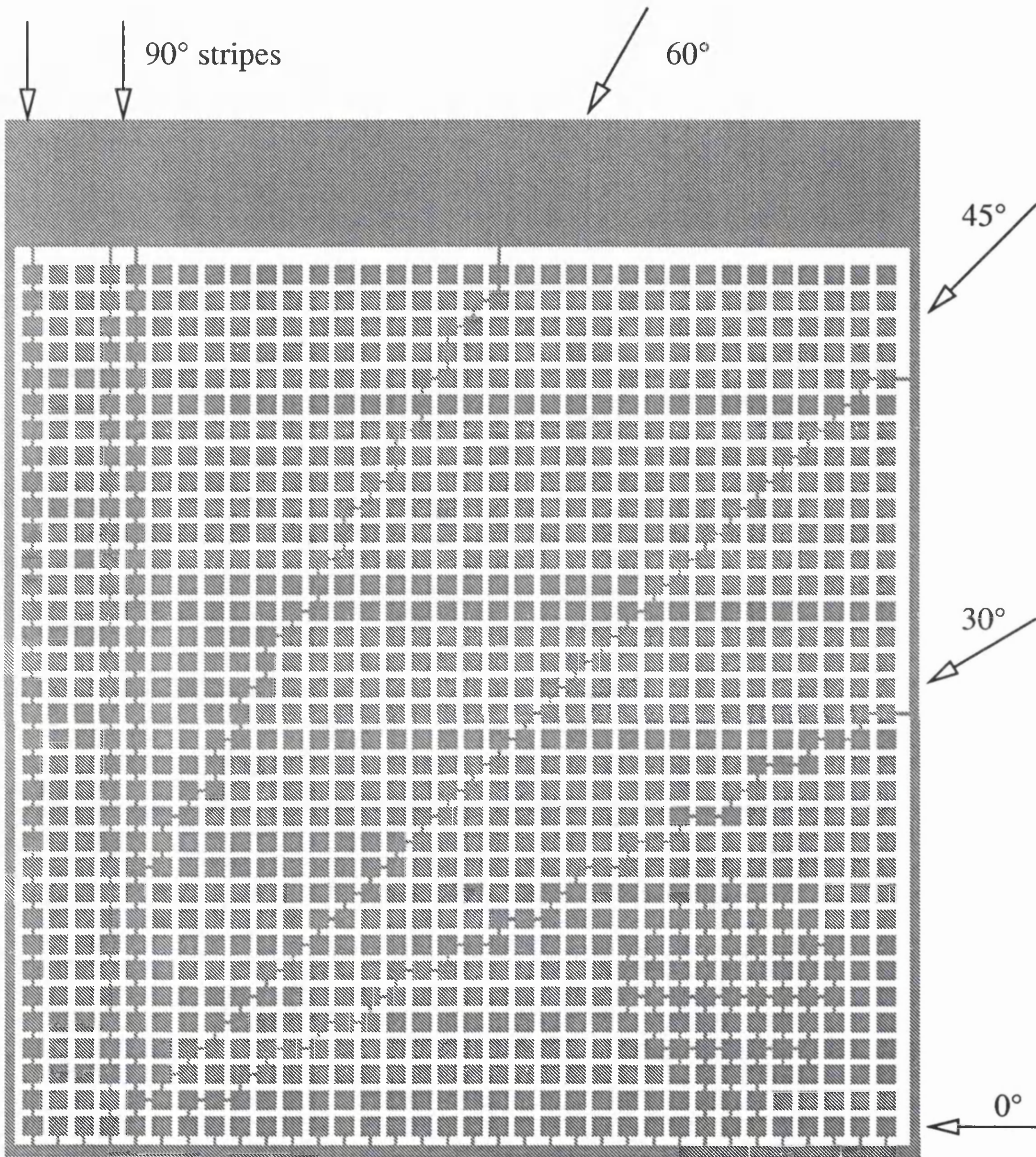

Figure D.7: Photo mask for metal etch (M2), device s8_s03, device for ASID (connected), square pixels, pixel diameter D=30 μm

Appendix E

Magnet Enhanced Ion Etch

The aim of this study is to investigate the feasibility of using the Scanwell Ion Etcher for etching the facets of the LETFEL devices. The working principle of the Scanwell Ion Etcher is described in [46]. The etcher is a conventional ion etcher [47], which uses permanent magnets for enforcing the etch process. During the etch process, the magnets are continously moved (magnet sweep) to obtain a uniform etch rate over the wafer surface. All experiments reported here are done with a magnet sweep and under an argon gas atmosphere.

The Etcher works in a pressure range from 3 mTorr to 23 mTorr. Under 3 mTorr, no plasma can be ignited. A pressure of 23 mTorr is the maximal adjustable pressure. The applied RF-Power can be adjusted between 50 W and 900 W. Under 50 W, the plasma can not be ignited, whereas it gets unstable over 900 W. The surface area of the bottom electrodes is A=1385 cm^2.

Etch experiments have been performed for the materials Si, Y_2O_3, ZnS, SiON, Al and TiW. To examine the etch rate, a Si-wafer is coated with a thin layer of the material to be investigated. After coating, the wafer is masked with photo resist. The etching follows then under defined process conditions. The resist is

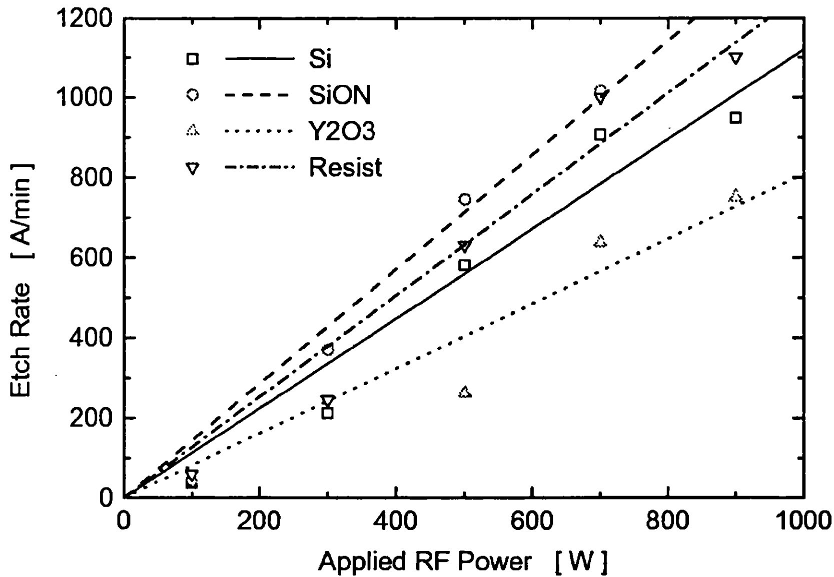

Figure E.1: Etch Rate versus RF Power for Si, SiON, Y_2O_3 and Photo Resist; Pressure p=3 mTorr

removed with an asher after the etching process. Finally the measurement of the etch profile is performed with a DEKTAK profile measurement system.

Table E.2 and Figures E.1, E.2, E.3 show the etch rates in A/min and the standard deviation for the investigated materials depending on the applied RF power. The etch rates and standard deviations for Si, SiON resist depending on the pressure are shown in Table E.1 and Figure E.4. The standard deviations of the etch rates are about 10 % and thus the uniformity is sufficient.

The surface quality and facet roughness of the etched Y_2O_3 samples have been investigated with a scanning electron microscope. Figure E.5 shows the surface of an etched Y_2O_3 sample. The facets are straight. The etched surface exhibits a vast amount of etching pits, likewise the unetched area exhibits humps. Thus the use of magnet enhanced ion etch seems not to be feasible for producing LETFEL displays because of the damaging of the insulator layers.

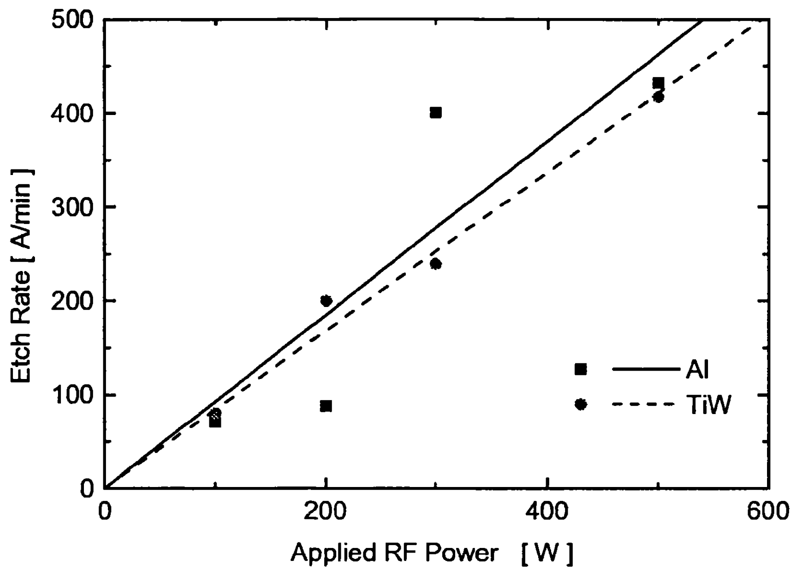

Figure E.2: Etch Rate versus RF Power for Al, and TiW; Pressure p=3 mTorr

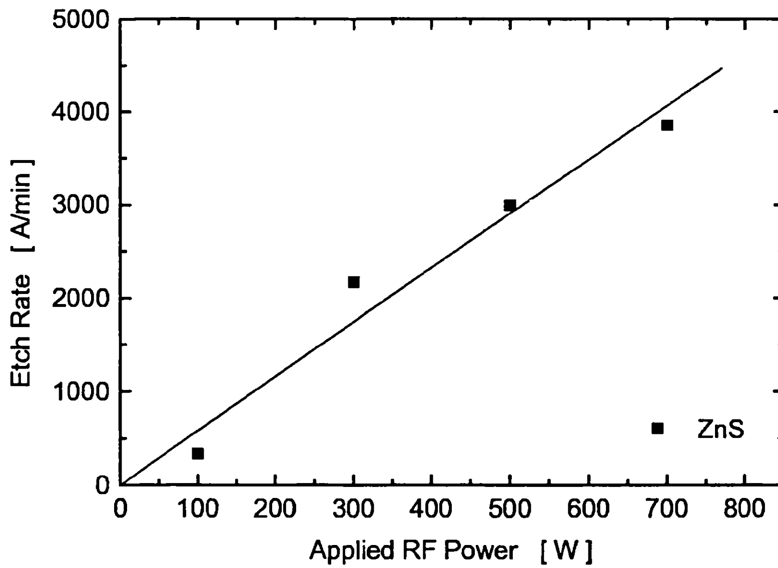

Figure E.3: Etch Rate versus RF Power for ZnS; Pressure p=3 mTorr

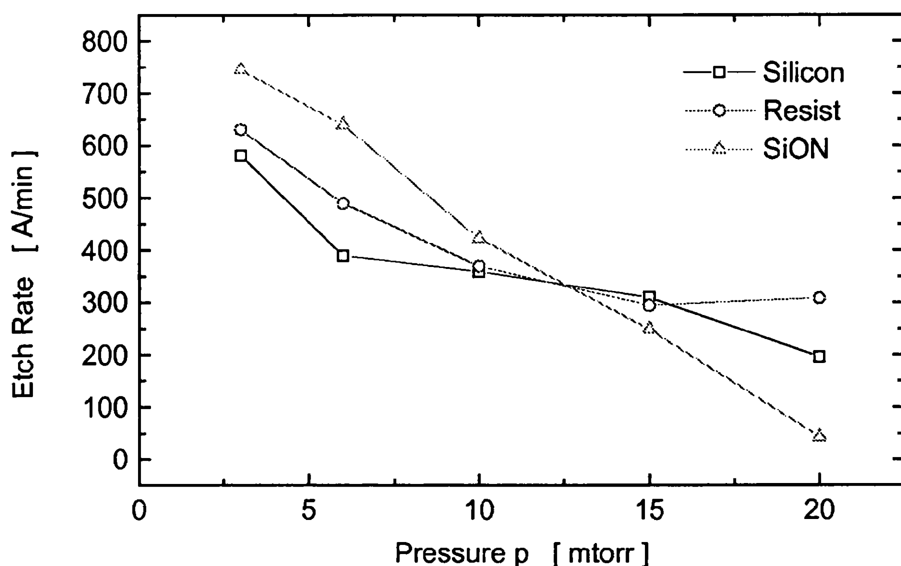

Figure E.4: Etch rate in A/min for an applied RF Power P=500 W

PRESSURE	MATERIAL:	Si	SiON	Resist
3 mTorr	Etch Rate	582	745	631
	Deviation	8 %	8 %	9 %
6 mTorr	Etch Rate	390	640	490
	Deviation	9 %	10 %	11 %
10 mTorr	Etch Rate	360	423	370
	Deviation	2 %	6 %	11 %
15 mTorr	Etch Rate	310	249	295
	Deviation	19 %	15 %	11 %
20 mTorr	Etch Rate	196	43	309
	Deviation	12 %	15 %	23 %

Table E.1: Etch rate in A/min and standard deviation for an applied RF Power P=500 W and a pressure of 3 mTorr to 20 mTorr

Appendix F

Listing RC-model

```
* RC-Spice model for TFEL
   .param q0='1.6e-19'          $ elementar charge
   * DRIVING PARAMETER:
   .param V_d=270               $ driving voltage peak-0 [V]
   .param f_d=5k                $ driving frequency [Hz]
   * TFEL-PARAMETER:
   .param C_ia=0.000177     $ insolator capacity per area in [F/m^2]
   .param C_pa=0.000083     $ phosphor layer capacity per area in [F/m^2]
   .param A='0.785e-6'      $ active area in [m^2]
   .param EF='1.16*q0'      $ Fermi Level of the interface state in eV
                            $ counted from valenz band edge
   $ density of interface states per area [electrons/m^2]
   .param n_s='4e4*1e12'
   .param d_p='0.8e-6'                $ thickness phosphor layer
   .param m_e_eff='0.25*9.11e-31'     $ effective electron mass
   * DERIVED PARAMETER
   .param t_sim='1/f_d/2'                 $ simulation time
   .param Qs0='n_s*q0*A'                  $ total interface charge
   .param c1='q0/sqrt(2*m_e_eff*EF)/4'
   .param c2='4/(3*q0*1.05e-34)*sqrt( 2*m_e_eff*EF^3)'
   .param jlimit='0.5e6'     $ limitation of current density for Art
```

```
* Define Nonlinear Components
.func  Tu( F )  'c1*F*exp(-c2 / F)' $ tunneling function
.func  Rt( V )  'Qs0*Tu( V / d_p )' $ nonlin. resistor modeling tunneling
$ nonlin. capacitor for interface states
.func  Cs( Vc ) 'C_pa*A /( 1 + C_pa*A*ABS(Vc)/Qs0 )'
Vd    1 0  SIN(0 V_d f_d ) AC V_d
Ri    1 2  10
Ci    2 3  C='C_ia*A'  IC=0V
Cp    3 0  C='C_pa*A'  IC=0V
ARt1  3 4  I=IF ABS(V(3)-V(0))<0.1  $ resistor modeling tunneling
+          THEN 0                   $ voltage around 0V
+          ELSE IF (V(3)-V(0))>0
+              THEN IF  Rt(V(3)-V(0))>jlimit*A
+                  THEN jlimit*A                  $ limitation
+                  ELSE Rt(V(3)-V(0))             $ positive current
+              ELSE IF  Rt(-(V(3)-V(0)))>jlimit*A
+                  THEN -jlimit*A                 $ limitation
+                  ELSE -Rt(-(V(3)-V(0)))         $ negative current
ACs1  4 0  I= Cs(V(4)) * DER.V(4)
R1    3 0   1e18
R2    4 0   1e18
.PLOT TRAN  V(1) V(3) I(Vd)  I(ARt1)
.print TRAN V(1) I(Vd) I(ARt1)
.OP
.trans 0.0001ms 0.4ms
```

Appendix G

Publication

Fast modelling of the optical characteristics of electroluminescent pixel structures

J.Rüdiger, C.Mias, R.Stevens and W.M.Cranton

Abstract: An analytic model of the optical behaviour of laterally light emitting thin film structures is developed. It is employed to calculate the outcoupled light of a pixel used in light emitting dot matrix displays such as laterally emitting thin film electroluminescent displays (LETFEL) with micromirrors. Consequently, one can identify the optimum pixel geometry. Here, the optical behaviour of the circular, square and hexagonal pixel geometry is modelled. The presented closed form solutions are based on a ray optics approximation whereby the absorption of the light within the light generating medium (phosphor material) and the transmission behaviour of the phosphor–air interface is taken into account, as well as the micromirror width. These solutions, however, neglect back reflected light. The effect of this neglect is investigated for square pixels by taking into account the first reflection. The model is applied to a typical LETFEL display with ZnS material doped with Mn. An optimal pixel diameter of 35 μm is estimated for that particular type of display.

1 Introduction

An analytical model of the optical behaviour of a pixel of a laterally emitting thin film electroluminescent display (LETFEL) with micromirror technology in presented. The pixel structure is illustrated in Fig. 1a. The LETFEL device is an improvement over the conventional thin-film electroluminescence (TFEL) device. A conventional TFEL is a stack of layers (TFEL-stack), which consists of an active thin-film phosphor sandwiched between thin-film insulating layers (Y_2O_3) and electrodes. The phosphor material is zinc sulphide (ZnS) doped with Mn whereby the Mn atoms function as light emitting centres. The application of an alternating electric field across the device results in luminous emission from the phosphor film. For a conventional TFEL device, this light is emitted in a direction perpendicular to the film plane so that the light passes through an insulating layer and a transparent electrode, which results in low resolution and weak emitting light sources [1–3]. In comparison, the LETFEL device utilises lateral emission with a micromirror for reflection resulting in approximately four times higher emission for small pixels [4].

The thin-film stack (Y_2O_3–ZnS–Y_2O_3) of a LETFEL forms a planar waveguide. Light generated within the phosphor layer is guided along the planar waveguide to the phosphor–passivation layer interface (Fig. 1*a*). There, it is coupled out laterally and deflected by the micromirror perpendicular to the planar pixel structure. The mirrors are arranged as surface emitting apertures forming pixels. Fig. 1*b* shows such a pixel. The geometry of the pixel affects the brightness and resolution of the display. Thus, it is our aim to optimise the pixel geometry to compensate for the high attenuation coefficient of the planar waveguide (about 12 000 neper/m [5]).

A further problem is caused by total internal reflection at the interface between the phosphor layer and the surrounding passivation layer (SiON). Light which is generated within the phosphor and reaches the phosphor–passivation interface with an angle greater than the angle of total internal reflection is reflected back into the pixel and attenuated again. The angle of total reflection is about 43° (referred to the interface normal) for the ZnS–SiON interface. Different pixel geometries such as a circle, a square and a hexagon could thus influence the angular distribution of the incident light and consequently affect the optical efficiency of the pixel.

This paper focuses on developing a fast analytic technique. This technique can be used, if we increase the number of ray reflections taken into consideration, to indentify a suitable pixel geometry and an optimum pixel diameter. To obtain the latter, it should be remembered that the larger the pixel diameter the more light is produced and the more attenuation occurs. Consequently, no significant increase of outcoupled light appears beyond a certain pixel diameter; a limiting effect occurs and hence the ratio of the emitted light flux to the total pixel area decreases. The limiting effect has been experimentally observed for a length of waveguide greater than 175 μm [5]. On the other hand, if the pixel diameter is too small, more chip area is used for the micromirrors. Thus, the ratio of active (phosphor) to passive (mirrors) area lessens and the ratio of the emitted light flux to total pixel area decreases. As a consequence, an optimum pixel diameter exists for a given mirror width and attenuation coefficient.

The outcoupled light of a pixel can be calculated with standard simulators based on ray tracing methods or by

© IEE, 2001

IEE Proceedings online no. 20010072

DOI: 10.1049/ip-opt:20000072

Paper first received 6th April and in revised form 6th October 2000

J. Rüdiger, C. Mias and W.M. Cranton are with the Department of Electrical and Electronic Engineering, The Nottingham Trent University, Burton Street, Nottingham NG1 4BU, UK

R. Stevens is with the Central Microstructure Facility, Rutherford Appleton Laboratory, Chilton, Didcot, Oxfordshire OX11 0QX, UK

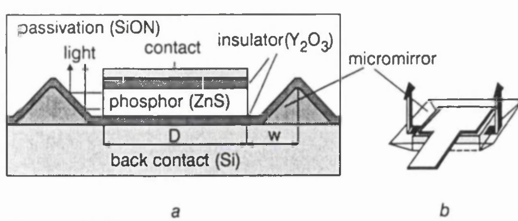

Fig. 1 *LETFEL device*

a cross-section
b schematic of a LETFEL pixel

solving the vector wave equation. Since the light generating layer can be considered as an ensemble of homogeneously distributed and isotropic light sources, a simulation must be performed for each point and each direction. Hence standard simulators require excessive computing resources even for two-dimensional models. The proposed method in this paper avoids this disadvantage.

2 Model for three-dimensional structures

The proposed optical model is based on ray optics so that optical attenuation is taken into account. Light that is reflected back into the pixel due to total internal reflection is neglected. This simplification of the problem is a good approximation for materials with a high attenuation coefficient, because the back reflected light is attenuated. Different transmission coefficients depending on polarisation and incident angle are not taken into account for the examples under investigation although they can be readily introduced.

The total light flux (luminous power) Φ of a light source is calculated as

$$\Phi = \int I d\Omega \tag{1}$$

where I is the luminous intensity, Ω is the solid angle and $d\Omega = (\cos\vartheta/r^2)dS$ [6], dS is the illuminated infinitesimal area element on the surface of a sphere around the light source, r is the distance between the light source and the area elements dS (see Fig. 2). The angle between the light ray and the surface normal vector $\mathbf{n}_S$ is ϑ. The light flux of an isotropically luminating light source ($I(\Omega) = \text{const.}$) is

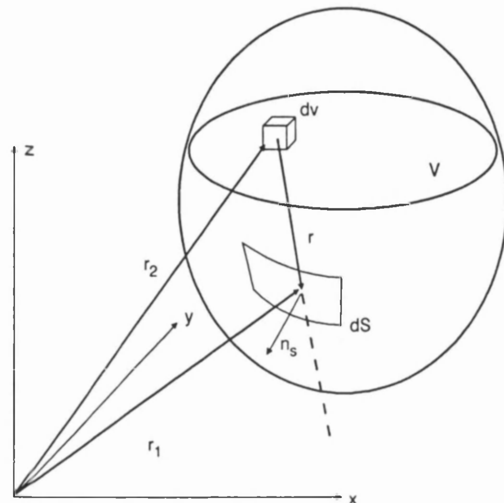

Fig. 2 *Geometry of a three-dimensional light emitting structure*

$\Phi = 4\pi I$. The illuminance on an area element dS at a distance r from the light source is defined as [6]

$$E = \frac{d\Phi}{dS} = I\frac{\cos\vartheta}{r^2} \tag{2}$$

For a homogeneously distributed isotropic light source, like a phosphor layer, it is necessary to define a light generation density g and an intensity density i for an infinitesimal volume dV

$$g := \lim_{\Delta V\to 0}\frac{\Delta\Phi}{\Delta V} = \frac{d\Phi}{dV} \tag{3}$$

$$i := \lim_{\Delta V\to 0}\frac{\Delta I}{\Delta V} = \frac{dI}{dV} \tag{4}$$

Φ and I denote the light flux and the luminous intensity, respectively, generated in the volume element dV. The units of g and i are lm/m^3 and $\text{cd/m}^3 = \text{lm/sr}\cdot\text{m}^3$, respectively. The intensity density for isotropically luminating infinitesimal light sources is then $i = 1/4\pi g$. To obtain the illuminance E on an area element dS with position vector $\mathbf{r}_1$ on the surface of the light generating medium, the intensity density i of all points in the light emitting volume V (pixel volume) must be summed up taking into account the attenuation in the medium (see Fig. 2)

$$E = \int_V a(r) i \frac{\cos\vartheta}{r^2} dV \tag{5}$$

where r is the distance between the light source and the area element on the surface $r = |\mathbf{r}_1 - \mathbf{r}_2|$, ϑ is incident angle $\vartheta = \angle(\mathbf{r}_1 - \mathbf{r}_2, \mathbf{n}_A)$, $dV = dx\,dy\,dz$, $\mathbf{r}_2 := (x, y, z) \in V$. The attenuation function is $a(r) = e^{-\alpha r}$ where α is the attenuation coefficient of the intensity. The total outcoupled light flux Φ is obtained by integrating the illuminance over the surface S of the light emitting structure whereby the transmission function $T(\vartheta)$ of the surface is taken into account

$$\Phi = \oint_{A_S}\int_V T(\vartheta) a(r) \frac{g}{4\pi r^2}\cos\vartheta dV dA \tag{6}$$

where r_1 is the vector along the surface $\mathbf{r}_1 = (x(u, w), y(u, w), z(u, w)) = \mathbf{r}_1(u, w) \in A_S$, $dA = |\mathbf{r}_{1u} \times \mathbf{r}_{1w}| du\,dw$, $\mathbf{r}_{1u} = \partial\mathbf{r}_1/\partial u$ and $\mathbf{r}_{1w} = \partial\mathbf{r}_1/\partial w$. The parameters u and w are the curvilinear coordinates. Light which is reflected back into the pixel due to total internal reflection is neglected.

3 Model for two-dimensional structures

Similar formulae to those given in Section 2 can be developed for a two-dimensional, thin layered laterally emitting structure (see Fig. 3). The real pixel is a three-dimensional structure but it can be approximated as a two-dimensional structure if the layer thickness is small compared to the pixel dimension. This is true for LETFEL devices where thin films are less than 1 μm thick and the pixel size exceeds 10 μm^2. The layers form a planar waveguide. Emitted light propagates therefore only in two dimensions along the planar waveguide. The attenuation coefficient α is, in this case, the attenuation coefficient of the waveguide, which can be experimentally obtained. For a calculation of a two-dimensional structure,

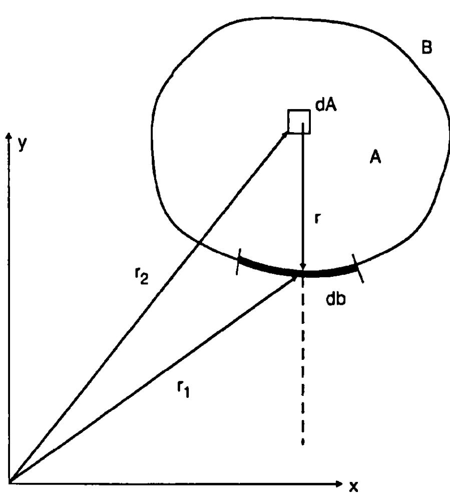

Fig. 3 *Geometry of a two-dimensional light emitting structure*

the following definitions need to be introduced (where the prime indicates a two-dimensional parameter):

$$I' := \frac{d\Phi}{d\omega} \tag{7}$$

$$E' = \frac{d\Phi}{db} = I' \frac{\cos \vartheta}{r} \tag{8}$$

where ω is the angle with $d\omega = (\cos \vartheta / r) db$, b is the border line length, r denotes the distance between the light emitting area element dA and the boundary element db. The incident angle ϑ is defined as the angle between the light ray and the boundary normal vector. The two-dimensional luminous intensity I' defines the portion of radiated light flux $d\Phi$ per infinitesimal unit of angle. The two-dimensional illuminace E' defines the portion of light flux $d\Phi$ per length db falling on an infinitesimal part db of the pixel boundary. Furthermore, the two-dimensional luminous intensity density i' and the two-dimensional light generation density are defined as

$$g' := \frac{d\Phi}{dA} \tag{9}$$

$$i' := \frac{dI'}{dA} = \frac{1}{2\pi} \frac{d\Phi}{dA} \tag{10}$$

where A is the active (light emitting) pixel area. The units of the two-dimensional luminous intensity density i' and the two-dimensional light generation density g' are lm/(rad·m^2) and lm/m^2, respectively. The two-dimensional light generation density g' represents the generated light flux Φ per infinitesimal area element dA. The two-dimensional luminous intensity density defines the luminous intensity for an area element dA.

A single area element emits light, which is travelling towards the pixel boundary and results in an illumination of the pixel boundary. The illuminance (of a point on the boundary) per area element dA, e', is calculated from eqns 8 and 10

$$e' = \frac{dE'}{dA} = a(r) i' \frac{\cos \vartheta}{r} (\mathrm{lm/m^3}) \tag{11}$$

under consideration of the attenuation $a(r)$. The illuminance E' of a point at the pixel boundary is then given by the area integral over the entire pixel area A

$$E' = \int_A a(r) i' \frac{\cos \vartheta}{r} dA = \int_A a(r) \frac{g'}{2\pi r} \cos \vartheta dA \tag{12}$$

To obtain the total emitted light flux of the pixel, the total illuminance E' along the boundary line **B** must be integrated, by also taking into account the transmission function $T(\vartheta)$ for the phosphor–passivation interface

$$\Phi = \oint_B \int_A T(\vartheta) a(r) \frac{g'}{2\pi r} \cos \vartheta dA db \tag{13}$$

where ϑ is the incident angle, $\mathbf{B}(t)$ is the boundary line of the pixel and $db = |\frac{d}{dt}\mathbf{B}(t)| dt$; t is the transformation parameter. eqn. 13 can be solved more easily when the area integral is written in polar coordinates with the origin on the boundary ($\mathbf{r}_1 = 0$)

$$\Phi = \oint_B \int_{-\vartheta_t}^{\vartheta_t} \int_0^{R_B} a(r_2) \frac{g'}{2\pi} \cos \vartheta dr_2 d\vartheta db \tag{14}$$

where $\mathbf{r}_2 = (r_2 \cos \vartheta, r_2 \sin \vartheta)$, $R_B = R_B(\vartheta)$ is the distance from the origin to the boundary B and ϑ_t is the angle for total internal reflection. The transmission function is simplified so that $T = 1$ for $\vartheta < \vartheta_t$ and $T = 0$ for $\vartheta \geq \vartheta_t$ (total internal reflection occurs). This means the integration of ϑ is carried out with $T = 1$ in the interval $-\vartheta_t$ to ϑ_t.

4 Model for circle, square and hexagon structures

The general solution for a two-dimensional structure is now applied to circular, square and hexagonal pixels as these are the important structures for dot matrix displays. The light flux Φ_c of a circular pixel is solved using eqn. 14. The boundary radius R_B, which is the distance from the origin to the pixel boundary, is given by $R_B = D \cos \vartheta$ (upper integration limit), where D is the pixel diameter of the active area (Figs. 1 and 4). The active area of a circular structure is $A = \pi D^2/4$. The closed line integral for the pixel boundary is $D\pi$, because the illuminance is the same for each point at the boundary line owing to the symmetry of the circle. The integration w.r.t. the angle ϑ is carried out between 0 and the angle for total reflection ϑ_t. Thus, the integral must be multiplied by two for the full range $-\vartheta_t \leq \vartheta \leq \vartheta_t$. The attenuation function is $a(r) = \exp(-\alpha r)$ with the attenuation coefficient α in neper/m. Hence,

$$\begin{aligned} \Phi_c &= 2\pi D \int_0^{\vartheta_t} \int_0^{D \cos \vartheta} \frac{g'}{2\pi} \exp(-\alpha r) \cos \vartheta dr d\vartheta \\ &= g' \frac{1}{\alpha} D \int_0^{\vartheta_t} \{1 - \exp(-\alpha D \cos \vartheta)\} \cos \vartheta d\vartheta \end{aligned} \tag{15}$$

where the pixel diameter D denotes the diameter of the circle. The integral of eqn. 15 can only be solved numerically.

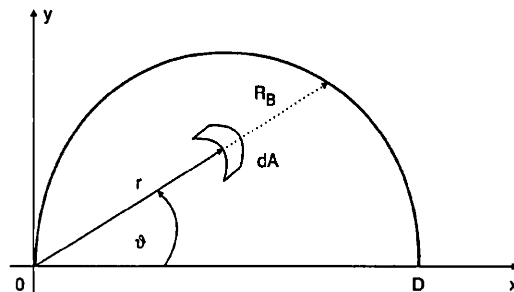

Fig. 4 *Geometrical region of the circular structure used in the calculations*

The light flux Φ_s of the square pixel is obtained by solving eqn. 14 for one side only because of the symmetry. The integration area is to be partitioned into two separate integration areas. The inner area integral can be solved analytically, while the integral w.r.t. the angle can only be solved numerically. The integration w.r.t. ϑ is carried out between 0 and the angle of total internal reflection ϑ_t. The result, eqn. 16, is valid for $0 \le \vartheta_t \le \pi/4$ (note $\vartheta_t \approx 43°$ for our LETFEL pixels)

$$\Phi_s = \frac{4}{\pi\alpha} g' \left\{ D \sin\vartheta_t - \frac{\sin^2\vartheta_t}{2\alpha} + \int_0^{\vartheta_t} \left(D\sin\vartheta - D\cos\vartheta + \frac{\sin 2\vartheta}{2\alpha} \right) \times \exp\left(-\alpha\frac{D}{\cos\vartheta}\right) d\vartheta \right\} \quad (16)$$

where the pixel diameter D denotes the length along a side of the square. The active area of the square is $A = D^2$.

The light flux Φ_h of a hexagonal structure is calculated by solving eqn. 14 for one side of the hexagon only. The integration area is partioned into four different integration areas. Only the inner integral of the radius can be solved analytically. The integrals along the border line and over the angle ϑ must be solved numerically. eqn. 17 is valid for $1/6\pi \le \vartheta_t \le 1/3\pi$:

$$\Phi_h = \frac{6}{\pi\alpha} g' \left\{ \rho\sin\vartheta_t - \int_0^{\rho}\int_0^{\alpha_1} \exp\left(-\alpha\frac{\sqrt{3}\rho}{\cos\vartheta}\right)\cos\vartheta d\vartheta dy - \int_{y_g}^{\rho}\int_{\alpha_1}^{\vartheta_t} \exp\left(-\alpha\frac{y+\rho}{\sin(\vartheta+\pi/6)}\frac{\sqrt{3}}{2}\right)\cos\vartheta d\vartheta dy - \int_0^{y_g}\left[\int_{\alpha_1}^{\alpha_2}\exp\left(-\alpha\frac{y+\rho}{\sin(\vartheta+\pi/6)}\frac{\sqrt{3}}{2}\right)\cos\vartheta d\vartheta + \int_{\alpha_2}^{\vartheta_t}\exp\left(-\alpha\frac{y}{\sin(\vartheta-\pi/6)}\frac{\sqrt{3}}{2}\right)\cos\vartheta d\vartheta\right] dy \right\} \quad (17)$$

where y is the ordinate (Fig. 3) >and the integration limits are

$$y_g = \frac{1}{2}\rho\left(\sqrt{3}\tan\vartheta_t - 1\right)$$

$$\alpha_1 = \arctan\frac{y}{\sqrt{3}\rho}$$

$$\alpha_2 = \arctan\left(\frac{2}{3}\sqrt{3}\frac{y}{\rho} + \frac{\sqrt{3}}{3}\right) \quad (18)$$

where ρ denotes the distance between the centre point and a corner point of the hexagon. This ρ is the radius of the outer circle of the hexagon. The equivalent pixel diameter D is the distance from side to side (inner circle of the hexagon) with $D = \rho\sqrt{3}$. The active area of a hexagonal pixel is $A = 3\rho^2\sqrt{3}/2$. It is again noted that for simplicity the above formulae for the outcoupled light ignore any internally reflected rays and are therefore valid for pixels with phosphor materials which posseses a sufficiently high attenuation.

5 Results and discussion

The outcoupled light of hexagonal, square and circular pixels is calculated by the numerical solution described in Section 4 using the program MATHCAD. In all the calculations reported below, the mirror width w is 2 μm, the angle of total internal reflection ϑ_t is 43° and the attenuation coefficient α is 12 000 neper/m. The light flux generation density g' is set to 1 lm/m^2.

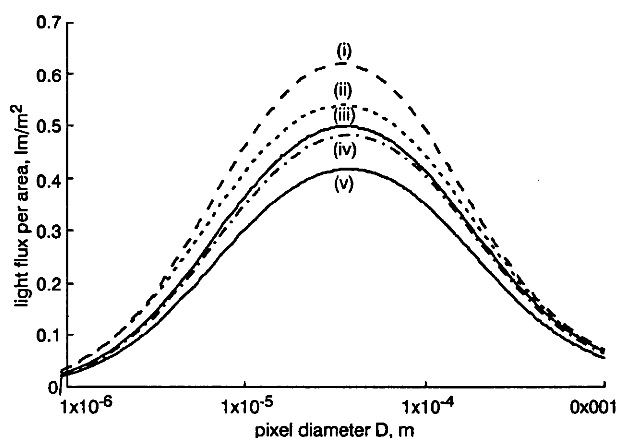

Fig. 5 *Light flux to pixel area ratio as a function of pixel diameter D*
mirror width, $w = 2$ μm
attenuation coefficient $\alpha = 12000$ neper/m
(i) square pixel (first reflection considered)
(ii) hexagonal pixel (no reflection considered)
(iii) square pixel (no reflection considered)
(iv) circular pixel placed in a hexagonal cell (no reflection considered)
(v) circular pixel placed in a square cell (no reflection considered)

Fig. 5 illustrates how the ratio of light flux to the total pixel area Φ/A_t varies with the pixel diameter D for the hexagonal structure (Φ_h/A_{th}), the square structure (Φ_s/A_{ts}), the circular structure placed in a hexagon (Φ_{tc}/A_{th}) and the circular structure (active region) placed in a square (Φ_c/A_{ts}). The total pixel area A_t is the sum of active area and passive area (mirrors). For the square structure, the total pixel area is given by $A_{ts} = (D + 2w)^2$ with D denoting the length along a side of the active square. The total pixel area for the hexagonal structure is given by

$$A_{th} = \frac{3}{2}\sqrt{3}\left(\frac{D}{\sqrt{3}} + w\right)^2$$

where the diameter D is the distance from one side to the opposite side of the hexagon (diameter of the inner circle of the hexagon). For all structures the maximum of light/area ratio occurs at the diameter $D \approx 35$ μm. This corresponds to a display resolution of 725 pixel per inch. The maximum light flux attainable per area is listed in Table 1.

The results in Fig. 5 (curves (ii)–(v)) were obtained by neglecting the back reflected light. To estimate the error caused by the simplification, a simulation of a square pixel is performed by condsidering the first reflection (see Fig. 5 curve (i)). Eqn. 16 for the square pixel is extended as

$$\Phi_{s1} = \Phi_s + \frac{4}{\pi\alpha} g' \int_{\vartheta_t}^{\frac{\pi}{4}} \left\{ \left[\int_{\min(D, D\tan\vartheta)}^{D} T(\vartheta)\left(1 - \exp\frac{-\alpha y}{\sin\vartheta}\right) \times \exp(-\alpha r) dy + \int_0^{\min(D, D\tan\vartheta)} T\left(\frac{\pi}{2} - \vartheta\right) \times \left(1 - \exp\frac{-\alpha D}{\cos\vartheta}\right)\exp(-\alpha r) dy \right\} \cos\vartheta d\vartheta \quad (19)$$

Table 1: Attainable light flux per unit area

Hexagon 54 %	circle in hexagon cell 48%
Square 50 %	circle in square cell 42%

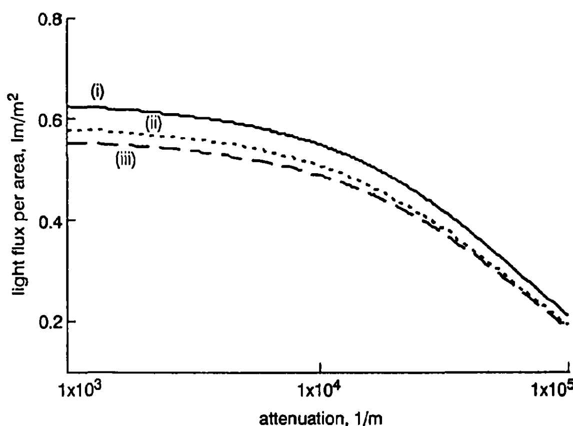

Fig. 6 *Light flux to pixel area ratio as a function of the attenuation coefficient α*

mirror width $w = 2\ \mu m$
pixel diameter $D = 30\ \mu m$
(i) hexagonal pixel
(ii) square pixel
(iii) circular pixel placed in a hexagonal cell

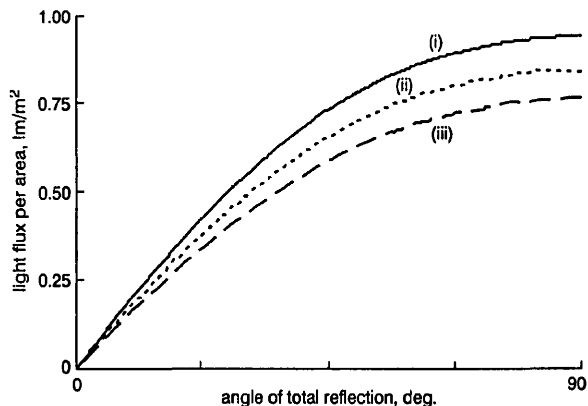

Fig. 7 *Light flux to pixel area ratio as a function of the angle of total internal reflection ($0 \leq \vartheta \leq \pi/2$) for a square pixel*

mirror width is $w = 2\ \mu m$
pixel diameter is $D = 30\ \mu m$
(i) $\alpha = 4000$ neper/m
(ii) $\alpha = 12000$ neper/m
(iii) $\alpha = 20000$ neper/m

where $r = \min(D/\cos\vartheta,\ (D-y)/\sin\vartheta)$, the trasmission function $T = 1$ for $\vartheta < \vartheta_t$ and $T = 0$ for $\vartheta \geq \vartheta_t$. By comparing curves (i) and (ii) in Fig. 5 it can be deduced that the optimal pixel diameter is unchanged and the error due to the neglect of the back reflected light is approximately 20% at the optimal pixel diameter.

Fig. 6 shows, the ratio of light flux to pixel area as a function of the attenuation coefficient for three different pixels with a diameter $D = 30\ \mu m$. The light flux decreases significantly for an attenuation coefficient greater than 10^4neper/m. Hence, the luminance of the display can be improved if the attenuation of the waveguide is reduced.

Fig. 7 shows a plot of the light flux to pixel area ratio as a function of the angle of total internal reflection for a square pixel with different attenuation coefficients. The light flux depends strongly on the angle of total internal reflection for $\vartheta_t \leq 77.5°$. The intensity of the outcoupled light can thus be improved further with an increasing ϑ_t. This can be achieved, for example, by employing other materials as passivation layers. Note, that for the square pixel, eqn. 16 is not valid for $\vartheta_t > \pi/4$. Thus, the following equation is used instead:

$$\Phi_r = \frac{4}{\pi\alpha} g' \int_0^{\vartheta_t} \left\{ \left(1 - \exp\frac{-\alpha D}{\cos\vartheta}\right)(D - \min(D, D\tan\vartheta)) + \min(D, D\tan\vartheta) - \frac{\sin\vartheta}{\alpha}\left(1 - \exp\frac{-\alpha\min(D, D\tan\vartheta)}{\sin\vartheta}\right) \right\} \cos\vartheta d\vartheta \quad (20)$$

6 Conclusions

A ray optics model for two-dimensional pixel structures has been developed. It is useful for the fast estimation of the outcoupled light and for the optimisation of the pixel geometry for a given attenuation coefficient. The model is applied to circular, square and hexagonal pixel structures because of their importance in dot matrix displays. For the display type investigated, the optimum pixel diameter is estimated to be about $35\ \mu m$. Future work will compare experimental results with the numerical predictions of the present model. The presented simulation method will be used in conjunction with an optical electromagnetic field simulator to investigate the influence of periodical shaped facets on the outcoupled light.

7 Acknowledgment

J. Rüdiger would like to thank the Nottingham Trent University for the award of a scholarship.

8 References

1 ONO, Y.A.: 'Electroluminescent displays' (World Scientific, 1995)
2 STEVENS, R., THOMAS, C.B., and CRANTON, W.M.: *Appl. Phys. Lett.*, 1993, 63, pp. 3119–3121
3 THOMAS, C.B., CRANTON, W.M., and McCLEAN, I.P.: 'Laterally emitting TFEL displays devices', *Proc. S.I.D.*, 1995, **25**, pp. 887–890
4 STEVENS, R., THOMAS, C.B., and CRANTON, W.M.: 'Enhancing the brightness of thin-film electroluminescent displays by improving the emission process', *IEEE Electron Device Lett.*, 1994, **15**, (3), pp. 97–99
5 STEVENS, R.: PhD thesis, University of Bradford, 1994
6 MENDE, D., and SIMON, G.: 'Physik - Gleichungen und Tabellen' (Fachbuchverlag Leipzig, Leipzig, 1988)